Plasmonic Structural Color and Sensing

by

Pamela Mastranzo Ortega

Thesis submitted to the program in Optics in partial fulfillment of the requirements for the degree of

Ph. D. in Optics

at the

Instituto Nacional de Astrofísica, Óptica y Electrónica

Noviembre 2023

Tonantzintla, Puebla

Advisor:

Dr. J. Javier Sánchez Mondragón, INAOE

Dr. Debashis Chanda, UCF

©INAOE 2023

Abstract

In recent years, nanostructures have gained prominence in the field of structural color due to the presence of plasmonic resonances within the visible frequency spectrum. In nature, we find examples of nanostructures that produce color through optical mechanisms such as refraction, reflection, scattering, and interference. Colors generated by these mechanisms tend to be purer and can encompass a wide range.

One critical advantage of nanostructures is their ability to manipulate light, which holds great potential for various optical applications. However, manufacturing these nanostructures is intricate, requiring methods like nanoimprinting or lithography to create periodic patterns. This complexity can result in high production costs, posing challenges for widespread industrial implementation.

The primary objective of this thesis centers on the investigation, fabrication, and experimental analysis of a plasmonic structure designed for easy manipulation, particularly in generating structural color. This structure comprises a layer of aluminum, a thin layer of aluminum oxide ($Al2O3$), and a layer of aluminum nanoislands. Its fabrication requires electron beam evaporation to deposit the aluminum layer and grow the nanoislands, and for depositing the $Al2O3$ layer, the technique of atomic layer deposition (ALD) is used. It's noteworthy that this structure can be readily applied to flexible surfaces. Using the same nanoisland growth method, we also explored the manufacturing and analysis of a potential application - specifically, a humidity and temperature sensor. Here, a polymer served as a modification medium within the nanostructure, resulting in a tunable color response to changes in humidity and temperature.

Finally, we briefly introduce a novel nanostructure composed of Vo2 exhibiting structural color. This material possesses thermoelectric properties, leading to a color shift in response to variations in temperature and voltage, thus displaying structural coloration.

Resumen

En los recientes años las nanoestructuras han tenido grandes logros en el campo del color estructural, debido a la presencia de resonancias plasmonicas dentro del espectro de frecuencias visibles. En la naturaleza encontramos ejemplos de nanoestructuras que producen color atreves de mecanismos ópticos tales como refracción, reflexión, esparcimiento e interferencia. Los colores generados por estos mecanismos tienden a ser puros y pueden abarcar una gama amplia.

Una ventaja fundamental de las nanoestructuras es su habilidad para manipular la luz, lo que tiene un gran potencial para diversas aplicaciones ópticas. Sin embargo, la fabricación de estas nanoestructuras es compleja y requiere métodos como la nanoimpresión o la litografía para crear patrones periódicos. Esta complejidad puede resultar en altos costos de producción, lo que plantea desafíos para la generalizada implementación industrial.

El objetivo principal de esta tesis se centra en la investigación, fabricación y análisis experimental de una estructura plasmónica diseñada para una fácil manipulación, particularmente en la generación de color estructural. Esta estructura contiene una capa de aluminio, una fina capa de óxido de aluminio ($Al2O3$) y una capa de nanoislas de aluminio. La fabricación requiere evaporación por haz electrones para el depósito de una capa de aluminio y crecimiento de nanoislas; para el depósito de la capa de $Al2O3$ es usada la técnica de deposición de capas atómicas, demostrando que la estructura se puede aplicar fácilmente a superficies flexibles. Utilizando el mismo método de crecimiento de nanoislas exploramos la fabricación y el análisis de una potencial aplicación, específicamente, un sensor de humedad y temperatura. En este caso, un polímero sirvió como medio de modificación dentro de la nanoestructura, lo que dio como resultado una respuesta de color ajustable a los cambios de humedad y temperatura.

Finalmente, presentamos brevemente una nueva nanoestructura compuesta de $VO2$ que exhibe color estructural. Este material posee propiedades

termoeléctricas, lo que provoca un cambio de color en respuesta a las variaciones de temperatura y voltaje, mostrando así una coloración estructural.

Preface

Both technoscientists and artists have studied colors of physical origin. On the other hand, colors with a chemical origin have not only spawned but also sustained entire industries, some for several millennia. In modern times, physical colors are gaining increasing technical importance. Given color's relevance in everyday life and industry, we are becoming more intrigued by structural colors. This is primarily because their production doesn't involve the release of volatile organic compounds, which do not pollute the environment and pose risks to life. For this reason, this work we are particularly interested in utilizing structural colors as detection tools or as alternative pigments. The structure of the thesis is described below.

The first Chapter introduces previous concepts of what color is, how it is possible to obtain and codify it, and why structural color has emerged lately and has gained more strength in recent years. This Chapter also specifies the general and particular objectives achieved in the thesis.

The second Chapter explains the theory necessary to understand the phenomenon that occurs when an electromagnetic field incises metallic nanostructures, particularly a nanoparticle. The phenomenon of localized plasmons is mathematically described since we work with metallic nanoislands in this thesis. Finally, the methodology of forming metallic islands is described, explaining in more detail the mechanism used in the experiments.

In Chapter 3, we introduce the experimental and simulation methods used that we used for modeling the plasmonic structure. The simulation software is Lumerical and contains FDTD to solve Maxwell's equations, allowing us to focus on the simulation design. Concerning the experimental part, we use standard techniques to deposit, such as Ebeam, ALD, and Spin coating. The description of its parameters is in detail in Chapter 4. because each experiment has its recipe.

Chapter 4 is dedicated to the structural color project and color tunability. This chapter is divided into two parts: the first is directed to the structural color project, and the second is directed to color tuneability. The first section of the chapter starts with a description of the plasmonic cavity; the next section discusses the experimental methodology that was carried out and the simulation model with different conditions. Finally, it shows the color generated and the results that we have of the analysis of the structural color. In the same way, the Tunability color follows this same format, starting with an introduction to the project and ending with the results and conclusions that were obtained. This chapter demonstrates two projects that can be replicated, and that can also be used for detection.

Chapter 5 is very brief since it shows a project in the experimental phase, which also generates structural color. Finally, we have Chapter 6, which are the general conclusions that were obtained from all the thesis work carried out.

Acknowledgments

I dedicate this work to all those people I love who have always been there and believed in me. I hope it provides guidance and new ideas for new research projects for every reader who encounters it.

Thank you.

TABLE OF CONTENTS

CHAPTER 1

INTRODUCTION

This Chapter serves as an introduction to several basic concepts in color production. In Section 1.1, important aspects of the human visual system for color interpretation are summarized, using the CIE system based on standard observations in colorimetry to establish the magnitudes of the primary values (tristimuli) that equal the spectral values. We also define the color models commonly used in monitors, mobile phones, tablets, etc., known as RGB light colors, and the CMYK pigment colors used in printed material, specifically paper. Section 1.2 discusses chemical colors, which are generated through light absorption by pigments. Section 1.3 explores structural colors that arise from light scattering by microstructures. Finally, in Section 1.5, the general and specific objectives of the thesis are detailed.

1.1.   Color

The Color begins with the reception of light by the retina, a photosensitive structure located at the back of the eye. Within the retina, cells convert this light into signals, which are then conveyed to the brain. These signals are processed in the brain to yield the sensation of Color. For Color encoding, the human is

expressed through three signal values produced by the retina. This encoding forms the basis for color measurement and represents Color as a set of red, green, and blue values. This chapter focuses on this encoding, which can be expressed through color models[1].

Color perception is a complex phenomenon influenced by various factors, including the spectral composition of light, physiological aspects of vision, and the psychology of the observer. It's not an inherent property of an object, as changing the light source can alter the perceived color. Instead, it hinges on the interplay between incident radiation, an object's capacity to interact with it, and the observer's visual system[2].

The chromatic stimulus comprises three distinct attributes, imparting color with its three-dimensional nature:

Hue/Tone: This is the foundational characteristic traditionally used to classify colors as reddish, yellowish, etc. It enables us to discern a color from a gray shade of the same brightness, known as an achromatic stimulus. It's linked to the variations in radiant energy absorption at different wavelengths, constituting the qualitative aspect of color.

Brightness/Luminosity: This trait allows colors to be broadly categorized as warm or dark. More precisely, it can be defined as the quality that permits colors to be considered equivalent to specific members of the grayscale, ranging from black to white. It offers a relative assessment of reflected versus absorbed light.

Saturation/Purity: This determines how much a color deviates from the gray of the same brightness and characterizes the reflection or transmission at a particular wavelength. Chromaticity is the quantitative measure of color, while saturation denotes its intensity. Brightness is not regarded as a component of the chromatic attribute.

---

[1] M. C. Stone, A Field Guide to Digital Color, Massachusetts: A. K. Peters, 2003.

[2] C. y. c. d. alimentos, "El Color: Fundamentos y Aplicaciones," [Online]. Available: https://es.slideshare.net/lauralclavijo/colorimetria-triestimulo-texto.

Color and its measurement have been the focus of inquiry for many scientists over the centuries. The assessment of color can be accomplished through two main methods: visual evaluation or instrumental assessment using specialized devices.

The color stands out as the only sensory attribute for which analytical measurement techniques have been developed with a level of precision that can replace subjective judgments. Instrumental methods offer repeatability and objectivity. However, their application necessitates expensive equipment.

The fundamental visual analysis of color is encompassed in organoleptic examinations, which involve visually appraising an object's qualities. This approach finds significant use in fields like food assessment. Another visual method for measuring color involves using color scales, atlases, dictionaries, or collections. A wide array of scales exists to describe color. One of the most widely utilized in color is the CIE L*a*b* scale. The human visual system exhibits an impressive ability to differentiate between colors but tends to have a weaker visual memory.

In instrumental evaluation, the color of objects is represented by color coordinates derived from the tristimulus values X, Y, and Z.

$$X = k \sum_{380}^{780} \bar{x}(\lambda) \cdot R(\lambda) \cdot \Delta\lambda$$
$$Y = k \sum_{380}^{780} \bar{y}(\lambda) \cdot R(\lambda) \cdot \Delta\lambda \qquad (1.\,1)$$
$$Z = k \sum_{380}^{780} \bar{z}(\lambda) \cdot R(\lambda) \cdot \Delta\lambda$$

Here, $\bar{x}(\lambda)$, $\bar{y}(\lambda)$, and $\bar{z}(\lambda)$ denote the mixing functions or values of spectral stimuli. $R(\lambda)$ represents the radiance of the object, whether it be emitted from a light source or reflected/transmitted by the object from another source. $\Delta\lambda$ signifies the interval over which the summation is conducted, and K is a predefined constant that adjusts the tristimulus values to ensure T falls within the range of 0 to 100.

Instruments designed to measure the color of an object fall into two categories: those that directly gauge the tristimulus values, known as colorimeters, and those that measure the radiometric or photometric magnitude characterizing the source or object from which the tristimulus values are derived (such as spectrophotometers and spectroradiometers).

Due to the anatomical distribution of the cones in the eye, the tristimulus values will depend on the observer's field of view. The CIE defined the CIE XYZ colorimetric standard observer to eliminate this variable. Originally considered the average of chromatic viewing perceptions across a 2° angle due to the belief that the color of sensitive cones resided within a 2° arc of the fovea. Therefore, at the 8th general meeting of the CIE 1931, tables were given with the color coefficients that constitute the definition of the CIE 1931 standard observer, also known as CIE 1931 2°. Standard observer[3].

For the study and analysis of color, the model or color space is considered in this work, which tells us how a color is defined. These models are essential tools since they allow us to analyze and take advantage of all the information in the image. The color spaces that are used for image processing are RGB and CMYK. A brief description of these is given in the next section.

RGB

There are three types of cones in humans, each responsive to distinct wavelengths of light. These are referred to as long, medium, and short wavelength cones (LMS) or, more casually, red, green, and blue cones (RGB). Each cone absorbs light and transmits a signal along the optic nerve, indicating the total amount of light energy detected by the cone. In the brain, this signal is interpreted to construct the perception of Color. This process carries two significant implications for comprehending color vision. First, the spectral distribution is condensed into precisely three values, one for each cone. Second, these values, rather than the original spectrum, constitute the earliest representation of color perception. These principles are termed trichromacy and

---

[3] A. V. Muñoz, Principios de color y holopintura, Club Universitario, 2013.

metamerism, respectively. Color measurement, or colorimetry, leverages these principles to encode Color using three numerical values. Likewise, digital color imaging employs these principles to encode Color as RGB pixels, which are also described by three numbers. This alignment is not accidental: color vision at the retinal encoding level fundamentally operates as an RGB encoding system. The fundamentals of vision, as expounded in this chapter, are remarkably systematic, involving concise mathematical operations on spectra and their encodings.

An RGB color space is composed of three primary colors: red, green, and blue. These colors are combined following the principles of additive mixture. In the realm of physical light, the process of adding colors entails the combination of their respective spectra. The resulting color is what an individual with normal vision would perceive. However, in the digital color domain, we typically do not explicitly consider the associated spectra of the RGB color primaries. Instead, a color is represented as a triplet of numbers, with one value associated with each primary. These values are combined through addition, much like vector addition. For instance, (0, 1, 0.5) + (1, 0, 0.2) results in (1, 1, 0.7). From a mathematical standpoint, the R, G, and B components serve as the axes of a three-dimensional color space.

The RGB color space is represented as a cubic unit, encompassing black at (0, 0, 0) and white at (1, 1, 1). The remaining vertices of the cube denote the primary colors (red, green, and blue) and their pairwise combinations, referred to as the secondary colors (cyan, magenta, and yellow). *Figure 1* visually illustrates these colors along with their respective values. From a mathematical standpoint, colors can extend beyond the unit cube by adopting values greater than one or less than 0. However, values are confined within (0, 1) in most RGB color space applications. The unit cube thus encapsulates the full spectrum of colors defined within this color space. Gray shades, achieved when red, green, and blue values are equal, align along the cube's main diagonal, transitioning from black to white. Within an RGB triplet, the smallest value determines the level of gray infusion, while the remaining two primaries establish the hue and

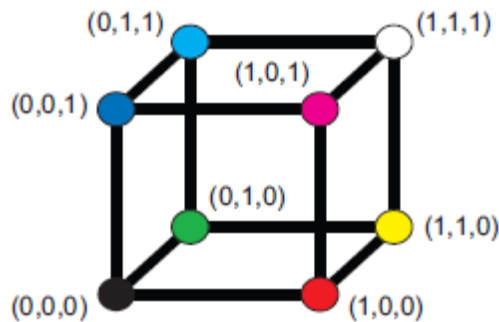saturation. Fully saturated colors, devoid of any gray component, reside exclusively on the cube's surface.

Figure 1 The RGB color cube, with each vertex labeled with its corresponding RGB triple[4].

These characteristics can be used to create an interpretation of the RGB color cube arranged as a perceptual color space. In this representation, the cube's main diagonal serves as the achromatic axis, spanning from black to white. The distance from this axis determines the "saturation" level, while the hue is organized into a closed shape, commonly a hexagon, triangle, or circle.

A 3 × 3 matrix, determined by the tristimulus values of the primaries, can be employed to convert any RGB color into its corresponding tristimulus values. These CIE tristimulus values establish a three-dimensional space characterized by its axes: X, Y, and Z. The outcome of applying this 3 × 3 matrix to the vertices of a physically defined RGB color cube is depicted in *Figure 2*. Here, the primary colors manifest as vectors of varying lengths directly proportional to their luminance. Their orientation is determined by their color, defined by an XYZ triple. White is a color defined by these primaries, calculated by summing them, while black corresponds to (0, 0, 0).

The color cube maintains a roughly cubical shape with three pairs of parallel sides, but its square faces are now parallelograms. There is still an achromatic axis along the main diagonal, and the fully saturated colors still lie on the surface, which encloses the color gamut. For those acquainted with 3D

---

[4] M. C. Stone, A Field Guide to Digital Color, Massachusetts: A. K. Peters, 2003.

transformation matrices, this shape visually affirms the affine transformation (a combination of rotation, scaling, and skewing) described by the 3 × 3 matrix.

When an RGB color space is represented on the chromaticity diagram by converting the CIE XYZ coordinates into chromaticity values, it forms a triangle, as depicted in *Figure 2*. The corners represent the primary colors, while the secondary colors are positioned along the line between the primaries at a distance proportional to the relative brightness of the two primaries. A solid dot denotes white and generally lies near the center of the triangle. Black is directly beneath white—effectively; this is the skewed cube in CIE XYZ coordinates projected along its black/white axis. The lines extending from white to the colors represent the projections of the edges of the color cube—half connect to black and half to white. Every color within the color gamut falls inside this triangle.
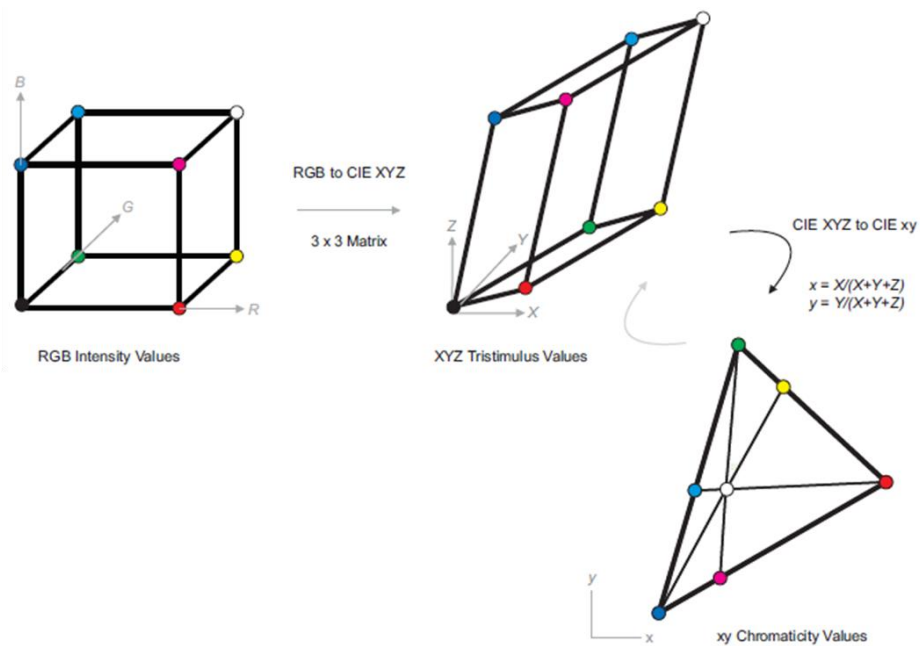

Figure 2. The RGB color cube can be converted to CIE XYZ using a 3X3 matrix. This transformation scales, rotates, and skews the cube. The CIE XYZ values can be mapped to the chromaticity diagram via the usual formulas. The result is a triangle, whose vertices are red, green, and blue. White and black lie on the same point5.

---

[5] R. E. W. Rafael C. Gonzalez, Digital Image Processing, Fourth ed., 330 Hudson Street, New York, NY 10013: pearson, 2018.

RGB color spaces defined by different primaries project as different triangles. While comparing these projections can offer insights, it only offers comprehensive information about whether a color exists within both color spaces due to the absence of brightness information. In other words, a color within the triangle projection may not necessarily reside within the entire color space volume because it could be either too bright or too dark. For an accurate comparison, a three-dimensional space is required.

CMYK

The CMYK model differs from the previous one. Still, like its predecessor, its name is an acronym derived from the colors it uses as references: cyan, magenta, and yellow, with the inclusion of black (referred to as "Key" in English to distinguish it from the "B" in the blue of the RGB model).

As already mentioned above a color model, also known as a color space or color system, provides a standardized way to specify colors. A color model consists of a coordinate system and a subspace within that system, where a single point within that subspace represents each color. Most of the color models today are tailored for hardware applications (such as color monitors and printers) or specific applications where color manipulation is a primary objective, as seen in fields like animation graphics[6].

Regarding digital image processing, the commonly employed hardware-oriented models include the RGB (red, green, blue) model for color monitors. This model assumes that all RGB color values have been normalized to fall within the range of [0, 1].

$$\begin{bmatrix} C \\ M \\ Y \end{bmatrix} = \begin{bmatrix} 1 \\ 1 \\ 1 \end{bmatrix} - \begin{bmatrix} R \\ G \\ B \end{bmatrix} \qquad (1.\,2)$$

Equation (1. 2). illustrates that light reflected from a surface coated with pure cyan lacks red content (i.e., C - R = -1 in the equation). Similarly, pure

---

[6] R. E. W. Rafael C. Gonzalez, Digital Image Processing, Fourth ed., 330 Hudson Street, New York, NY 10013: pearson, 2018.

magenta lacks green reflection, while pure yellow lacks blue. This equation also demonstrates that RGB values can be easily derived from a set of CMY values by subtracting each CMY value from 1.

As depicted in Figure 3, an equal mixture of the pigment primaries—cyan, magenta, and yellow—should theoretically produce black. However, in practice, because C, M, and Y inks are seldom pure colors, their combination produces a muddy-looking brown instead of true black. To address this, a fourth color, black (denoted by K), is introduced in the CMYK color model. The amount of black added is precisely calibrated to achieve true black. Therefore, when publishers refer to "four-color printing," they indicate the inclusion of the three CMY colors and a portion of black.
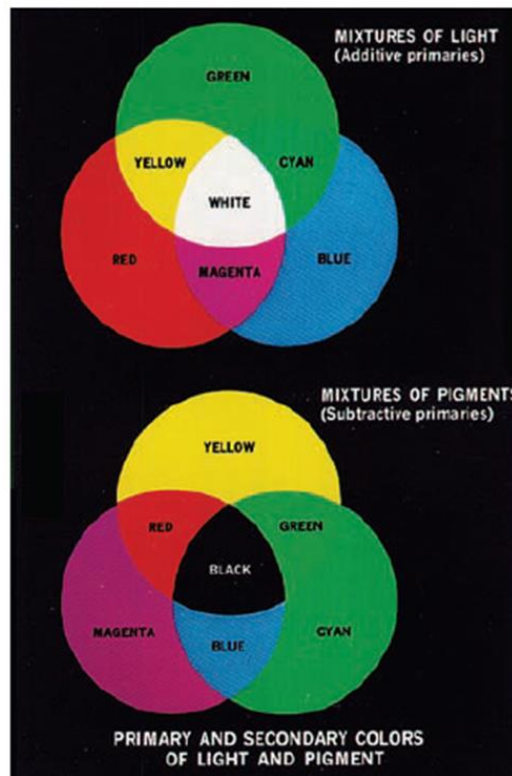

Figure 3. Primary and secondary colors of light and pigments. (Courtesy of the General Electric Co., Lighting Division.)

The conversion from CMY to CMYK starts by letting...

$$K = \min(C, M, Y) \qquad (1.3)$$

If $K = 1$, then we have black, with no color contributions, from which it follows that

$$C = 0$$
$$M = 0 \qquad (1.4)$$
$$Y = 0$$

Otherwise,

$$C = (C - K)/(1 - K)$$
$$M = (M - K)/(1 - K) \qquad (1.5)$$
$$Y = (Y - K)/(1 - K)$$

Where all values assumed to be in the range [0,1]. The conversions from CMYK back to CMY are:

$$C = C * (1 - K) + K$$
$$M = M * (1 - K) + K \qquad (1.6)$$
$$Y = Y * (1 - K) + K$$

As mentioned earlier in this section, all computations in the previous equations are carried out on a pixel-by-pixel basis. By utilizing Equation (1. 2) for bidirectional conversions between CMY and RGB, we establish a "bridge" for converting between RGB and CMYK and vice versa.

It's crucial to remember that the conversions outlined here for transitioning between RGB, CMY, and CMYK rely on the collective relationships presented earlier. Various alternative methods exist for converting between these color models, so attempting to mix approaches may yield nonsensical outcomes. Furthermore, colors that appear on monitors often exhibit significant differences when printed unless these devices are correctly calibrated. This general principle applies to colors converted from one model to another.

1.2.   Chemical coloration

Chemical colors are generated through light absorption by pigments, substances characterized by specific chemical compositions. The resulting colors vary depending on the chemical nature of the pigment. Natural pigments can be extracted from colored tissues found in plants, woad, shellfish, or lichens using

appropriate reagents. Regardless of whether they are located within a biological object or outside of it, pigments respond to light in the same manner. Tissues or organisms exhibiting only pigment-based colors lack surface gloss. Moreover, their color remains unchanged when immersed in a medium that does not chemically interact with the pigment[7].

Extracting chemicals from plants and animals, followed by their conversion into dyes and pigments, boasts a history spanning several millennia. It is only within the last 150 years that natural dyes, pigments, and inks have gradually, and then rapidly, been supplanted by-products originating from modern organic chemistry.

In natural colorant, organic and inorganic materials are obtained from vegetable, animal, or mineral sources. Most do not have sanitary restrictions for food, drugs, and cosmetics. An example of these colorants is zinc oxide or carmine extracted from cochineal; they are colors obtained from natural sources. From an economic point of view, natural dyes have certain disadvantages compared to synthetic components, which meet 90% of global demand. Among the most notable disadvantages are their higher cost, lower reproducibility in the different batches since it depends on the quality of the biological material, they have lower dyeing power, they are not very stable to light, heat, and pH changes, and use is not general for all food, pharmaceutical or cosmetic preparations[8].

Among natural organic dyes, there are several chemical groups: Carotenoids, yellow to red colors (carrot, pepper, etc., in some crustaceans and birds), Porphyrins; green-yellow colors (chlorophyll), etc. and Inorganic dyes include zinc oxide, titanium, iron, calcium carbonate, etc.

In the food industry, there are chemical colors called food dyes. The most significant use of colorants is in those products with little color or colorless: jellies,

---

[7] A. N.Dushkina, In Engineered Biomimicry, Elsevier, 2013, pp. 267-303

[8] D. Marcano, introducción a la química de los colorantes, C. D. C. y. Tecnológica, Ed., Academia de Ciencias Físicas, Matemáticas y Naturales, 2018.

soft drinks, liqueurs, candies, etc. The most common dyes are Quinoline Yellow, Patented Blue V, Indigotine, or "indigo carmine," etc[9].

1.3.   Structural coloration

Structural colors arise from light scattering by microstructures, thin films, and even irregular arrays of extremely small particles. Unlike pigments, they are not produced by chemical compounds. Most colors in the animal kingdom result from chemical pigments, with some exceptions. Floral colors, for instance, are primarily chemical in origin. However, there are colors like the warm reds and earthy ochres of sunsets, the blues and greens of ocean water, the colorful colors of rainbows, and the vibrant hues seen in certain minerals, animals, and plants, which owe their existence to purely physical phenomena. These phenomena include refraction, reflection, scattering, interference, and polarization of light. To our eyes, it is indistinguishable whether a color arises from a physical, chemical, or mixed origin. Our visual system is solely stimulated by photons, which appear to emanate from an object but carry no information about the mechanism behind the color production[10].

In nature, the biological examples provide fascinating insights into the two primary mechanisms of physical color formation. Butterflies, in particular, exhibit an astonishing array of vivid colors, which arise from the intricate interplay of light with an extensive range of micro- and nanostructures present in their wings. Likewise, the exocuticles of numerous beetle species boast striking and vibrant hues. The morphology of biological tissues can be linked to three distinct types of photonic structures: periodic multilayered reflectors, diffraction gratings, and higher-dimensional photonic crystals. These structures play a crucial role in

---

[9] F. naturls, "Tipos de colorantes artificiales para alimentos y sus usos".

[10] A. N.Dushkina, In Engineered Biomimicry, Elsevier, 2013, pp. 267-303

producing the vibrant and diverse colors observed in various species of butterflies and beetles.

Over the past two decades, the growing interest in structural colors has been fueled by the potential to create synthetic photonic structures that mimic those found in nature. Additionally, it has led to the development of new materials for coatings, fabrics, cosmetics, and paints[11] [12]. In order to meet industrial demands, it is crucial to implement simple, fast, efficient, and cost-effective techniques, enabling the production of various shapes and sizes with consistent repeatability and quality.

Industrial applications have primarily focused on producing multilayer structures and block copolymers with periodic refractive index modulation in one direction (referred to as one-dimensional photonic crystals) [13]. Furthermore, there has been progress in fabricating three-dimensional photonic crystals through the self-assembly of colloids. A recent development in the field involves replicating biological templates such as the wings of butterflies and cicadas. Nanofabrication techniques employed for bioreplication include atomic layer deposition, nanocasting, nanoimprinting, and physical vapor deposition.

One of the disadvantages of structural colors is that colors with a chemical origin have been the focus of study and have driven entire industries for millennia. These hues have been crucial in various fields, from technology to art. However, colors of physical origin are gaining significance in modern times due to their environmentally friendly production process. The advantages of producing structural colors, unlike colors produced chemically, they do not involve the release of volatile organic compounds. These compounds contribute to environmental pollution and pose risks to living organisms, even in minuscule

---

[11] S. Y. Shuichi Kinoshita, "Structural Colors in Nature: The Role of Regularity and Irregularity in the Structure," *ChemPhysChem,* vol. 6, no. 8, pp. 1442-1459, 2005.

[12] A. Saito, "Material design and structural color inspired by biomimetic approach," Science and Technology of Advanced Materials, vol. 12, no. 6, 2012.

[13] D. L. R. R. a. O. M. Arno Seeboth, "Thermochromic Polymers-Funtion by Design," *Chemical Reviews,* vol. 114, pp. 3037-3068, 2014.

quantities, by disrupting endocrine systems. This shift towards physical colors aligns with a growing emphasis on sustainable and eco-friendly practices.

1.4.   Goals of the Research

General objectives:

- Development of a nanostructure with plasmonic resonance in the visible to have a structured color easily reproducible and with an accessible reproduction cost.
- Manufacture of a tunable color; explore the use of other thermosensitive materials to control plasmonic resonance and obtain tunable colors in the visible that help us have a possible application as a detector.

Particular objectives:

- Obtain structural color through metallic nanostructures and ultrathin layers of dielectric materials.
- Fabrication of plasmonic nanostructures with conventional thermal evaporation methods.
- Analysis of reflectance, surface, and modeling by the FDTD method.
- Fabrication, characterization, and study of a plasmonic structure with a thin layer of PNIPAM as its spacer between the mirror and the nanoparticles to control and or modify some of its characteristics.
- Study humidity and temperature in a controlled environment with the PNIPAM/nanoparticles sensor.

CHAPTER 2

THEORY

The origin of color in the material can arise from various mechanisms such as absorption/emission, reflection/transmission, scattering, dispersion, or interference. These mechanisms arise from optical properties of materials.

The optical properties are closely related to the electrical and electromagnetic properties of the material. Usually, when we talk about optical properties, we refer to the interaction of electromagnetic radiation with matter. Let us consider a ray of an electromagnetic wave of a single frequency entering a medium from the vacuum. The ray could be reflected, transmitted(refracted), or absorbed *Figure 4* a), and the reflection could be specular or diffuse *Figure 4* b), If the spectrum of frequencies is broader, then some part of the spectrum could be absorbed, and other frequencies could be scattered *Figure 4* c). [14]

---

[14] J. Z. Zhang, "https://home.iitk.ac.in/~anandh/MSE694/NPTEL_Optical%20properties%20of%20Nanomaterials.pdf," 2009. [Online].
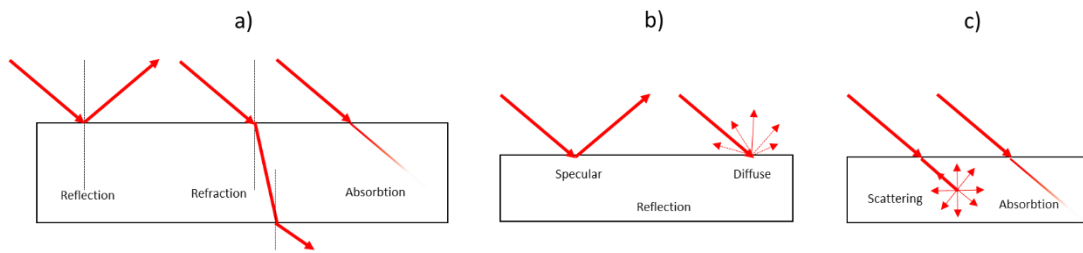
Figure 4 Physical phenomena that a ray of light can experience when in contact with matter.

After providing a concise introduction to the optical mechanisms underlying color formation in materials, this chapter delves into the crucial aspects of electromagnetic response in metals. A thorough understanding of various types of plasmons is essential for this discussion. For this, The chapter is divided into two sections. The first section elucidates the phenomena that underlie the concept of plasmonics, culminating in a detailed exploration of the mechanisms governing Localized Surface Plasmon Resonance. To illustrate, we examine the case of a metallic nanosphere.

The subsequent section, 2.2, delves into growing a thin film and forming metal islands on a smooth surface. Finally, we conclude the chapter with the growth mechanisms of Volmer-Weber model.

2.1.   Plasmonic

This section review Maxwell´s equations, describe the electromagnetic response in metals, and introduce the fundamental excitation of the conduction electron sea in bulk metals: volume plasmons.

To have the description optical properties of metals, we need first remember the basic equation that governs the electromagnetic response, taking as a starting point Maxwell´s equations of macroscopic electromagnetism in the following form:[15]

---

[15] Maier, Stefan A., Plasmonics: Fundamentals and Applications, United Kingdom: Springer, 2007.

$$\nabla \cdot \boldsymbol{D} = \rho_{ext} \tag{2.1}$$

$$\nabla \cdot \boldsymbol{B} = 0 \tag{2.2}$$

$$\nabla \times \boldsymbol{E} = -\frac{\partial \boldsymbol{B}}{\partial t} \tag{2.3}$$

$$\nabla \times \boldsymbol{H} = \boldsymbol{J}_{ext} + \frac{\partial \boldsymbol{D}}{\partial t} \tag{2.4}$$

where **D** is dielectric displacement, **E** is electric field, **H** the magnetic field, and **B** the magnetic induction or magnetic flux density whit the external charge and current densities ρ_{ext} and $\boldsymbol{J}_{ext}$. Because we distinguish external and internal $(\rho, \boldsymbol{J})$ charge and current densities, so that in total $\rho_{tot} = \rho_{ext} + \rho$ and $\boldsymbol{J}_{tot} = \boldsymbol{J}_{ext} + \boldsymbol{J}$. The external set drives the system, whit the internal set responds to the external stimuli. The macroscopic fields **D, E, H** and **B** are linked via the polarization **P** and magnetization **M** by

$$\boldsymbol{D} = \varepsilon_0 \boldsymbol{E} + \boldsymbol{P} \tag{2.5}$$

$$\boldsymbol{H} = \frac{1}{\mu_0} \boldsymbol{B} - \boldsymbol{M}, \tag{2.6}$$

Where ε_0 and μ_0 are the electric permittivity and magnetic permeability of the vacuum. If we consider not magnetic media, then **M** is 0 and **P** is the electric dipole moment per unit volume inside the material by the alignment of microscopic dipoles with the electric field, and is related to the internal charge density via $\nabla \cdot \boldsymbol{P} = -\rho$. Charge conservation $(\nabla \cdot \boldsymbol{J} = -\partial \rho / \partial t)$ further requires that the internal charge and current densities are linked via

$$\boldsymbol{J} = \frac{\partial \boldsymbol{P}}{\partial t} \tag{2.7}$$

The macroscopic electric field includes all polarization effects i.e. the external and induced fields are absorbed into it. This can show via inserting the Equation (2. 5) into (2. 1), leading to

$$\nabla \cdot \boldsymbol{E} = \frac{\rho_{tot}}{\varepsilon_0} \tag{2.8}$$

We will limit ourselves to linear, isotropic and nonmagnetic media. One can define the constitutive relations

$$\boldsymbol{D} = \varepsilon_0 \varepsilon \boldsymbol{E} \qquad (2.9)$$
$$\boldsymbol{B} = \mu_0 \mu \boldsymbol{H}. \qquad (2.10)$$

ε is called the dielectric constant or relative permittivity and $\mu = 1$ the relative permeability of the nonmagnetic medium. The relation between **D** and **E** is possibly defined using the dielectric susceptibility χ, which describes the linear relationship between **P** and **E** via

$$\boldsymbol{P} = \varepsilon_0 \boldsymbol{\chi} \boldsymbol{E}. \qquad (2.11)$$

Using the equations *(2. 5)* and *(2. 11)* into *(2. 9)* yields $\varepsilon = 1 + \chi$.

The last important constitutive linear relation is

$$\boldsymbol{J} = \sigma \boldsymbol{E} \qquad (2.12)$$

where σ is the conductivity.

The electromagnetic phenomena with metals can be described using ε or σ. Experimentally, the electromagnetic phenomena are observed at optical frequencies in terms of the dielectric constant. The optical response of metals depends on the frequency and possibly also on wave vector. If we take account of the non-locality in time and space; it´s possible to get the constitutive relations in the Fourier domain; these depend of wave vector **K** and angular frequency ω.

$$\boldsymbol{D}(\boldsymbol{K}, \omega) = \varepsilon_0 \varepsilon(\boldsymbol{K}, \omega) \boldsymbol{E}(\boldsymbol{K}, \omega) \qquad (2.13)$$
$$\boldsymbol{J}(\boldsymbol{K}, \omega) = \sigma(\boldsymbol{K}, \omega) \boldsymbol{E}(\boldsymbol{K}, \omega) \qquad (2.14)$$

Using Equations (2. 5), (2. 7), (2. 13) and (2. 14), and in the Fourier domain $\partial/\partial t \to -i\omega$, we have the relationship between the relative permittivity and the conductivity, its name is dielectric function.

$$\varepsilon(\boldsymbol{K}, \omega) = 1 + \frac{i\sigma(\boldsymbol{K}, \omega)}{\varepsilon_0 \omega}. \qquad (2.15)$$

For the interaction of light with metals, the form of the dielectric can be simplified to the limit of a spatially local response then. $\varepsilon(\boldsymbol{K} = 0, \omega) = \varepsilon(\omega)$.

It is valid as long as the wavelength λ in the material is significantly longer than all characteristic dimensions, such as the size of the unit cell or the mean free path of the electrons.

The $\varepsilon(\omega) = \varepsilon_1(\omega) + i\varepsilon_2(\omega)$ and $\sigma(\omega) = \sigma_1(\omega) + i\sigma_2(\omega)$ are complex valued functions of angular frequency ω. For reflectivity studies at optical frequencies, ε and index refractive complex $\tilde{n}(\omega) = n(\omega) + i\kappa(\omega)$ of the medium can be experimentally determined and defined $\tilde{n} = \sqrt{\varepsilon}$., we have

$$\varepsilon_1 = n^2 - \kappa^2 \tag{2.16}$$
$$\varepsilon_2 = 2n\kappa \tag{2.17}$$
$$n^2 = \frac{\varepsilon_1}{2} + \frac{1}{2}\sqrt{\varepsilon_1^2 + \varepsilon_2^2} \tag{2.18}$$
$$\kappa = \frac{\varepsilon_2}{2n}. \tag{2.19}$$

κ is called the extinction coefficient and determines the optical absorption of electromagnetic waves propagating through the medium. It is linked to the absorption coefficient α of Beer´s law then

$$\alpha(\omega) = \frac{2\kappa(\omega)\omega}{c}. \tag{2.20}$$

The imaginary part ε_2 of the dielectric function determines the amount of absorption inside the medium. For $|\varepsilon_1| \gg |\varepsilon_2|$, the real part n of the reflective index, quantifying the lowering of the phase velocity of the propagating waves due to polarization of the material. It is determined by ε_1. In the la Equation (2. 15) , the real part of σ determines the amount of absorption, while the imaginary part contributes to ε_1 and therefore to the amount of polarization.

In the absence of external stimuli and combining the curl Equations (2. 3) and (2. 4) the wave equation is

$$\nabla \times \nabla \times \boldsymbol{E} = -\mu_0 \frac{\partial^2 \boldsymbol{D}}{\partial t^2} \tag{2.21}$$

$$K(K \cdot E) - K^2 E = -\varepsilon(K, \omega)\frac{\omega^2}{c^2} E, \qquad (2.\,22)$$

In the time and Fourier domains, respectively $c = \frac{1}{\sqrt{\varepsilon_0 \mu_0}}$ is the speed of light in vacuum. We have two cases that depend on the polarization direction of the electric field vector. In case of a transverse wave, $K \cdot E = 0$, then the generic dispersion relation is

$$K^2 = \varepsilon(K, \omega)\frac{\omega^2}{c^2}. \qquad (2.\,23)$$

For longitudinal wave, (2. 22) implies that

$$\varepsilon(K, \omega) = 0 \qquad (2.\,24)$$

This signifies that longitudinal collective oscillations can only occur at frequencies corresponding to zeros of $\varepsilon(\omega)$. The importance of these expressions finals showing in the next section, where we check the function of dielectric in metals and plasmons.

2.1.1. The Dielectric Function of the free electron gas

The optical properties of metals can be explained by a plasma model for a wide frequency range. In noble metals the wide frequency range is in visible frequencies where occur the interband transition. The electrons that are in the metal oscillate in response to the applied electromagnetic field, and their motion is damped via collisions occurring with a characteristic collision frequency $\gamma = 1/\tau$, τ is known as the relaxation time of the free electron gas, which is typically on the order of $10^{-14} s$ at room temperature, corresponding to $\gamma = 100 THz$.

If an electron of the plasma sea is subjected to an external electric field E then the equation of motion is

$$m\ddot{x} + m\gamma\dot{x} = -eE \qquad (2.\,25)$$

If the driving field is harmonic time dependence $E(t) = E_0 e^{-i\omega t}$ and $x(t) = x_0 e^{-i\omega t}$, that describes the oscillation of the electron. The complex amplitude x_0 incorporates any phase shifts between the driving field and response via

$$x(t) = \frac{e}{m(\omega^2 + i\gamma\omega)} E(t). \qquad (2.\,26)$$

The macroscopic polarization $P = -nex$ is now

$$P = -\frac{ne^2}{m(\omega^2 + i\gamma\omega)} E \qquad (2.\,27)$$

by the displaced electrons. Using the Equation (2. 5) and P yields

$$D = \varepsilon_0 \left(1 - \frac{\omega_p^2}{\omega^2 + i\gamma\omega}\right) E, \qquad (2.\,28)$$

Where $\omega_p^2 = \frac{ne^2}{\varepsilon_0 m}$ is the plasma frequency of the free electron gas, m is electron mass. Then the dielectric function of the electron gas is

$$\varepsilon(\omega) = 1 - \frac{\omega_p^2}{\omega^2 + i\gamma\omega} \qquad (2.\,29)$$

and the dielectric function is complex $\varepsilon(\omega) = \varepsilon_1(\omega) + i\varepsilon_2(\omega)$ then

$$\varepsilon_1(\omega) = 1 - \frac{\omega_p^2 \tau^2}{1 + \omega^2 \tau^2} \qquad (2.\,30)$$

$$\varepsilon_2(\omega) = 1 - \frac{\omega_p^2 \tau}{\omega(1 + \omega^2 \tau^2)}, \qquad (2.\,31)$$

where $\gamma = 1/\tau$ is the collision frequency . when the frequencies is close to ω_p, the product $\omega\tau \gg 1$, leading to negligible damping and $\varepsilon(\omega)$ is predominantly real, and

$$\varepsilon(\omega) = 1 - \frac{\omega_p^2}{\omega^2} \qquad (2.\,32)$$

Now the dielectric function is the undamped free electron plasma, for noble metals in this frequency region is completely altered by interband transitions, leading to an increase in ε_2. In higher frequencies ($1 \leq \omega\tau \leq \omega_p\tau$), the complex reflectance index is predominantly imaginary (leading to a reflection coefficient $R \approx 1$)

2.1.2. Surface Plasmons: Definition

It is necessary to start with a few definitions of plasmonics, given the multidisciplinary nature of plasmonics (*Figure 5*). When the electrons in the metal respond to the electric field and are pushed back to their original position is a restoration force. This restoring force results in oscillations of electron density; this oscillation is known as a plasma oscillation.

The *Plasmons* are quasi-particles that are collective oscillations of conductions in a material, excited by electromagnetic radiation. They are also referred to as `quantized plasma (charge density) waves. ´[16] They are three types of plasmons that are commonly referred to in the literature:

Volumen or Bulk plasmons are longitudinal collective oscillations of the conduction electrons of a metal (*Figure 5* a). If we use the Equation(2. 32) in (2. 23), the dispersion relation of traveling waves evaluates to

$$\omega^2 = \omega_p^2 + K^2 c^2. \qquad (2.\,33)$$

---

[16] A.E. Rider, K. Ostrikov, and S.A. Furman, "Plasmas meet plasmonics Everything old is new again," *The European Physical Journal D,* vol. 66, no. 226, 2012.

For $\omega < \omega_p$ the propagation of the transverse electromagnetic wave is forbidden inside the metal plasma. For $\omega > \omega_p$ the plasma supports transverse waves propagating with a group velocity $v_g = d\omega/dK < c$.

The physical significance of the excitation at ω_p can be understood by considering the collective longitudinal oscillation of the conduction electron gas versus the fixed positive background of the ion core in a plasma slab. We have a homogeneous electric Field $E = \frac{neu}{\varepsilon_0}$ inside the slab, the displaced electrons experience a restoring force and the equation of motion is $nm\ddot{u} = -neE$. Then this leads to $\ddot{u} + \omega_p^2 u = 0$. The plasma frequency ω_p is the natural frequency of a free oscillation of the electron sea, and our derivation frequency assumes that all electrons move in phase; thus, ω_p corresponds to the oscillation frequency in the long-wavelength limit where $K = 0$.

The quanta of these charge oscillations are called plasmons (or volume plasmons, to distinguish them from the surface and localized plasmons). The volume plasmons do not couple to transverse electromagnetic waves and can only be excited by particle impact.

Surface plasmon polaritons (SPPS) are the guided electromagnetic waves that propagate along a metal and dielectric interface, evanescently confined in the perpendicular direction (*Figure 5* b). The amplitude of the SPPs decays exponentially away from the interface in both the media. [17] The physical properties of surface plasmon polaritons can be explained by applying the Maxwell equations in the flat interface between a conductor and a dielectric, mentioned above in section 2.1. and the propagation wave solutions confined to the interface, i.e., with evanescent decay in the perpendicular z-direction.

---

[17] Sarswat, Gagan Kumar and Prashant K., "Interaction of Surface Plasmon Polaritons with Nanomaterials," in *Reviews Plasmonics*, C. D. Geddes, Ed., Baltimore, MD, USA, Springer, 2015, pp. 103-106.

The confinement to the surface demands is that dielectric constant $Re[\varepsilon_1] < 0$ if $\varepsilon_2 > 0$ - the surface waves exist only at interfaces with opposite signs of the real part of their dielectric permittivities, i.e., between a conductor and an insulator. The dispersion relation of SPPs propagating at the interface between the two half-spaces is

$$\beta = k_0 \sqrt{\frac{\varepsilon_1 \varepsilon_2}{\varepsilon_1 + \varepsilon_2}}. \qquad (2.34)$$

This expression is valid for conductors without and with attenuation (i.e., ε_1 can be real or complex) and k_0 is the wave vector of the propagating wave in the vacuum. The component of the wave vector perpendicular to the interfaces in the two media are k_1 and k_2. For confinement of the wave in interface is necessary the continuity of field in both media, the components of field need to meet specific conditions as the confinement to the surface demands that $Re[k_1] > 0$ and $Re[k_2] > 0$, this condition is only fulfilled if $A_2 = A_1 = 0$ (amplitudes of field). Thus, no surface mode exists for TE polarization. Surface plasmon polaritons only exit for TM polarization. For coupling of field is necessary special phase-matching techniques such as grating or prim for their excitation via three-dimensional beams.

For regime of large wave vectors, the frequency of the SPPs approaches the characteristic surface plasmon Frequency

$$\omega_{sp} = \frac{\omega_p}{\sqrt{1 + \varepsilon_2}} \qquad (2.35)$$

concluding that the radiation into the metal occurs in the transparency regime $\omega > \omega_p$. between the regime of the bound and radiative modes, a frequency gab region with purely imaginary β prohibiting propagation exists.
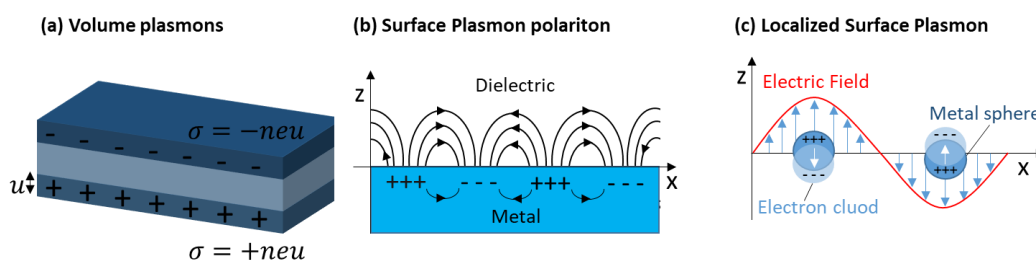
Figure 5 Comparative sketches of (a) volume plasmon [15], (b)surfaces Plasmon Polariton; (c) Localised surface plasmon.[18][16]

2.1.3. Localized Surface Plasmon Resonance (LSPR)

The excitation plasmonic by nanostructures (nanoparticles) is localized surface plasmons that are non-propagating excitations (no wave vector) of the conduction electrons of metallic nanostructures coupled to the electromagnetic field (*Figure 5*). The curved surface of the particle exerts an effective restoring force on the drive electrons so that resonance can arise, leading to field amplification inside and in the near-field zone outside the particle. This resonance is called the localized surface plasmon or short localized plasmon resonance. This resonance is the stimulus-response of the system by external excitation of a particular frequency (in this work, by optical stimulus). Another consequence of the curved surface is that plasmon resonances can be excited by direct light illumination, and the reflection at optical frequencies can be distorted due to interband transitions by the plasmon resonances.

To explain the term LSPR the best way is to consider the case of a metallic nanosphere embedded in a homogeneous medium, where we used the *quasi-static approximation* $d \ll \lambda$, i.e. the particle is much smaller than the wavelength of light in the surrounding medium. Here the phase of the harmonically oscillating electromagnetic field is practically constant over the particle volume so that one

[18] Duyne, Katherine A. Willets and Richard P. Van, "Localized Surface Plasmon Resonance Spectroscopy," *Annu. Rev. Phys. Chem,* vol. 58, p. 267–97, 2007.

can calculate the spatial field distribution by assuming the simplified problem of particles in an electrostatic field. This case describes the optical properties of nanoparticles of dimensions below 100nm.

We start with a homogeneous, isotropic sphere of the radius located at the origin in a uniform static electric field $E = E_0\hat{z}$ (*Figure 6*). The surrounding medium is isotropic, and non-absorbing with a dielectric constant ε_m, and the field lines are parallel to the z-direction at a sufficient distance from the sphere. The dielectric response of the sphere is the dielectric function $\varepsilon(\omega)$.
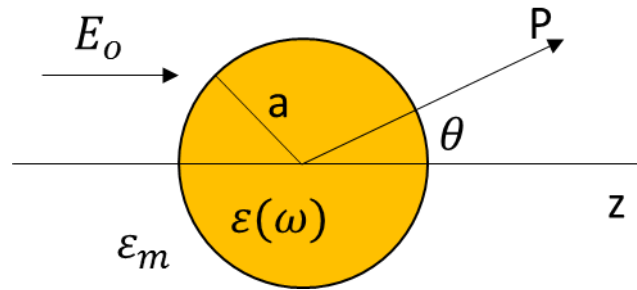
Figure 6 Sketch of a homogeneous sphere placed into an electrostatic field, where $\varepsilon(\omega)$ is dielectric function, ε_m is dielectric constant surrounding medium. [15]

The electrostatic problem of a metallic sphere is resolved using the Laplace equation for the potential $\nabla^2\Phi = 0$, to calculate the electric field $E = -\nabla\Phi$. Due to the azimuthal symmetry of the problem using spherical coordinates, the general solution is [19]

$$\Phi(r, \theta) = \sum_{l=0}^{\infty}\left[A_l r^l + B_l r^{-(l+1)}\right]P_l(cos\theta), \qquad (2.\ 36)$$

where $P_l(cos\theta)$ are the Legendre Polynomials of order l, and θ the angle between the position vector **r** at point P and the z-axis. Separating the general solution (2. 48) , the potentials Φ_{in} inside and Φ_{out} outside the sphere can be written as

[19] J. D. Jackson, Classical Electrodynamics, vol. 3rd edition, John Wiley & Sons, 1999.

$$\Phi_{in}(r,\theta) = \sum_{l=0}^{\infty} A_l r^l P_l(cos\theta) \tag{2.37}$$

$$\Phi_{out}(r,\theta) = \sum_{l=0}^{\infty} B_l r^l + C_l r^{-(l+1)} P_l(cos\theta). \tag{2.38}$$

The coefficients A_l, B_l, C_l are determinate by boundary condition at $r \rightarrow \infty$ an at the sphere surface $r = a$. Then $\Phi_{out} \rightarrow -E_0 z = -E_0 r cos\theta$ as $r \rightarrow \infty$ demands that $B_1 = -E_0$ and $B_1 = 0$ for $l = 1$. For $r = a$ the tangential components of electric field and the normal components of the displacement field are

$$-\frac{1}{a}\frac{\partial\Phi_{in}}{\partial\theta}\bigg|_{r=a} = -\frac{1}{a}\frac{\partial\Phi_{out}}{\partial\theta}\bigg|_{r=a} \tag{2.39}$$

y

$$-\varepsilon_0\varepsilon\frac{\partial\Phi_{in}}{\partial\theta}\bigg|_{r=a} = -\varepsilon_0\varepsilon_m\frac{\partial\Phi_{out}}{\partial\theta}\bigg|_{r=a} \tag{2.40}$$

calculationing the boundary conditions, the potentials evaluate are[19]

$$\Phi_{in} = \frac{3\varepsilon_m}{\varepsilon + 2\varepsilon_m} E_0 r cos\theta \tag{2.41}$$

$$\Phi_{out} = -E_0 r cos\theta + \frac{\varepsilon - \varepsilon_m}{\varepsilon + 2\varepsilon_m} E_0 a^3 \frac{cos\theta}{r^2}. \tag{2.42}$$

physically Φ_{out} describes the superposition of the applied field and that of a dipole located at the particle center. Rewrite Φ_{out} by introducing the dipole moment **p** as

$$\Phi_{out} = -E_0 r cos\theta + \frac{\boldsymbol{p}\cdot\boldsymbol{r}}{4\pi\varepsilon_0\varepsilon_m r^3} \tag{2.43}$$

$$\boldsymbol{p} = 4\pi\varepsilon_0\varepsilon_m a^3 \frac{\varepsilon - \varepsilon_m}{\varepsilon + 2\varepsilon_m} E_0 \tag{2.44}$$

We observed that the applied field induces a dipole moment inside the sphere of magnitude proportional to $|\boldsymbol{E_0}|$. Where the polarizability α is defined via $\boldsymbol{p} = \varepsilon_0 \varepsilon_m \alpha \boldsymbol{E_0}$, and it is written as

$$\alpha = 4\pi a^3 \frac{\varepsilon - \varepsilon_m}{\varepsilon + 2\varepsilon_m}. \qquad (2.\ 45)$$

This result is the (complex) polarizability of a small sphere of sub-wavelength diameter in the electrostatic approximation.

Figure 6 shows the electromagnetic field E_0 that incident on a homogenous sphere with frequency ω (in energy units) and the dielectric constant $\varepsilon(\omega)$. The polarizability that experiments the sphere is α, but enhancement polarizability is when the resonant is under the condition $|\varepsilon + 2\varepsilon_m|$ is a minimum ,we have the most oscillating changes involved. Which for the case of small or slowly-varying $Im[\varepsilon]$ around the resonance simplifies to

$$Re[\varepsilon(\omega)] = -2\varepsilon_m. \qquad (2.\ 46)$$

This relationship is the Frohlich condition and the associated mode (in an oscillating field) of the dipole surface plasmon of the metal nanoparticles.

For a sphere consisting of a Drude metal with a dielectric function $\varepsilon(\omega)$ located in the air, the Frohlich criterion is met at frequency $\omega_0 = \omega_p/\sqrt{3}$ further expresses the strong dependence of the resonance frequency on the dielectric environment: The resonance red-shifts as ε_m is increased. Metal nanoparticles are thus ideal platforms for optical sensing of changes in refractive index.

2.2. Modes growth of a thin film and formation of metal island onto a smooth surface.

In the past, theoretically and experiments have studied the process of deposit of thin film where growing this film has different mechanisms. In general, are accepted three possible modes of crystal growth film on surfaces are illustrated schematically in *Figure 7*. These mechanisms are growth modes, and

your names are; layer-by-layer or Frank-van der Merve (FM). It is when the film atoms are more strongly bound to the substrate than to each other, and we have a layer fully completed before the next layer starts to grow (*Figure 7* a); Island or Vollmer-weber (VW) is when the film atoms are more strongly bound to each other than to the substrate, and we have islands nucleate and grow directly on the substrate surface (*Figure 7*Figure 7 c); layer-plus-island or Stranski-Krastanov (SK) is between case FM and VW, after the formation of a complete layer, the growth of islands takes place *Figure 7* b).[20]

| Layer-by layer growth (Frank-van der Merve) | Layer plus island growth (Stranski-Krastanov) | Island growth (Vollmer-Weber) | |
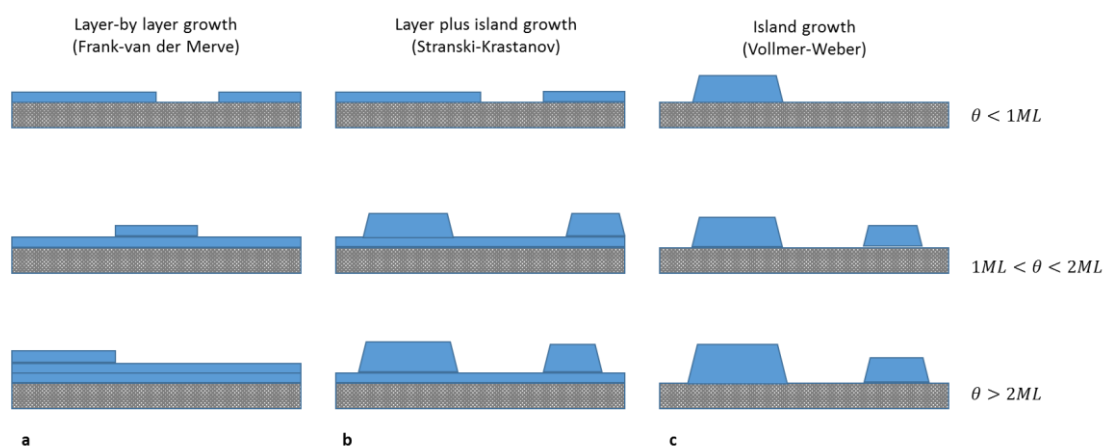
Figure 7 Schematic representation of the three main growth modes, where θ is the adsorbate coverage that characterizes the surface concentration of adsorbed species expressed in monolayer (ML) units. One monolayer corresponds to one adsorbate atom or molecules for each 1x1 unit cell of the ideal non-reconstructed substrate surface. The schematic (a) is the layer-by-layer (FM) growth mode, (b) is the layer-plus-island (SK) growth mode, and (c) is Island (VW) growth mode. [20]

We are talking about the thin film when the adsorbate coverage exceeds the monolayer range. The film growth first has the oriented growth of a crystalline film on a single-crystal substrate referred to as epitaxy, which in turn is subdivided into homoepitaxy and heteroepitaxy, the first is when both film and substrate are of the same material, and de second is when film and substrate are different.

[20] V. L. A. S. A. Z. M. K.Oura, Surface Science An Introduction, Osaka and Vladivostok: Springer, 2003, pp. 197,357-363.

The general characteristics involved in growing a thin film are:

- The first starts with the process of random nucleation. In this stage, a grain is placed on a surface and begins to grow.
- The nucleation and growth depend on the temperature in growth and the chemical substratum natural.
- The film growth is controlled by the interplay of thermodynamics and kinetics, where the film growth is understood with the thermodynamic approach in terms of the relative surface energies.
- The nucleation stage can be modified since the film growth is a non-equilibrium kinetic process in which the rate-limiting steps affect the net growth mode.

The growth modes can be understood in terms of surface or interface tension γ, which is the work that must be performed to build a surface (or interface) of unit area. γ. It can also be interpreted as a force per unit length of the boundary, consider the contact point of the film island and the substrate *Figure 8*, where the island wetting angle is φ, and the force equilibrium can be written as

$$\gamma s = \gamma_{s/F} + \gamma_F \cos \varphi, \qquad (2.\ 47)$$

where γs is the surface tension of the substrate surface, γ_F is the surface tension of the film surface, and $\gamma_{s/F}$ is the surface tension of the film/substrate interface. For $\varphi = 0$ we have the case layer-by-layer (FM).

$$\gamma s \geq \gamma_{s/F} + \gamma_F \quad \text{(layer-by-layer growth)} \qquad (2.\ 48)$$

For $\varphi > 0$ corresponding to island growth

$$\gamma s < \gamma_{s/F} + \gamma_F \quad \text{(Island growth)}. \qquad (2.\ 49)$$
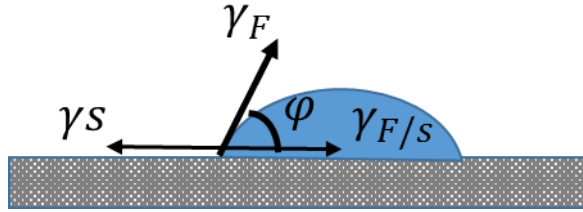
Figure 8 Schematic of a film island on a substrate, the balance of force acting along the substrate surface is shown in the Equation **(2. 47)**.

In the next section, we show the main elementary processes for the forming and growing islands, illustrated schematically in *Figure 7* 7 c) with Volmer-Weber.

2.1.4. Mechanisms during coalescence Volmer-Weber thin films

The forming of islands starts when atoms arrive from the gaseous phase at a rate R and become accommodated at the substrate surface as adatoms with a bound energy E_{ads}, and create a population of single adatoms n_1 on the substrate with n_0 sites per unit area. The adatoms migrate over the surface with the diffusion coefficient D; that is, it is responsible for moving the particles somewhere on the surface (*Figure 9* b), $D = \left(\frac{v}{4n_0}\right)\exp\left(-\frac{E_{diff}}{k_B T}\right)$. The adatom motion along the surface can be visualized as a random site-to-site hopping process, where v is the hopping frequency , E_{diff} is the energy of diffusion i.e., is the difference in potential energy of the adatom in the equilibrium adsorption site and the transition point, it is the energy necessary for hop of neighboring sites, k_B is the Boltzmann constant, and T the temperature.[21]

D can be lost when start the following processes (*Figure 9*):

---

[21] V. L. A. S. A. Z. M. K.Oura, Surface Science An Introduction, Osaka and Vladivostok: Springer, 2003, pp. 197,357-363.

- If the substrate temperature is high enough, they are re-evaporated (*Figure 9* a). The re-evaporation is characterized by the residence time $\tau_{ads} = v^{-1}\exp(E_{ads}/k_B T)$.
- The adatoms might become captured by existing clusters or at defect sites such as steps (*Figure 9* e).
- The adatoms might combine with one another to forma cluster (*Figure 9* c). The clusters are metastable and often decay back into individual atoms.
- When the cluster grows in size, it becomes more stable and the probability of its growth is greater than the probability of decay. The *critical island size i* is defined as the minimal size when the addition of just one more atom makes the island stable (*Figure 9* d).
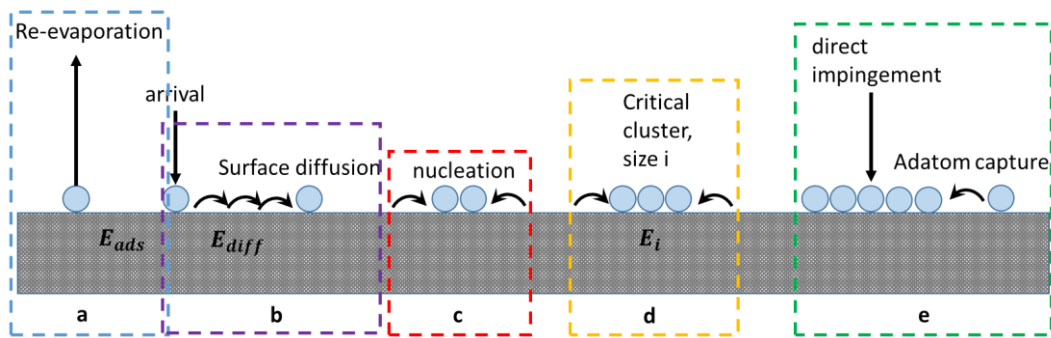
Figure 9 *Schematic diagram that illustrates the atomic processes of what happens by the nucleation and growth of islands on surfaces.*

It is possible explain the decay or formation of the clusters, in terms of the rate equations. The metastable clusters can be described with the fluxes population n_j (number density of j-clusters) of size $j < i$, where i is the critical cluster size.

When an adatom is attached to the cluster of size $j - 1$ then n_j increases, and the flux is $\sigma_{j-1}Dn_{j-1}n_1$. If now decay of the $(j + 1)$-cluster, we have a detachment of the atom from a cluster of size $j + 1$, and the net flux of the decay is $\delta_{j+1}n_{j+1}$. For the processes of decrease n_j, the atoms are attached to j-clusters and transforms in $(j + 1)$-clusters, and net rate is $\sigma_j Dn_j n_1$. If the decay of j-

clusters, then we have $(j-1)$-clusters with a net rate $\delta_j n_j$. where n_1 is the number density of adatoms, D diffusion coefficient, σ is the capability of islands to capture diffusing adatoms, and $\delta_{j+1} \sim D\exp(-\Delta E_j^{j+1}/k_B T)$ the decay rate with ΔE_j^{j+1} is the energy difference between the $(j+1)$-clusters and the j-clusters.

For evaluation of the number density of adatoms, n_1, and that of stable clusters with $j > i$, denoted n_x, we have the rate equations:

$$\frac{dn_1}{dt} = R - \frac{n_1}{\tau_{ads}} + \left(2\delta_2 n_2 + \sum_{j=3}^{i} \delta_j n_j - 2\sigma_1 D n_1^2 - n_1 \sum_{j=2}^{i} \sigma_j D n_j \right)$$
$$- n_1 \sigma_x D n_x \tag{2. 50}$$

$$\frac{dn_j}{dt} = n_1 \sigma_{j-1} D n_{j-1} - \delta_j n_j + \delta_{j+1} n_{j+1} - n_1 \sigma_j D n_j \tag{2. 51}$$

$$\frac{dn_x}{dt} = n_1 \sigma_i D n_i. \tag{2. 52}$$

The Equation (2. 50) describes the time variation of the adatom density n_1, where showing an increase in n_1 due to deposition with a flux R and decrease due to desorption at a rate n_1/τ_{ads}. The terms bracketed together $2\delta_2 n_2$ and $2\sigma_1 D n_1^2$ stand for the decay and formation of dimers, the factor 2 indicate that in each of these processes adatoms are supplieds or consumed as pairs, the σ terms are for the decay and formation of clusters of size from 3 to i, and the last term represent the net capture rate of stable clusters larger than i.

For the density of metastable clusters of size j, Equation (2. 51) shows the terms that have been discussed previously, and Equation (2. 52) describes the growth of the stable cluster density n_x due to attachment of adatoms to critical-size clusters.

The integration of Equations (2. 50)-(2. 52) gives the time evolution of island and adatom densities. For the case $i = 1$ (i. e. when a dimer is already a stable cluster)and sufficiently low temperatures can see the dynamic behavior of

the density of adatoms (n_1) and islands (n_x). The results are shows in *Figure 10* which is divided into four coverage regimes: L,I A and C.
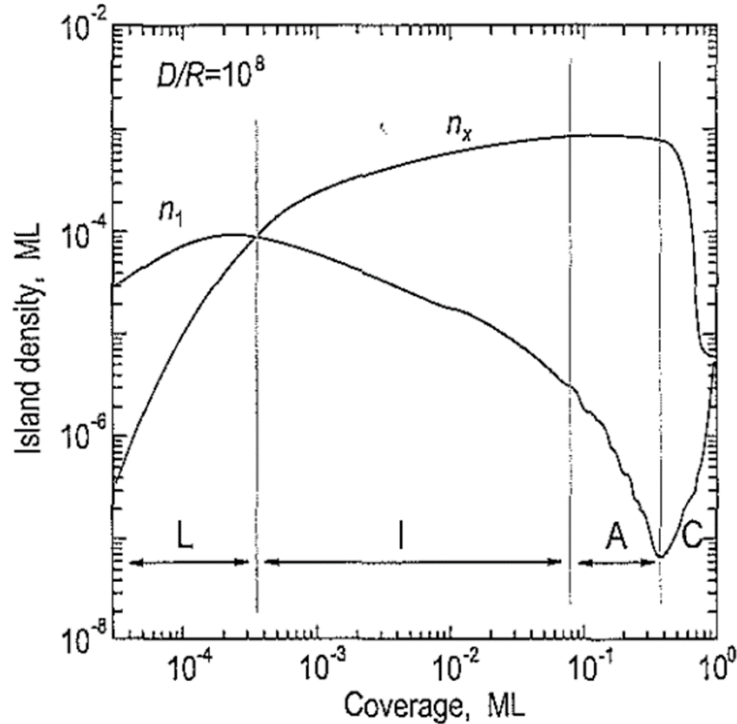
Figure 10 The L labeled is low-coverage nucleation regime, I is intermediate-coverage regime, A is aggregation regime, and C is coalescence and percolation regime. The number density of adatoms (n_1) and islands (n_x) versus coverage in the case $i = 1$ and $D/R = 10^8$. [21]

In regime A the adatom density is much higher than the island density, so the probability of island nucleation far exceeds the probability of an adatom becoming incorporated into an existing island, here $n_1 \propto \theta$ and $n_x \propto \theta^3$. Regime I is intermediate-cover, and it is in the course of deposition, the number density of islands increases until it becomes comparable to the density of adatoms. Here the adatom density peaks and begins to decrease ($n_1 \propto \theta^{-1/3}$), and island density increases more slowly ($n_x \propto \theta^{1/3}$). The aggregation regime passes when the density of islands increases so that the mean island separation is equal to the mean free path of migrating adatoms. The island´s growth and the island density attains a saturate value. This showing in regimen A (*Figure 10*) and usually occurs at a coverage between 0.1 and 0.4 ML. The last regime C is the coalescence and percolation; here, the islands join together (coalesce) and percolate, meaning

that the island number density decrease and second-layer growth starts with adatom density again increases.

Experimentally these processes are controlled for temperature, control pressure in the method of deposit and rate deposit; this last showed experimentally that while more slowly evaporation, we have more material aggregated for thicknesses the structure.[22]

---

[22] R. S. a. G. Scott, "The Structure of Evaporated Metal Films and Their Oprical Properties," *Journal of the Optical Society of America,* vol. 40, no. 4, pp. 203-211, April,1950

CHAPTER 3

METHODS

Utilizing software for structural modeling presents a significant advantage in terms of time efficiency, allowing us to generate a wide array of potential outcomes swiftly. These results empower us to analyze their performance under various conditions comprehensively. This chapter outlines the modeling approach employed for our nanostructures, utilizing the commercial software package Lumerical Solution. Subsequently, we conduct a comparative analysis between the data obtained from simulation and experimental results.

In the experimental phase, the choice of fabrication method for a given nanostructure hinges on its specific attributes, including material composition and intended form. Thus, in Section 3.2, we provide a comprehensive description of the various deposition methods employed throughout this thesis.

3.1.   FDTD Simulations

Finite Difference Time Domain Modeling

Lumerical FDTD (Finite difference time domain) is a commercial software package (Lumerical Solution Inc.). This software has tools for designers to

nanophotonic model devices, processes, and materials and offers multiphysics-style capabilities and workflows to model optical. FDTD can calculate physical quantities, such as the complex pointing vector and the transmission/ reflection of light.

The Finite-Difference Time-Domain (FDTD) method is a state-of-the-art method for solving Maxwell's equations in complex geometries. FDTD solves for the electric and magnetic fields as a function of time; the essential mathematical and physical formalism behind the FDTD algorithm is Maxwell´s equations. FDTD solve Maxwell´s curl equations in non-magnetic materials[23] [24]:

$$\frac{\overrightarrow{\partial D}}{\partial t} = \nabla X \vec{H}$$

$$\vec{D}(\omega) = \varepsilon_0 \varepsilon_r(\omega) \vec{E}(\omega) \qquad (3.\,1)$$

$$\frac{\overrightarrow{\partial H}}{\partial t} = -\frac{1}{\mu_0} \nabla X \vec{E}$$

where H,E and D are the magnetic, electric and displacement fields, $\varepsilon_r(\omega)$ is the complex relative dielectric constant ($\varepsilon_r(\omega) = n^2$, where n is the refractive index).

In the three dimensions, Maxwell equations have six electromagnetic field components: Ex, Ey, Ez and Hx, Hy, and Hz. If we assume that the structure is infinite in the z dimension and that the fields are independent of z

$$\Rightarrow \quad \varepsilon_r(\omega, x, y, z) = \varepsilon_r(\omega, x, y)$$

$$(3.2)$$

$$\frac{\partial \vec{E}}{\partial z} = \frac{\partial \vec{H}}{\partial z} = 0$$

---

[23] A. Lumerical, "https://optics.ansys.com/hc/en-us/articles/360034914633-FDTD-solver," [Online].

[24] R. J. L. Karls. Kunz, The Finite Difference time Domain Method for Electromagnetics, Boca Raton London New york Washington, D. C.: CRC press, 1993, p. 11.

Then Maxwell´s equation split two independent sets of equations composed of three vector quantities each which can be solved in the x-y plane only. These are termed the TE (transverse electric), and TM (transverse magnetic) equations. We can solve both sets of equations with the following components.

TE: Ex,Ey,Hz

TM: Hx,Hy,Ez

For example, in the TM case, Maxwell´s equations reduce to:

$$\frac{\partial D_z}{\partial t} = \frac{\partial H_y}{\partial x} - \frac{\partial H_x}{\partial y}$$
$$D_z(\omega) = \varepsilon_0 \varepsilon_r(\omega) E_z(\omega)$$
$$\frac{\partial H_z}{\partial t} = -\frac{1}{\mu_0} \frac{\partial E_z}{\partial y}$$
$$\frac{\partial H_y}{\partial t} = \frac{1}{\mu_0} \frac{\partial E_z}{\partial x}$$

(3.3)

The FDTD method solves these equations numerically on a discrete spatial and temporal grid; this means that the electric and magnetic fields are discrete in space and time. Each filed component is solved at a slightly different location within the grid cell (Yee cell) Figure 11. The Data collected from the FDTD solver is automatically interpolated to the origin of each grid point.
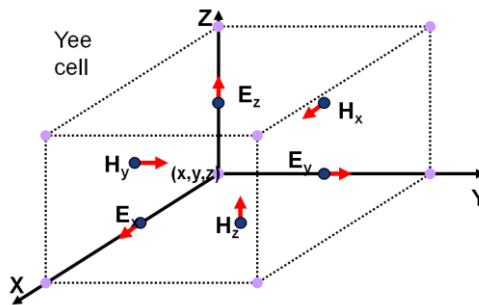
Figure 11 Yee cell is used to discretize Maxwell´s equations in space. The grid shows the placement of electrical and magnetic fields.

Dispersive materials with tabulated refractive index (n,k) data as a function of wavelength can be incorporated by using the multi-coefficient material models

that automatically generate a material model based on the tabulated data. The FDTD solves a number of different types of sources; in this work, we used plane waves. The FDTD uses a rectangular, Cartesian-style mesh Figure 12. The fundamental simulation quantities (material properties and geometrical information, electric and magnetic fields) are calculated at each mesh point
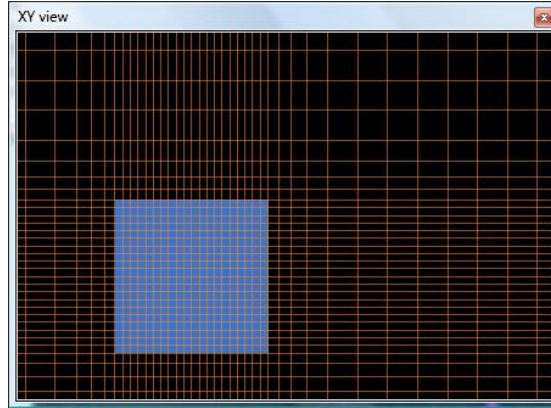
Figure 12 FDTD solution provide a simple mesh accuracy setting that targets a minimum points per wavelength in all regions of the simulation and automatically adapts to the reflective index of the different materials.

Suppose we wanted quantities that depend of fields as a function of frequency ($\vec{E}(\omega)$) or wavelength ($\vec{E}(\lambda_o)$), such as the Poynting vector, transmission, reflection, absorption and scattering cross section. We need to calculate the frequency domain response by Fourier transform[25].

$$\vec{E}(\omega) = \int_0^{T_{SIM}} e^{i\omega t} \vec{E}(t) dt$$

$$\lambda_0 = \frac{c}{f} = \frac{2\pi c}{\omega}$$

(3.4)

FDTD can calculated this Fourier transform while the simulation is running. FDTD solutions use frequency domain monitors to perform the discrete Fourier transforms, while time domain monitors can record the fields.

---

[25] A. Lumerical, "https://optics.ansys.com/hc/en-us/articles/360044941874-FDTD-Algorithm-Getting-Frequency-Domain-Results," [Online].

FDTD is so versatile that it can have a wide range of applications. Including photonic crystal, plasmonics, nano-patterned solar cells, nanoparticles scattering and absorption, grating, metamaterials, and integral optics, to name just a few; all of these applications involve wavelength-scaled structures[26] [27] *Figure 13*.
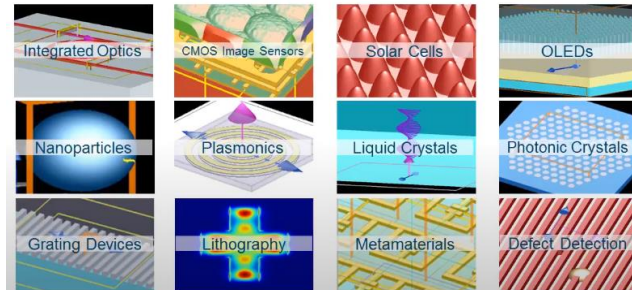
Figure 13 Structures that are possible to model and calculate in FDTD

3.2.   Nanofabrication

E-beam Evaporation

E-Beam evaporation is a physical vapor deposition (PVD) technique[28]. It is used to deposit thin films, typically up to 1-micron thickness, at the normal angle. The electron beam (E-beam) is generated from a filament and steered via electric and magnetic fields to strike source material (e.g., pellets of Al); this material is melted and vaporized within a vacuum environment, and the rate of evaporation increases or decreases with the energy input of the electron gun *Figure 14*. The sample is put on the holder and rotated with a rate constant this help have a thin film uniform. When the material evaporation arrives at the top chamber with the desired evaporation rate, the shutter opens, and the material deposit starts on the substrate; the thickness is monitored and measured by a sensor after having

[26]   A.   Lumerical,   "https://optics.ansys.com/hc/en-us/articles/360034914633-FDTD-solver," [Online].

[27]   A.   Lumerical,   "https://optics.ansys.com/hc/en-us/articles/360045465293-FDTD-Algorithm-The-FDTD-Method," [Online].

[28]   A.   international,   "https://www.ajaint.com/what-is-e-beam-evaporation.html," [Online].

the required thickness, the shutter closes immediately, and the deposit on the substrate is stopped.
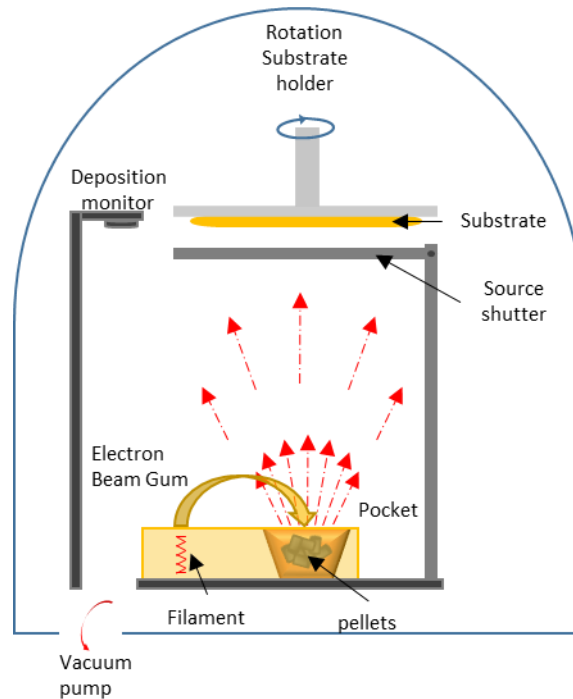
Figure 14 Schematic of the Electron Beam Evaporation

In this work, the AJA Electron Beam Evaporation System is used; this one has five pockets lineal E-beam source on a convenient slide mechanism for loading and service; it also features turbo-pumped vacuum load-lock, the e-beam has two chambers, the small chamber is the first entry for has soon vacuum, the big chamber be at a pressure of up to 10-8 Torrs. The material that can be deposited by AJA E-beam are metals (Al, Ag, Au, Cr, Ni, Ti, and Cr). The E-beam is shown in *Figure 15*.
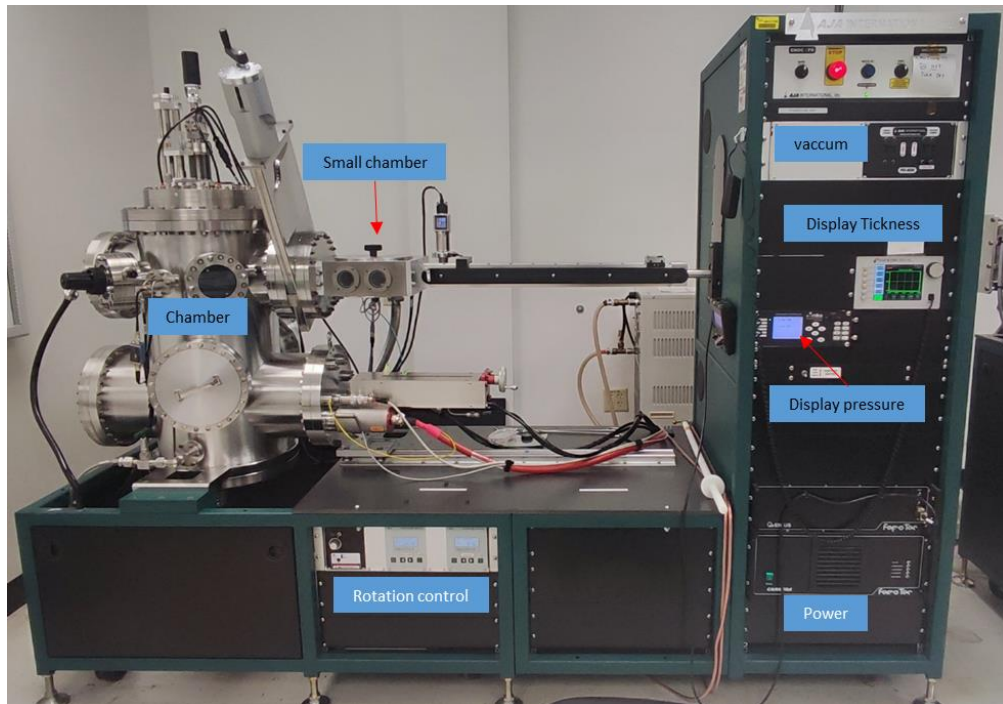
Figure 15 AJA Electron Beam Evaporation System

ALD

Atomic Layer Deposition (ALD) is a technique that grown ultra-thin film layer, monolayer by monolayer everywhere on sample surface. Different materials can be deposited by ALD, the materials typically deposited are Oxides $(Al_2O_3$, TiO_2, HfO_2, SiO_2,Ta_2O_5, ZnO,..); Nitrides(AlN, TiN, HfN, TaN,..); Fluorides(AlF_3, MgF_2,..); Sulfides(ZnS,MoS_2,…); Metals(Pt, Ni, Ru,...). The process of monolayer deposit is through of chemical reaction a typical reaction is the formation of aluminum oxide (Al_2O_3) from trimethylaluminum or TMA Al(CH3)3, and water[29]. These chemicals elements are called precursors and are used for ALD depositions. The growth process of Al_2O_3 is illustrated in *Figure 16*. The process starts when the water made to contact with the surface; it is absorbed molecules of oxygen and hydrogen, making a hydroxyl group (OH) *Figure 16* a); when the trimethylaluminum(TMA) into the chamber, it reacts with the OH group,

---

[29] A. S. R. C. NanoFabrication Facility, "https://asrc.gc.cuny.edu/content/uploads/sites/4/media/member-resources/equipment-procedure-and-policies/deposition/ALD-SOP.pdf," NanoFabrication Facility, ADVANCED SCIENCE RESEARCH CENTER , 25 January 2018. [Online].

removing a methyl group and replacing with a molecule of H and liberating methane group (*Figure 16* b)). This process happens on everything surface *Figure 16* b). The excess TMA and methane groups are removed with nitrogen flowing over the surface (*Figure 16* c)). Next step, the water is introduced into the chamber, and it reacts with the methyl groups on the deposited aluminum atoms them removing the methyl groups and forming both Al-O-Al bridges and new hydroxyl groups (*Figure 16* d), e)). The methane product made by the chemical reactions is pumped out of the chamber. Finally, we have a new layer of hydroxyl (OH) for the following layer of aluminum atoms (*Figure 16* f)) and the all process starts again.
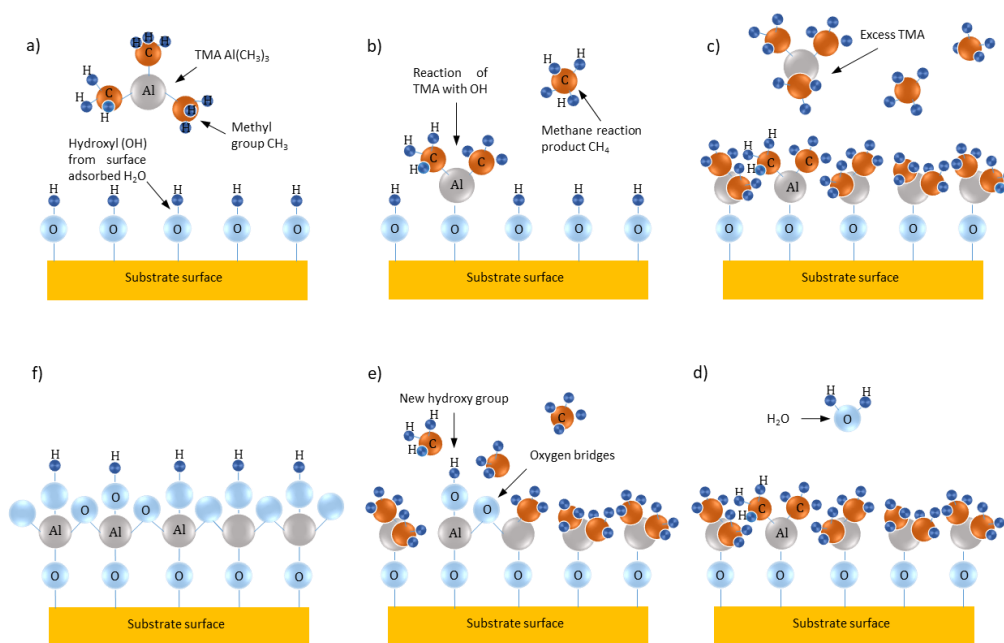
Figure 16. Process of deposit of Al_2O_3 by technique grown Atomic Layer Deposition (ALD).

The Atomic Layer Deposition (ALD) System-Ultratech Savannah S200 is used in this work to deposit thin films of 10 nm thickness. We have a highly controlled, layer-by-layer methodology. The scheme ALD system is shown in *Figure 17*. Where the deposits are made in the chamber, usually two precursors are used for the deposition; in this work, we used TMA and H2O, and inert gas N2; the precursors and gas inert are introduced for the same duct, and valves control them through a computer that decides which gas passes and which does not then the excess of material is expelled de chamber, the process is with the

hot walls, the temperature is the same everywhere in the chamber. The final thickness is controlled by cycles where one cycle makes a monolayer; this process replays until the final thickness. A cycle consists of the process previously described and shown in *Figure 177*. The materials that can be deposited at the NanoScience Technology Center lab are Oxides: Al2O3, TiO2, and SiO2.
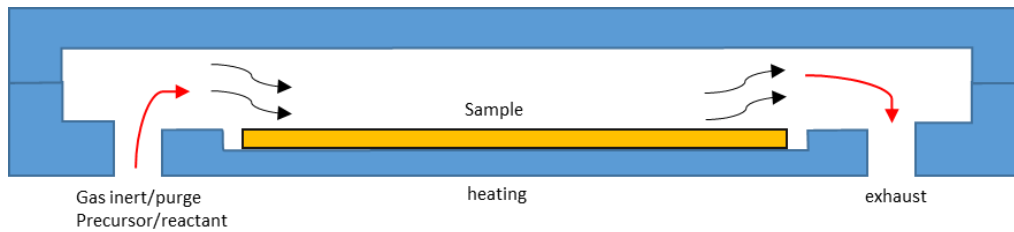
Figure 17 .Scheme of Atomic Layer Deposition , the ALD is always heating inside

Spin coating

Spin coating is a technique for depositing a homogeneous organic and uniform thin film on a flat substrate. This method is economical, easy, and reproducible, with low-temperature ability to create a good-quality thin-thickness film. The thin film thickness depends on the spinning speed, solution viscosity, and evaporation rate. *Figure 18* shows the schematic representation of the spin coating process. The process of spin coater is possibly explained by four stages: solution deposition, spin-up, spin-off, and solvent evaporation. In the 1st stage, a flat substrate is put on the spin coater, and deposited the coating solution on the center of the flat substrate. In the 2nd stage, the substrate starts to rotate and speed up to the maximum programmed rate. In the 3rd stage, the substrate is spinning at a constant rate, and together with the viscosity of the solution, controls the solution thinning to get a uniform thin film. The 4th stage is evaporation; it happens from the start process and culminates whit completing

evaporation of the entire solvent; it controls the thinning characteristics of the coating, producing a solid film[30].

$$\frac{d\omega}{dt} \neq 0$$

1st stage

2nd stage

$$\omega = 0$$

$$\omega = cst.$$

4th stage

3rd stage
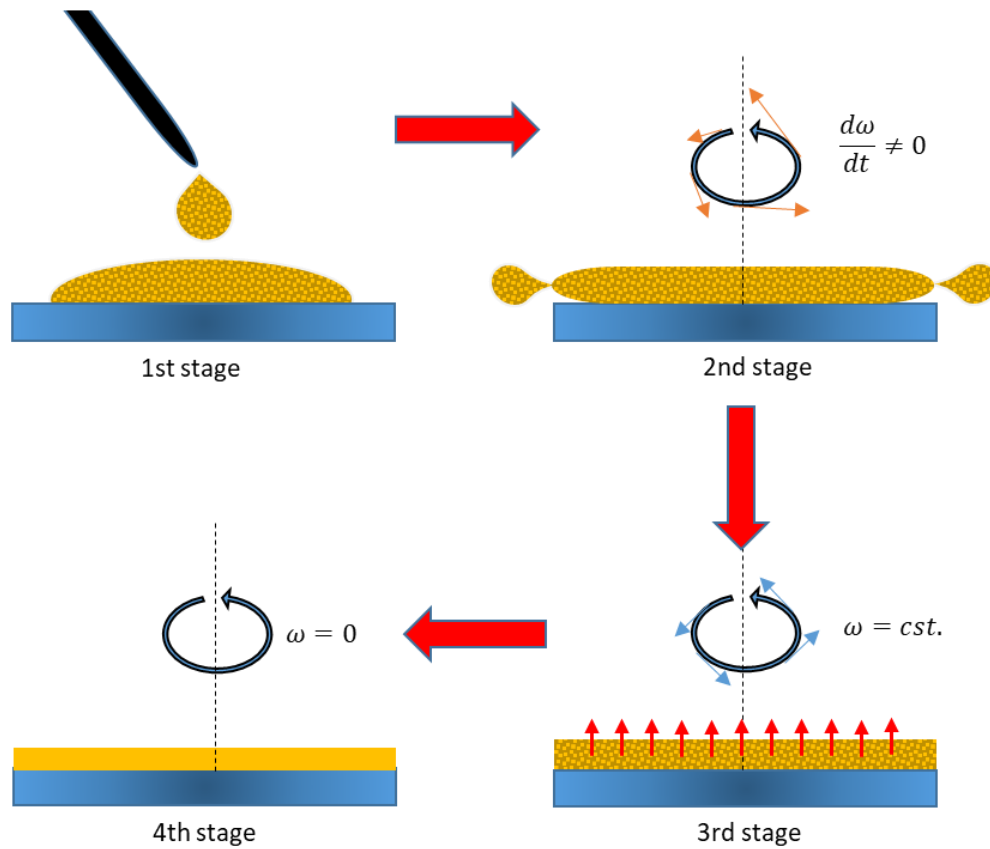
Figure 18 Spin coating process, we have four stages: a dispense stage, substrate acceleration, constant rate, and solvent evaporation.

Sputtering

Sputtering is a technique used to deposit thin films of a material onto a surface (substrate). Sputtering is defined as the ejection of particles (atoms, ions, and clusters) from a surface that is bombarded by energetic ions. The term "sputtering" is commonly used to refer to erosion processes induced by the impact of atoms, molecules, neutrons, or electrons. There are two concepts "chemical" and "physical" sputtering. Chemical sputtering involves chemical reactions between the incoming beam particles and target material, e. g., the

---

[30] M. R. a. M. A. R. Mohammad Meftahul Ferdaus, "Design and Fabrication of a Simple Cost Effective Spin Coater for Deposition of Thin Film," *Advances in Environmental Biology,* pp. 729-733, 2014.

45

formation of compounds on the surface, which are subsequently sputtered as a result of the continuous particle irradiation. Physical sputtering is the process in which the energetic particles penetrate a certain distance into the solid, and they will give rise to collision cascades or thermal spikes, resulting in the ejection of the target material. Schematically the process is shown in Figure 19. In this work, we used sputtering, how physical sputtering[31].
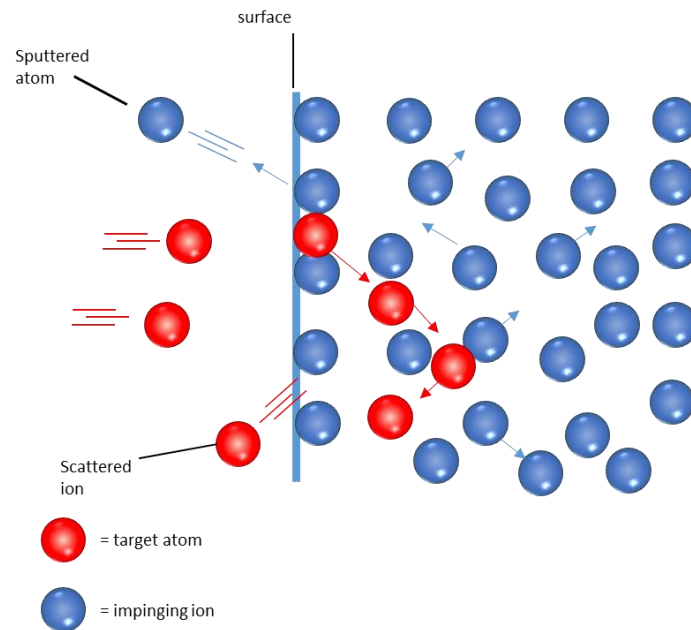
Figure 19 scheme of collisions of ions and atoms into the bulk material. The upper impinging ion is implanted into the bulk material where it gives rise to a collision sequence leading to the ejection of a substrate atom, i.e., sputtering. The lower impinging ion is reflected against the substrate atoms.

The concept of magnetron sputtering appear when sputtering process was combined with magnetic fields. The principles process is presented in *Figure 20*. The idea is to enhance the ionization of the atoms to hit the target so that the number of sputtered material is increased compared to conventional sputtering. This is achieved by introducing magnetic fields close to the target surface with the help of horseshoe magnets arranged at the back side of the magnetron, as

---

[31] M. Braun, "Magnetron Sputtering Technique," in *Handbook of Manufacturing Engineering and Technology*, Sweden, 2015, pp. 2929-2957.

shown in *Figure 20*. The discharge which is created in front of the target is often denoted as the magnetron "plasma "as ions and electrons are separated here.
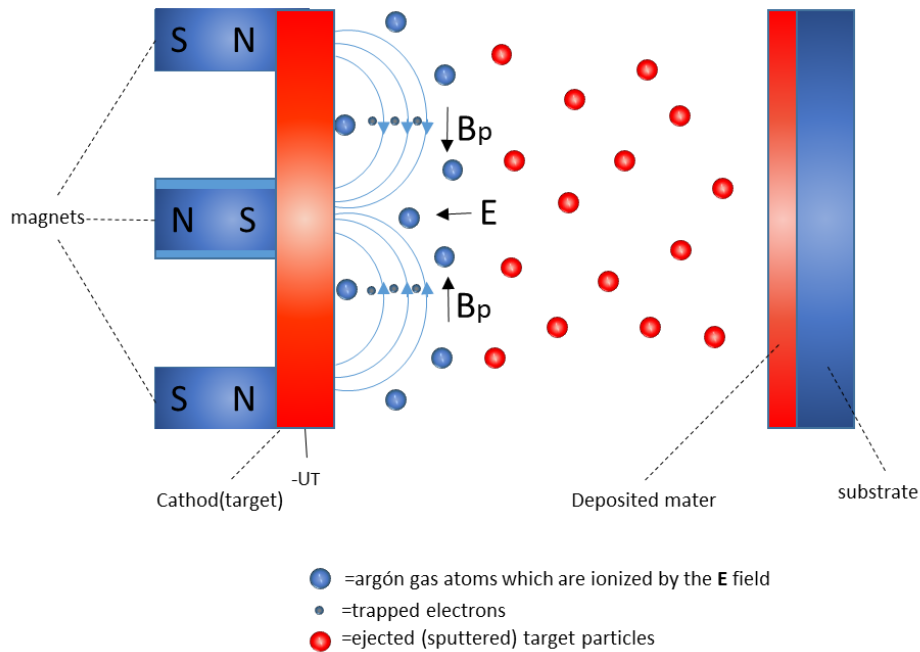
Figure 20 Side view of a "magnetron" (left side of the figure) illustrating the principles of magnetron sputtering by showing the arrangement of the magnets behind the target which is held at a negative potential $-U_T$. This gives rise to the electric field **E** and the magnetic field lines, where **B** $_p$ is the magnetic field perpendicular to the electric field **E** [32].

Figure 20 shows a neutral gas (Argon Ag) that is ionized for an electric field; the magnetic field lines start from the outer north poles and end at the centrally arranged south pole. In addition to the magnetic field lines, an electric field **E**, perpendicular to the target surface, is created by applying a negative potential $-U_T$ at the target. The magnetic field lines parallel to the target surface and perpendicular to the electric field **E** are denoted by **B$_p$.** The magnetic field attracts the free electrons directly above the target surface; the electrons trapped in the magnetic field have more probability of ionizing a neutral gas molecule by several orders of magnitude [33]. This increase in available ions significantly

---

[32] [20] M. Braun, "Magnetron Sputtering Technique," in *Handbook of Manufacturing Engineering and Technology*, Sweden, 2015, pp. 2929-2957.

increases the rate at which target material is eroded and subsequently deposited onto the substrate[34].

The deposition System-AJA Magnetron Sputtering is used in this work; it has 5-3" magnetron sputtering sources and turbo-pumped vacuum load-lock with six position cassette. The flow of gases and temperature deposition is controlled by a computer connected to the sputtering. The material that is a possible deposit in the AJA Magnetron of nanoscience UCF is VO2. *Figure 21*.
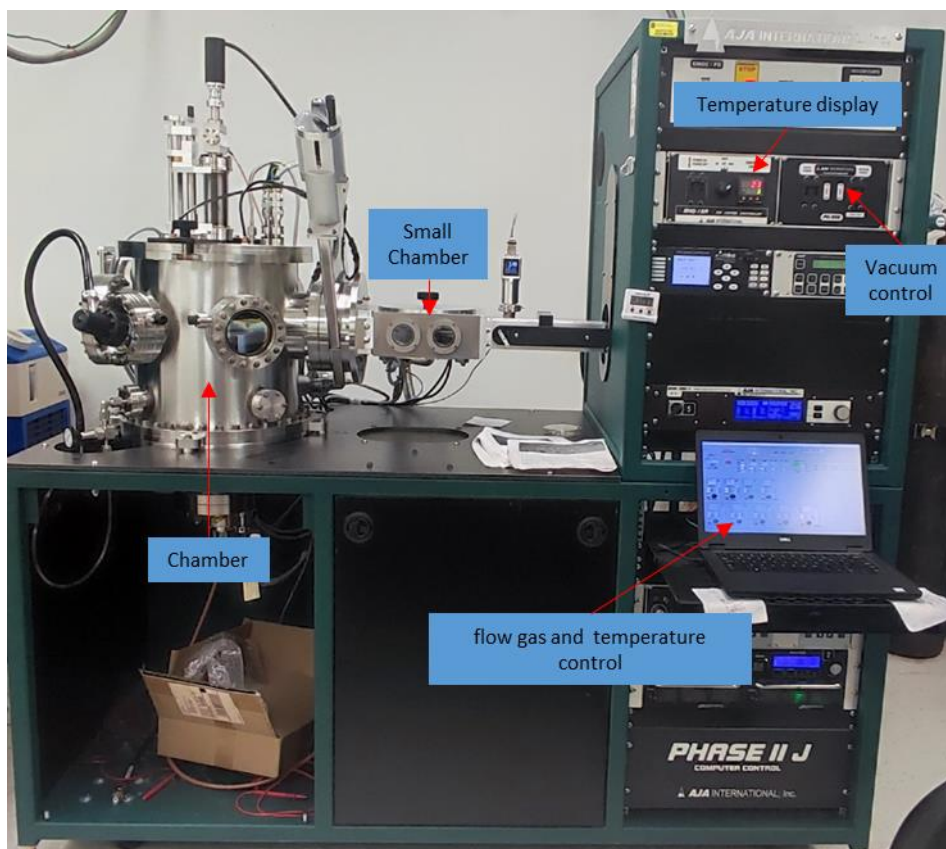
Figure 21 System-AJA Magnetron Sputtering

---

[34] A. I. Inc, "https://www.ajaint.com/what-is-sputtering.html," [Online].

CHAPTER 4

COLOR STRUCTURAL

Nanotexturing of materials introduces innovative methods for manipulating the interaction between light and matter, in contrast to bulk materials, a material´s characteristics at the nanoscale exhibit a pronounced an its size and shape. When electromagnetic wave interacts with a metallic nanoparticle, they induce a collective oscillation of the free electrons in the conduction band, referred to as localized plasmons, resulting in intense optical absorption[35] [36]. Notably, this resonant response is highly contingent on the composition, size, spatial arrangement, and environmental factors affecting the structure[37] [38]. In a sense, nanoparticles function as optical antennas, capturing and confining light at volumes much smaller than the wavelength, leading to an

---

[35] [24] S. A. Maier, Plasmonics: Fundamentals and Applications, United Kingdom: Springer, 2007.

[36] H.-S. K. a. K. B. Ralf B. Wehrspohn, Nanophotonic Materials: Photonic Crystals, Plasmonics, and Metamaterials, WILEY-VCH, 2008.

[37] [35]

[38] B. D. a. L. N. Palash Bharadwaj, "Optical Antennas," *Advances in Optics and Photonics,* vol. 1, no. 3, pp. 438-483, 2009.

exceptional enhancement of the near field[39]. This plasmonic resonance can be harnessed to regulate materials´ spectral and spatial reactions to incident light, paving the way for exiting applications in holography, wavefront engineering, display technologies, sensing, and structural coloration[40] [41] [42] [43] [44]. Creating artificial colors by exploiting plasmonic resonances has garnered significant attention in recent years[45] [46] [47] [48]. In plasmonic coloration, the color arises from the absorption of specific bands of incoming light by the constituent metallic nanoparticles.

In this Chapter, the results of two projects are reported; the first is the fabrication of a nanostructure that produces plasmonic color, where we show

[39] Jon A Schuller, Edward S Barnard, Wenshan Cai, Young Chul Jun, Justin S White, Mark L Brongersma, "Plasmonics for extreme light concentration and manipulation," *Nature Materials,* vol. 9, no. 3, pp. 193-204, 2010.

[40] Matthew E. Stewart, Christopher R. Anderton, Lucas B. Thompson, Joana Maria, Stephen K. Gray, John A. Rogers, and Ralph G. Nuzzo, "Nanostructured Plasmonic Sensors," *Chem. Rev.,* vol. 108, no. 2, pp. 494-521, 2008.

[41] Ni, X., Emani, N. K., Kildishev, A. V., Boltasseva, A., & Shalaev, V. M., "Broadband light bending with plasmonic nanoantennas," Science, vol. 335, no. 6067, p. 427, 2012.

[42] Ming Kang, Tianhua Feng, Hui-Tian Wang, and Jensen Li, "Wave front engineering from an array of thin aperture antennas," Optics Express, vol. 20, no. 14, pp. 15882-15890, 2012.

[43] Daniel Franklin, Yuan Chen, Abraham Vazquez-Guardado, Sushrut Modak, Javaneh Boroumand, Daming Xu, Shin-Tson Wu & Debashis Chanda, "Polarization-independent actively tunable colour generation on imprinted plasmonic surfaces," Nature Communications, vol. 6, no. 1, p. 7337, 2015.

[44] J. Scheuer, "Metasurfaces-based holography and beam shaping: engineering the phase profile of light," Nanophotonics, vol. 6, no. 1, pp. 137-152, 2017.

[45] A. N.Dushkina, In Engineered Biomimicry, Elsevier, 2013, pp. 267-303.

[46] S. Daqiqeh Rezaei, Z. Dong, J. You En Chan, J. Trisno, R. J. H. Ng, Q. Ruan, C. W. Qiu, N. A. Mortensen, J. K. W. Yang, "Nanophotonic Structural Colors," *ACS Photonics,* vol. 8, no. 18, 2020.

[47] Z. Xuan, J. Li, Q. Liu, F. Yi, S. Wang, W. Lu, "Artificial Structural Colors and Applications," The Innovation, vol. 2, no. 100081, 2021.

[48] Yulan Fu, Cary A. Tippets, Eugenii U. Donev and Rene Lopez, "Structural colors: from natural to artificial systems," WIREs Nanomed Nanobiotechnol, vol. 8, no. 758, 2016.

significantly that the absorption bands can be easily adjusted by altering the geometric parameters of the structure, resulting in color modification. The second project shows that if a plasmonic structure encounters an external stimulus that alters its material properties, geometry, or the surrounding environmental conditions, it will change its color appearance. In simpler terms, nanostructures can translate alterations in their structure or environment into corresponding changes in their optical response and present a versatile platform for sensing applications.

4.1. Self-assembled Plasmonic paint (Dielectric thin-film and nanoparticles Al)

This section presents a self-assembled subwavelength plasmonic cavity; this structure offers angle and polarization-independent vivid structure colors, getting a surface colorimetric. The structure is fabrication through E-Beam evaporation and Atomic Layer Deposition (ALD) techniques. These techniques are explained above in the methods section.

4.1.1. Experimental Methodology

The surface colorimetric is fabrication on a standard microscope slide; this is cut in pieces of sizes 25mm X 25 mm, and the clean slide (substrate) process is

- Immersion in DI water and ultrasonic bath for 15 minutes.
- Dried with Nitrogen.
- Immersion in Acetone and ultrasonic bath for 30 minutes and after ultrasonic bath with Isopropyl Alcohol (IPA) for 30 minutes more.
- Dried with Nitrogen.

4.1.1.1. Self-assembled cavity

The subwavelength plasmonic cavity has three layers: Aluminum (Al), Aluminum Oxide (Al_2O_3), and Nanoparticles (NP) (*Figure 22*). The first layer is

deposited on the glass slide (standard microscope pieces); the Aluminum layer is an optically thick back mirror that has 100 nm of thickness and is produced on a Thermionic E-beam Evaporator. The parameters used for deposit of Al are pressure of $\sim 1 \times 10^{-6}$ Torr and evaporation rate Kept at 0.1 A/s this parameter we have a good quality of mirror. The second layer is the spacer of Al_2O_3 and was grown by atomic layer deposition (ALD, Savannah 200, Cambridge Nanotech) with pulses of trimetylaluminum and water at 100°C. The last layer is the growth of aluminum Islands (nanoparticles) by UHV AJA electron beam evaporator, where the growing methods were previously studied. We find three parameters that play an essential role in the shape and sizes of the monolayer islands film. These are the temperature of the substrate, the pressure in the chamber, and the rate of growth. The sizes of film islands are controlled by rate growth and monitory by the deposit thickness; this parameter is significant for the analysis of the plasmonic color we will discuss later. We chose to keep the temperature of the substrates at 100°C, resulting in high color saturation while being below many polymers, essential for flexible substrate application and lift-off during flakes preparation. For our reproducibility and color vividness, the nanoparticles´ growth was carried on at pressures below 5×10^{-8} Torr, while growth rates were kept constant at about 0.1 A/s. It has been made in this same process with other metals to produce an even larger color gamut and emphasizes the practicality of the approach. However, we report only the ones produced using aluminum and its oxide in this work because we find that it is the optimal solution to fabrication and cost.
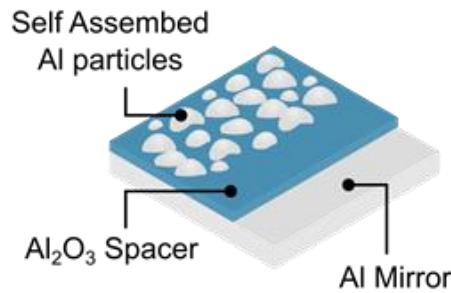
Figure 22 Schema of Structure Absorption for Color Generation. A subwavelength plasmonic cavity formed by a self-assembly of metallic nanoislands on top of an oxide-coated mirror, generates color by selectively absorbing certain wavelengths and strongly back-reflecting other.

4.1.2.   Finite Difference Time Domain Modeling

This section describes the simulations and analytical models used to analyze the structure's self-assembled layer in different situations.

4.1.2.1.   Single particle with periodic conditions

Whit, the collaboration of Dr. Pablo Cencillo, the weight semi-analytical model was built. We calculated the simulated samples' reflection spectral and electric field distribution using the experimental geometrical parameters extracted from the SEM (Scanning Electron Microscope, Zeiss NVision40). The commercial FDTD software package (Lumerical FDTD, Lumerical Solution Inc.) was used for simulation, and the relative permittivities of aluminum and aluminum oxide that were used are taken from the literature[49]. To build the weight semi-analytical model showing in the *Figure 23*, we simulated a single particle with periodic conditions. The values of the unit cell size were chosen to make the area covered by the aluminum island equivalent to those obtained from the SEM analysis for the different samples (55%, 60% and 70% for the 4, 8 and 12 nm respectively). 50 simulations with radii values within 4 standard of the mean value were then performed and weight-averaged reflectance calculated as:

---

[49] Palik, Edward D., Handbook of Optical Constants of Solids, vol. 3.

$$\bar{R} = \sum_i R_i \times w_i \qquad (4.1)$$

where w_i and R_i represent the Gaussian weight and simulated reflection for the particle i.
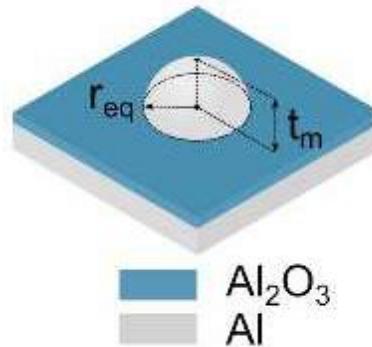
Figure 23 A single particle with periodic conditions

4.1.2.2. Relative position of the plasmonic particles, analysis of effect of disorder.

In addition to the size and shape of islands, the resonances of the self-assembled layer depend on the relative position of the plasmonic particles. As observed in the SEM micrographs, the nanoislands fill most space generation an isotropic monolayer of highly-packed hemispheroids of different sizes in no particular order or orientation. To evaluate the effect of this spatial disorder on the effective optical response of the self-assembly and disentangle it from the effect, we simulated an array of 49 particles. This array was built with the FDTD Lumerical software with experimental structure characteristics but with different configurations in the array of particles. We run simulations for 7x7 nanoislands in three different configurations, introducing the disorder parameter following the

method by Zhang et al [50]., a periodic square array of particles of equal sizes, a disordered array of particles of equal sizes, and a disordered array of particles of random sizes as predicted by the Gaussian fit of histograms. The set of simulations for 7X7 hemispherical nanoparticles is for an equivalent thickness mass of 4 nm on top of a 10 nm oxide spacer. This configuration is shown in *Figure 24*.
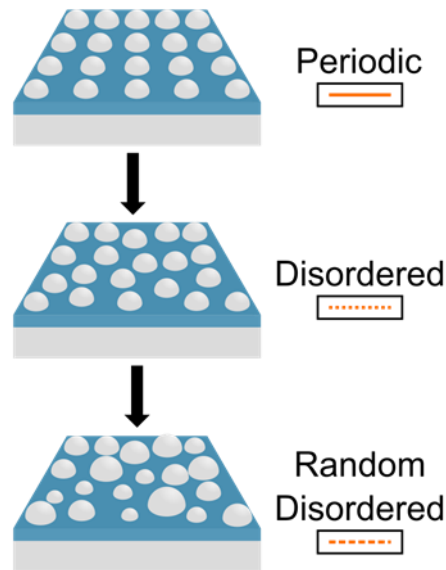
Figure 24 7x7 hemispherical particles with equal size in periodic and disorder arrangement, and random size and disordered arrangement, equivalent to the 5 nm self-assembly layer with 10 nm aluminum oxide spacer

4.1.2.3.   Simulation study of the Cavity Stack

Finite-difference time-domain (FDTD) simulations were performed using a commercial software package (Lumerical FDTD Solutions) to analyze the cavity stack. We combined the spatial disorder and particle size distribution in run simulations on 1028, 412, and 218 nanoislands corresponding to 5,8 and 12 nm

[50] Mao P, Liu C, Song F, Han M, Maier SA, Zhang S., "Manipulating disordered plasmonic systems by external cavity with transition from broadband absorption to reconfigurable reflection," *Nature Communications*, vol. 11, no. 1538, p. 1, 2020 Mar 24.

mass thicknesses. Analyzing the fabricated samples with the SEM estimated the covered area to be 55%, 65%, and 75% for the yellow, magenta, and cyan samples, respectively. In the simulation, the algorithm used for filling the simulation boxes with non-overlapping hemispheres could only fill 45 to 50% of the area before becoming prohibitively time-consuming. The illumination source is normal incident plane waves, and the reflection spectra were calculated by recording the field with monitors, as shown in the *Figure 25* 3D.
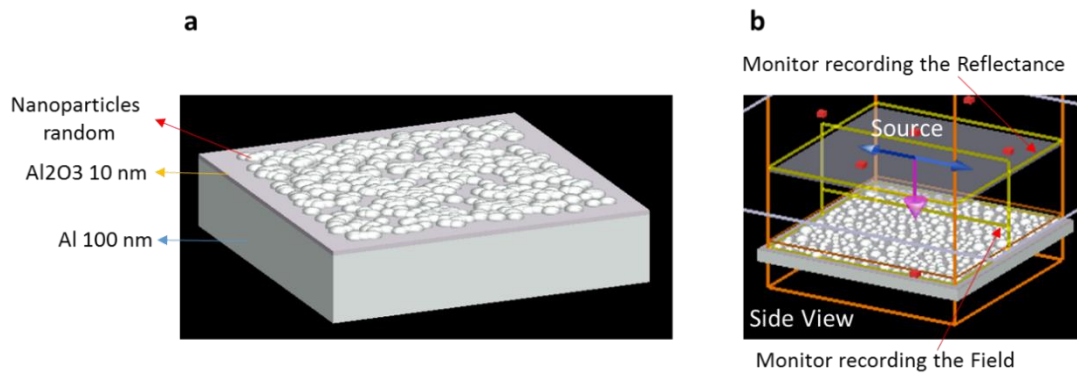
Figure 25 Simulation setup used for FDTD simulations shows nanoparticles randomly non-overlapping (Figure 25 a) based on the SEM results shown in Figure 28. View in 3D where show normal source, the monitors that record the Flied in the nanoparticles and reflectance (Figure 25 b). The box size is 1 um x 1 um.

4.1.3. Color Gamut Evaluations

The color gamut graphic is made in collaboration with Dr. Pablo Cencillo. To find the L*a*b* coordinates of the fabricated samples we first obtained the XYZ tristimulus values integrating over the visible spectrum according to:

$$X = \frac{1}{N} \int \bar{x}(\lambda) R(\lambda) I(\lambda) d\lambda$$

$$Y = \frac{1}{N} \int \bar{y}(\lambda) R(\lambda) I(\lambda) d\lambda \qquad (4.\ 2)$$

$$Z = \frac{1}{N} \int \bar{z}(\lambda) R(\lambda) I(\lambda) d\lambda$$

$$N = \int \bar{y}(\lambda) I(\lambda) dy$$

where $R(\lambda)$ is the measured reflectance; $\bar{x}(\lambda), \bar{y}(\lambda)$, and $\bar{z}(\lambda)$ are the color matching functions that describe in numerical form the chromatic response of the observation; $I(\lambda)$ is the reference Illuminant; λ is the wavelength of the monochromatic light measured in nanometers. From the tristimulus values CIEXYZ the CIELAB coordinates can be calculated from:

$$L^* = 116 f_y - 16$$

$$a^* = 500(f_x - f_y)$$ (4. 3)

$$b^* = 500(f_y - f_z)$$

where, being $t_x = \frac{X}{X_n}, t_y = \frac{Y}{Y_n}, or\ t_z = \frac{Z}{Z_n}$; and $X_n = 0.9642$, $Y_n = 1.0000$, and $Z_n = 0.8251$ is the point coordinate that describes of the achromatic illuminate reference white D50 using in the printing industry and the graphic arts for color proofing as per ISO 3664:2009:

$$f_i = \begin{cases} \sqrt[3]{t_i}, & if\ t > \left(\frac{6}{29}\right)^3 \\ \dfrac{841\ t_i}{108} + \dfrac{4}{29}, & otherwise \end{cases}$$ (4. 4)

As the reference illuminate, we chose D50. Finally, to keep consistency, all colormaps presented in the figures in the section Results correspond to a horizontal slice with $L^* = 75$.

4.1.4. Measurements and Images

Reflection measurements were taken at normal incidence with unpolarized light using a 4X, 0.07 numerical aperture objective and fiber coupled spectrometer (HR 2000+, Ocean Optics. The scheme is shown in the *Figure 26*. An aluminum mirror was used as a reference. The spectrometer is a system that measures light's properties and allows light decomposition into its different lengths of waves. It consists of mirrors collimating and focusing the light in a

grating, the light is diffracted, and the detector collects the light from the focusing mirror and converts the optical signal to a digital signal.

Angular measurement was taken with an integrating sphere (RTC-060-SF, Labsphere) connected to the spectrometer. The integrating sphere is an optical component consisting of a hollow spherical cavity with its interior covered with a diffuse white reflective coating, with small holes for entrance and exit ports. The light scattered by the interior of the integrating sphere is evenly distributed over all angles, illuminating the sample and then detecting it. To ensure consistency on illumination the sample was photographed with flash-light at fixed intensity. Photographies for the butterfly models were taken under sun illumination with a linear polarizer attached to the objective.
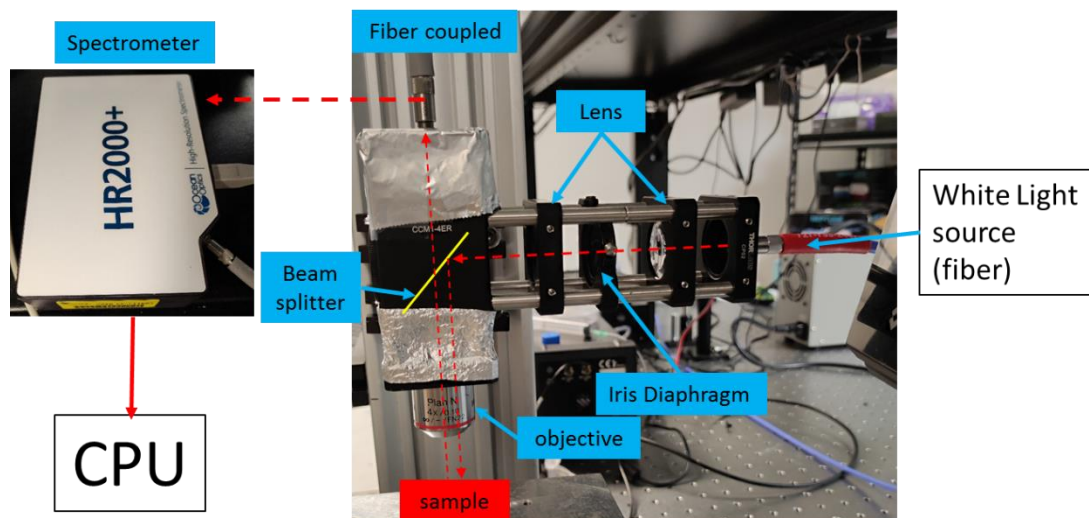
Figure 26 Schematic for measuring Reflectance

4.1.5.   Results and Discussion

Dielectric thin film and nanoparticles. In nature, our colors are origin chemical and structural coloration. For example, the pink tint of Formosa azaleas, *Figure 27* a, is due to the absorption of cyaniding molecules, a type of

anthocyanin pigment that gives reddish colors[51]. In contrast, the bright metallic blue displayed by the Peruvian Morpho didius, *Figure 27* b, primarily results from how the blue components are scattered by lamellae nanostructures in this butterfly´s wings[52]. Frequently, however, structural color in animals results from the combination of the diffraction and scattering of the outer skin layer and the molecular absorption of the complementary color by intrinsic pigments of the skin[53]. This critical observation inspired us to produce an absorptive structural pigment where the selective absorption of specific frequencies results from the tailored structural resonant response of metallic nanostructures coupled to a subwavelength optical cavity. The proposed architecture consists of a highly-packed monolayer of self-assembled aluminum nanoislands on this aluminum oxide film that spaces them from the aluminum back mirror, *Figure 27* c. In this configuration, the aluminum nanoislands resonantly absorb specific wavelengths, while the back mirror strongly back-reflects the non-resonant ones, rendering vivid colors based on colorless materials.

---

[51] Daiki Mizutaa, Takuya Banb, Ikuo Miyajimac, Akira Nakatsukab, Nobuo Kobayashi, "Comparison of flower color with anthocyanin composition patterns inevergreen azalea," *Scientia Horticulturae* , no. 122, pp. 594-602, 2009.

[52] Kinoshita, S., Yoshioka, S., & Kawagoe, K., "Mechanisms of structural colour in the Morpho butterfly: cooperation of regularity and irregularity in an iridescent scale," *Proceedings. Biological sciences,* vol. 269, no. 1499, p. 1417–1421, 2002.

[53] Y. S. Kinoshita S, "Structural colors in nature: the role of regularity and irregularity in the structure," *Chemphyschem.,* vol. 6, no. 8, pp. 1442-1459, 2005.
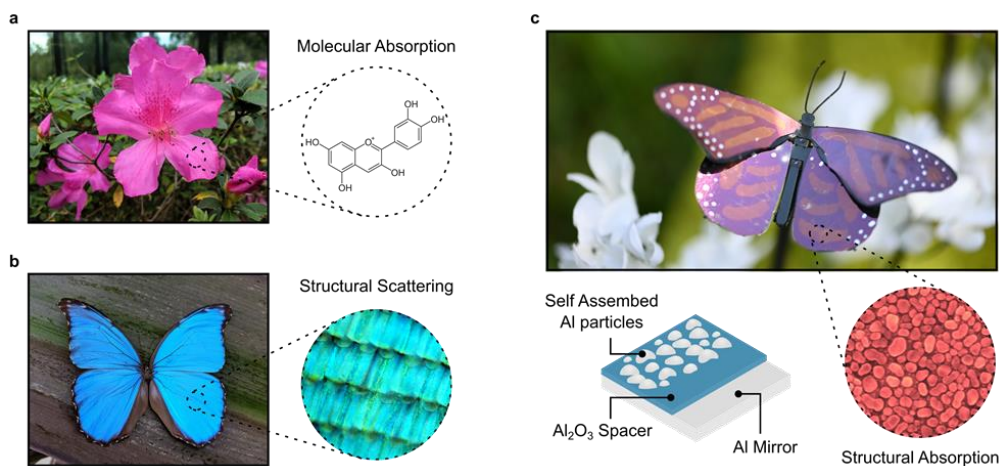
Figure 27 Structure Absorption for Color Generation. a), Many Chemical substrates produce color by selectively absorbing frequencies matching their molecular electronic transitions. Pink color in Formosa azaleas is due to the absorption of cyaniding molecules. b), An example of structural coloration is found in the Peruvian Morpho didius. Lamellae nanostructures found in its wings scatter the blue components of incident light generating its characteristic metallic blue. c), A subwavelength plasmonic cavity formed by a self-assembly of metallic nanoislands on top of an oxide-coated mirror, generates color by selectively absorbing certain wavelengths and strongly back-reflecting other.

Contrary to other artificial structural schemes that rely on the use of low-throughput, multistep, top-down techniques such as electron beam lithography or focused ion beam, incompatible with mass production, the proposed architecture is the result of a naturally occurring nucleation process in an electron beam evaporator. In the self-assembly growth, small clusters of aluminum nanoparticles are formed due to the more significant affinity of the aluminum atoms to their kind over the oxide substrate. With a low enough rate, the evaporation of nanometric films results in a nanoparticles monolayer that exhibits optical plasmonic resonances. Crucially, this pressure- and temperature-controlled process ensures high reproducibility over broad areas in a simple step, lowering the cost of production and enabling large-scale fabrication. The dynamics of the self-assembly process are presented in detail in a single step, lowering the cost of production and enabling large-scale fabrication.

The method developed in the fabrication of the nanoparticles monolayer was Volmer-Weber and is described in the section of methods where the formation of nuclei and their evolution is a process governed by the surface

energies at the interfaces between the substrate and the film to grow. The evaporation of aluminum on alumina exhibits the Volmer-Weber mode where adjusting the equivalent thickness mass, i.e., the amount of aluminum evaporated; one can control the size of the particles and, consequently, the color appearance of the sample. The results of this cumulative process for three mass equivalent thicknesses can be seen in the *Figure 28*. The samples correspond to yellow, magenta, and cyan, with 5,8 and 12 nm thicknesses, respectively; these pigments' primaries are used in the CMYK color model typical of printing devices. The high color homogeneity is achieved on squares in area sizes of inches and using the small abeam chamber; the result is seen in *Figure 28*c. The evaporation system employed is described in the section Methods, and the process is in the section experimental methodology. The samples were characterized using scanning electron microscopy, as shown in the micrograph insets *Figure 28*a, where we see that the aluminum grows, producing randomly placed nanoislands with sizes and shapes that vary with the thickness mass. Using the micrographs obtained from the SEM and the Fiji[54] processing package, quantitative analysis was done to obtain a histogram distribution of the equivalent radii to the hundreds of nanoislands per sample. For a given nanoisland, its equivalent radius is defined as the radius of a circular particle that would cover the same area as the one measured. The morphological homogeneity of the samples made characterized use of the histograms fit with a normal distribution from which a mean equivalent radius and a standard deviation are extracted, in agreement with the literature[55] where we observe a linear relationship between the thickness mass and the mean equivalent radius of the islands we can been in the *Figure 28*b.

---

[54] Johannes Schindelin, et al. "Fiji: an open-source platform for biological-image analysis," *Nature Methods,* vol. 9, p. 676–682, 2012.

[55] Granqvist, Thorwald Andersson and C. G., "Morphology and size distributions of islands in discontinuous films," *Journal of Applied Physics,* vol. 48, no. 4, pp. 1673-1679, 1977.
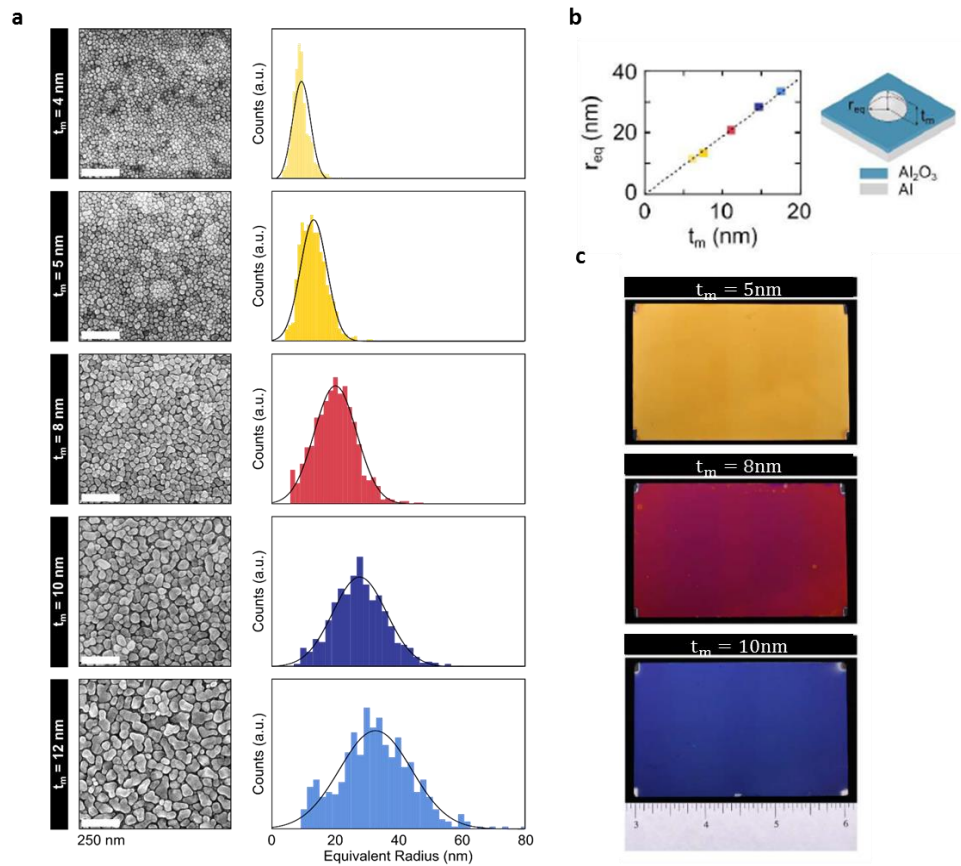
Figure 28 **Morphology dynamics of the self-assembly**. a, The SEM analysis of samples corresponding to thicknesses from 4 to 12 nm show how size and shape of the nanoparticles changes with increasing thickness. The histogram analysis of the SEM micrographs show together with the size increase, larger size and shape variability is induced in the system. Black curves correspond to a Gaussian fit of the histogram distribution. b, Linear proportionality between the equivalent thickness mass and Gaussian mean values as obtained from the SEM images. c, The fabrication method allows the production of large scale fabrication of nanostructured surfaces with great homogeneity.

Optical Response of the Near-Field Coupled Gap Plasmons. The color of the nanostructure is the result of the absorptive response of the self-assembled aluminum monolayer and the subwavelength cavity formed by nanoparticles as the top layer, the aluminum back mirror, and the dielectric spacer sandwiched in between. If there are any geometrical changes in any layers, the perceived color will change accordingly. When ambient light reaches the monolayer, the electric field of the light at select wavelengths can drive the free electrons of the aluminum to oscillate resonantly within the nanoparticles' geometry. This collective oscillation, known as localized surface plasmon resonance, is influenced by the coupling between closely-packed neighboring particles and the presence of the back-mirror inference at a subwavelength

62

distance from the particles'layer. The hybridization mechanism results in a gap-plasmon mode that causes strong optical absorption and tight confinement of the light at the metal/dielectric boundary of the metallic particles at resonant frequencies. The perceived color is determined by the spectral position of the absorption band, which is influenced by the gap-plasmon dispersion. The gap-plasmon dispersion is controlled by three parameters: (1) the size and spatial distribution of the nanoislands, (2) the refractive index of their environment, and (3) the thickness of the spacing layer.

The control of nanoisland size can be achieved by adjusting the amount of evaporated aluminum. To explore the spectrum of colors obtainable through this process, we employed a shutter to regulate the sample´s partial exposure during evaporation. In this manner, by rotating the sample, we generated a polar thickness gradient ranging from 0.5 nm to 16 nm, with thickness increments of 0.5 nm corresponding to wedges of approximately 11° (see *Figure 29*b). As the thickness mass increases, neighboring nanoislands merge to form large particles (see *Figure 29*a-top).

The increase in the nanoislands´ size leads to a red-shifts the absorption band, resulting in a diverse range of hues and saturations. This produce a color palette that covers from the white of the black mirror, at very low thicknesses, to the yellow, magenta, and blue. It should be noted that, being a subtractive color scheme, a red-shift of the absorption band results in a blue-shift in perceived color. This phenomenon occurs as the intensity of blue components in the reflected light increases, reducing the proportion of the yellow and red components. If the process is carried on for long enough, adjacent nuclei can coalesce to form semi-continuous films and, eventually, continuous films, as illustrated in *Figure 29*a-bottom. The point at which the transition occurs from isolated islands to a continuous film is known as the percolation threshold. When the aluminum thickness exceeds this threshold, the metal's free electrons can find paths to move through the self-assembly, eliminating the geometrical confinement required for resonant plasmonic absorption and disabling color

production. This can be observed in the gradient wheel sample at higher thicknesses, where the blue color fades to white, as shown in *Figure 29* b.
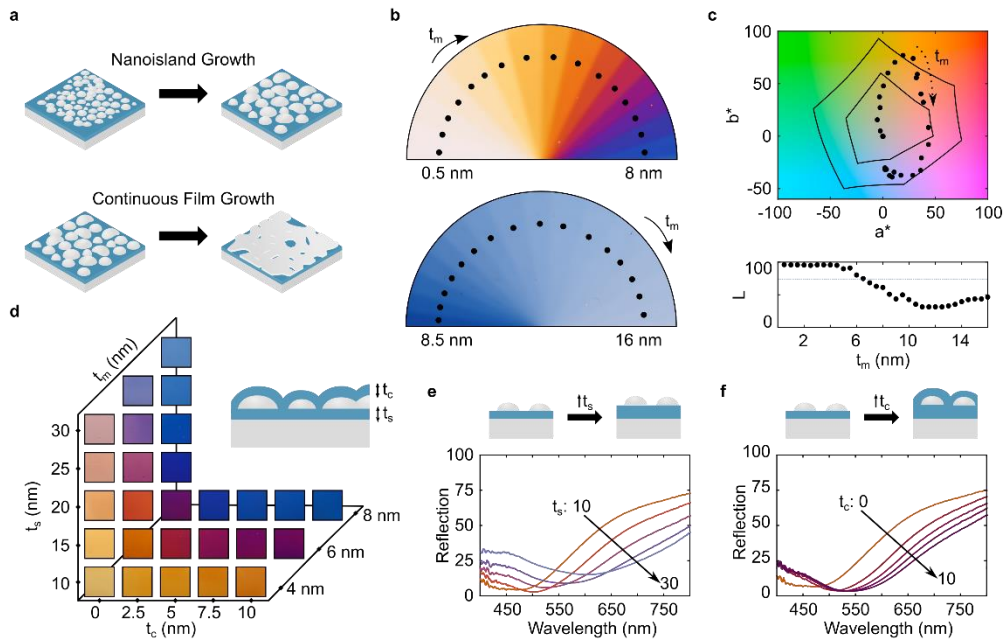
Figure 29 Color Space and Quality of the Plasmonic Cavity: a) In the Volmer-Weber growth mode, the size of the nanoislands can be controlled by adjusting the amount of evaporated aluminum (top). If the process continues for an extended duration, semi-continuous films form, deactivating the plasmonic resonances and, consequently, the color (bottom). b) Depicts the color polar gradient for thicknesses ranging from 0.5 to 16 nm, with a fixed 10 nm spacer. c) Compares CIELAB coordinates for the points in the color wheel to ISO DIS 15339-2 cold-set newsprint and coated premium paper standards (inner and outer hexagons). d) Illustrates how tuning the spacer and capping layer thicknesses expands the available color space. e, f) Demonstrate the red-shift of the absorption resonance as the spacer and capping layer thicknesses are increased.

In addition to the spectral shift, the increase in the thickness mass leads to a broadening of the optical resonances. We attribute this phenomenon to the inhomogeneous broadening of the nanoparticles' resonances, which arises from the doubly random nature of both the morphology and spatial distribution, as illustrated in *Figure 30*. On the other hand, an increase in thickness mass leads to significant variability in the island size, as shown in *Figure 28*a. To investigate this effect further, we constructed a semi-analytical model that determines the monolayer's total reflection by weight averaging the reflection of periodic islands of 50 hemispherical radii, which are within four deviations of the mean value obtained from the SEM analysis for an 8 nm thickness mass as shown in *Figure*

*30*a. The significant variation in morphology leads to resonance broadening, to the reduction in the reflection contrast and saturation of the resulting colors, as illustrated in *Figure 30*b. Generally, reflective color generation is less pure than transmissive due to the narrow spectral resonances. Besides, the effect of spatial distribution can be explained through the dependency on the relative position of interacting plasmonic resonators. To assess this effect, we conducted a series of simulations for 7x7 hemispherical nanoparticles with an equivalent thickness mass of 4 nm on top of a 10 nm oxide spacer where the configurations are arranged in a periodic square array, a disordered array of particles of equal sizes, and a random array of varied sizes as predicted by the Gaussian fit of the histograms, as presented in *Figure 30*c. The reflection curves indicate a spectral shift that we attribute to the different energies of the newly available modes arising from the lateral hybridization of nanoparticles, which are otherwise forbidden in the symmetry arrangement.

*Figure 30*c displays the reflection curves for the three configurations studied. It can be observed that the reflection contrast decreases as spatial disorder is introduced, resulting a broader absorption resonance. We propose that this broadening is due to the displacement of the resonant shift from the excitation of laterally hybridized modes of closely spaced particles. Such modes were previously prohibited due to symmetry reasons in the case of the periodic arrangement of particles[56].

*Figure 30*d shows the electric field enhancement at three spectral positions for a simulation corresponding to the yellow sample of *Figure 28* c; the spectral positions are in-resonance (425 nm), at the tail of the resonance (505 nm), and off-resonance (705 nm). The horizontal cross-section is taken at 3 nm above the nanoislands/oxide interface. We show that for the ordered structure, the dipolar resonance is only excited at the in-resonance wavelength, while it is significantly

---

[56] Sheikholeslami, S.,Jua,Y., Jain,.P. K.& Alivisatos, A. P., "Coupling of Optical Resonances in a Compositionally Asymmetric Plasmonic Nanoparticle Dimer," *Nano Lett.,* Vols. 2655-2660, p. 10, 2010.

suppressed at the tail and off-resonance. However, both disordered and randomly disordered configurations exhibit strong excitation of plasmonic modes, even outside the in-resonance spectral position. It is worth noting that the modes excited in-resonance and off-resonance for these two disordered configurations correspond to different particles than the ones excited in-resonance, confirming the inhomogeneous broadening nature of the effect. Furthermore, the vertical distribution of electric fields for all three configurations in resonance is extracted. Unlike other plasmonic structures that rely on vertical metal/insulator/metal cavities, in the self-assembled plasmonic structure, most of the energy is confined to the interstices between the nanoislands. This allows for color production even for thick oxide layers and the resonant modes are strongly influenced by the refractive index of the surrounding medium.
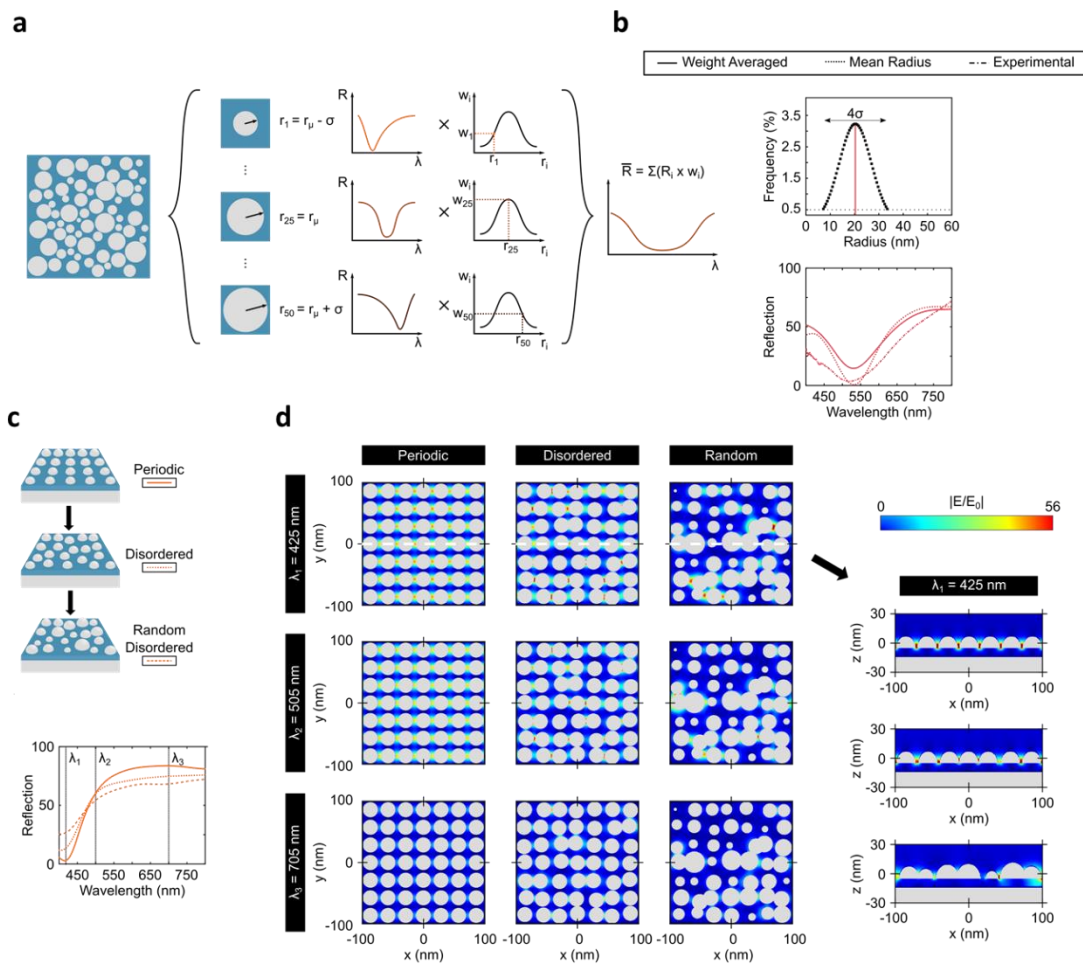
Figure 30 Size distribution effect on the optical response. a, To simulate the inhomogeneous broadening of the resonance as a result of the broader distribution of particles, we average the reflection

curves obtained from FDTD simulations of 50 radii within 4 standard deviations of the mean value, as obtained from the Gaussian fitting of the SEM histograms, assuming square periodic boundary conditions. b, The reflection curves for the experimental, weight-averaged, and FDTD simulation are compared for the case 8 nm. Disorder effect on the optical response. c, Reflection curves for FDTD simulations corresponding to 7x7 hemispherical particles with equal size in periodic and disorder arrangement, and random size and disordered arrangement, equivalent to the 5 nm self-assembly layer with 10 nm aluminum oxide spacer. d, Electric profiles in three different spectral positions for the configurations of panel c.

The observed inhomogeneous broadening can be effectively explained using the classical formula for dipole-dipole interaction energy, as described by [57]:

$$W = k_e k_\propto \frac{|\boldsymbol{p}_1||\boldsymbol{p}_2|}{n_e^2 |\boldsymbol{r}_{12}|^3} \qquad (4.\,5)$$

In this equation, k_e represents the Coulomb constant, $k_\propto$ denotes the orientation factor, n_e corresponds to the refractive index of the surrounding medium, $|\boldsymbol{p}_1|$ and $|\boldsymbol{p}_2|$ represents the modulus of the dipole moments for two interacting particles, and $|\boldsymbol{r}_{12}|$ represents the magnitude of the distance between them. The near-field approximation considers the interaction between two neighbor particles. The modulus of the distance between the particles is significant in their interaction energy. As the particles become closely packed, the distance between them decreases, increasing interaction energy. Consequently, this causes a blue-shift in the resonating wavelength.

Theoretical, Semi-Analytical, and Simulation study of the Cavity Stack. When the sizes and shapes of the particles exhibit significant variability, it is expected that the dipole modes corresponding to a particular illuminating wavelength will be weakly exited. As a result, lower absorption and a reduced reflection contrast are anticipated. Moreover, the broadening of the spatial disorder can be attributed to the averaging of distances between particles. Some particles will undergo constructive interference, while other will experience

---

[57] Bron, M.& Wolf, E., Principles of Optics., Cambridge University Press, 1999.

destructive interference. Lastly, it is worth noting that our subtractive color scheme requires broad resonances to achieve more saturated colors, unlike colors produced by luminous objects which necessitate high purity. The high-density packing of the self-assembled structure plays a crucial role in bringing the hybridized modes into the visible range and ensuring vivid coloration within a single nanometric layer. However, this dense packing also intensifies the broadening of resonances caused by the dynamic depolarization of non-spherical particles, this phenomenon is showing in the simulation study of the cavity stack *Figure 31*. To compare the reflection curves considering both spatial disorder and size distribution of particles, we conducted simulations on different numbers of nanoislands. Specifically, we performed simulations on 1028, 412, and 218 nanoislands, corresponding to mass thicknesses of 4 nm, 8nm, and 12 nm, respectively. The experimental, analytical model and simulated reflection curves for all three samples can be observed in *Figure 31*a. While the simulated reflection curve qualitatively reproduces the measured ones, they exhibit a noticeable spectral blue-shift that becomes more prominent with increasing nanoisland size. We attribute this blue-shift to the growing disparities in the filling factor between the simulated samples and the fabricated ones. The SEM analysis estimated the covered area to be 55% for the yellow sample, 65% for the magenta sample, and 75% for the cyan sample. However, the algorithm that filled the simulation boxes with non-overlapping hemispheres could only achieve a filling factor of 45% to 50% before it became excessively time-consuming. *Figure 31*b displays cross-sections of the electric fields at a distance of 5 nm above the interface for two specific wavelengths. These cross-sections illustrate the excitation of the laterally hybridized plasmonic modes within the plane of the nanoislands. The presented data highlights the spatial distribution and behavior of the electronic fields at those specific wavelengths, shedding light on the characteristics of the plasmonic modes in the system. By examining the electric field distribution, the behavior and characteristics of these plasmonic modes can be observed and analyzed.
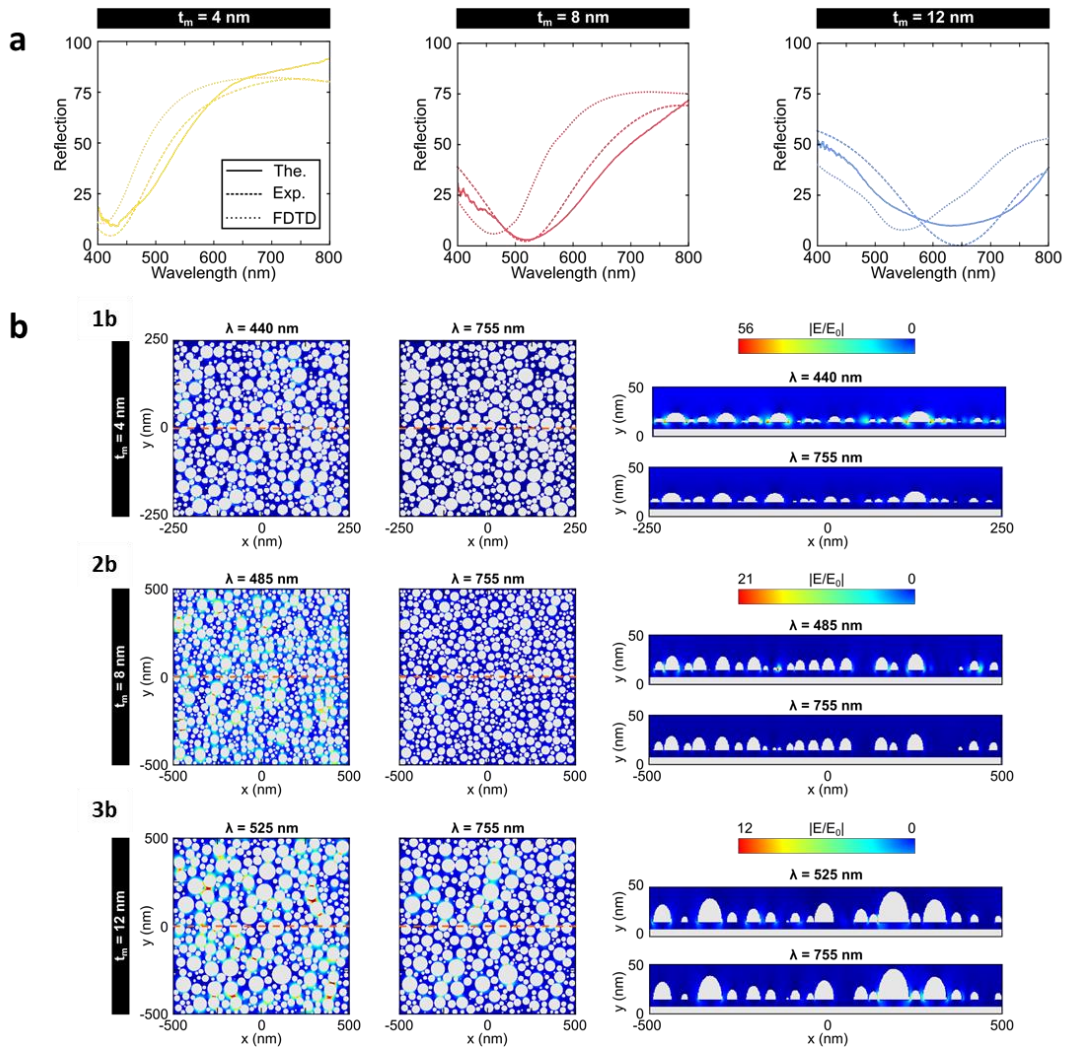
Figure 31a) compare reflection curves for the experimental data, analytical model, and FDTD simulations. The curves correspond to three different sets of nanoislands: 1028, 412, and 218 nanoilands, representing a thickness of 4 nm, 8 nm, and 12 nm. The figure illustrates the agreement of differences between the experimental results, the analytical model, and the FDTD simulations for each nanoisland thickness. b) The field distribution of the electric field is presented for the samples shown in Figure 4a. The field distribution is depicted for both the resonance wavelength and off-resonance wavelength. These plots provide a visual representation of the excitation of the laterally hybrized plasmonic modes within the plane of the nanoilands.

The spectral dependence on the filled can be explained within the hybridization model by considering the dipole-dipole interaction energy between neighboring particles. In this near-field approximation, the interaction energy W can be described using Equation (4. 5).

An analytical model is utilized in this study to address the computational challenges associated with simulating a large number of nanoislands. The model combines an effective medium theory that describes the nanoislands' layer with the transfer-matrix method (TMM), which describes the multilayer stack as a stratified medium (*Figure 32*).

In the analytical model, an effective electrical permittivity is derived based on the structural parameters obtained from SEM morphological analysis. Following the approach introduced by Fedotov and colleagues[58], The expression for the effective medium takes into account the instantaneous interaction of the seven nearest particles. This means that the model takes the background field of farther islands, the charge images of the particles in the interface, and depolarization terms that consider the inhomogeneous broadening of the resonance. These interactions contribute to the overall effective behavior of the self-assembled structure and play a role in determining its optical properties. By considering the interactions with nearby particles, the model captures the effects of the local environment on the system's collective behavior, providing a more accurate description of the effective medium. The effective electrical permittivity of the self-assembly is given by

$$\epsilon_{eff} = \epsilon_{env} \left(q \frac{\epsilon_{NP} - \epsilon_{env}}{\epsilon_{env} + F(\epsilon_{NP} - \epsilon_{env})} + 1 \right) \qquad (4.6)$$

In this equation, ϵ_{env} represents the environmental permittivity, ϵ_{NP} represents the permittivity of the nanoparticles (such as aluminum), and F represents the effective geometrical factor of the particles. The effective geometrical factor considers the local electric field contributions from nearest neighbors, far-field interactions, and image particles on the interface. The formula combines these

[58] Fedotov, V. A., Emel'yanov, V. I., MacDonald, K. F. & Zheludev, N. I., "Optical properties of closely packed nanoparticles films: spheroids and nanoshells," *J. Opt. A Pure Appl. Opt.,* vol. 6, p. 155, 2003.

factors to calculate the effective electrical permittivity of the self-assembled structure.

One the effective electrical permittivity is determined, it is used to calculate the Fresnel coefficients, which are input into the transfer-matrix method (TMM) model calculates the total reflectance of the multilayer stack. The experimental results agree better with this approximated analytical model than the simulations (*Figure 31*). This analytical model provides a convenient way to characterize the other two factor controlling color (i.e. environment and cavity length) and allow for easy expansion to structures with multiple nanoislands. As a result, the analytical model will be used to compare the experimental results.
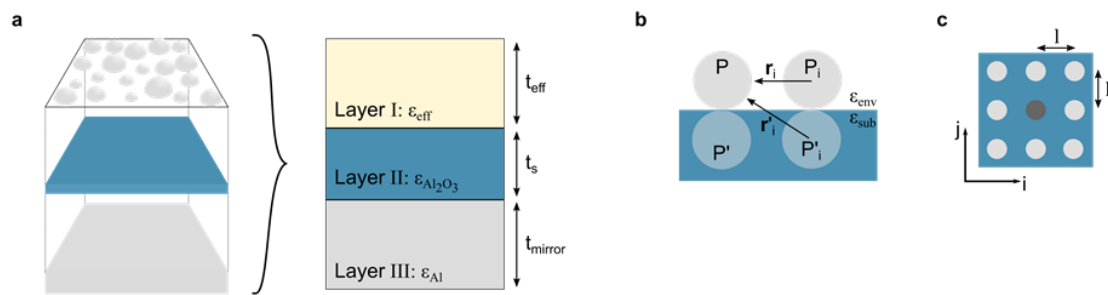
Figure 32 The analytical model employed in this study to alleviate the computational demands associated with simulations involving many nanoislands, the Transfer Matrix Method (TMM), is utilized. The effective medium model considers the interaction of a central particle with its neighboring nanoislands, incorporates the influence of the farther particles, includes the effect of image charges at the interface with the substrate, and incorporates depolarization factors to account for the inhomogeneous broadening of the plasmonic nanoislands.

In this work, we calculated the L*a* b* coordinates based on the reflection spectral of each thickness in the gradient sample to evaluate the color gamut produced by our self-assembled plasmonic structure (see chapter Methods). These L*a*b* coordinates represent the perceived color and were plotted as black dots in the CIELAB color space, as shown in *Figure 29*c. In order to compare the color quality of our plasmonic structure with industry standards, we overlayed the standards for cold-set newsprint and coated premium paper technologies as defined in ISO DIS 15339-2 (represented by the inner and outer hexagons, respectively).

The results indicate that the self-assembled plasmonic colors exceed the color quality standard for newsprint in a substantial portion of the color space and even match the quality of some colors produced on coated premium paper. However, it should be noted that due to the subtractive nature of the plasmonic structure, the production of green color is not possible with a single layer of nanoparticles.

We introduce two color mixing schemes in the subsequent sections to address this limitation and expand the color space. These schemes aim to overcome the restrictions of the single-layer plasmonic structure and enhance the range of achievable colors.

The plasmonic resonance in the metal-dielectric interface are highly sensitive to environmental change, thanks to the strong field confinement[59] [60]. Adding a capping layer on top of the self-assembled structure can further adjust the color response by shifting the resonant spectral position of the nanoislands' layer. Our experiments focused on samples corresponding to mass thicknesses of 4 nm, 6nm, and 8 nm, with a fixed 10 nm-thick oxide spacer. We observed the color change as we grew the alumina capping layer t_c in increments of 2.5 nm, as shown in *Figure 29* d. The reflection curves for the 6 nm samples can be seen in *Figure 29* f. Notably, the capping layer causes a red-shift in the plasmonic resonance, resulting in colors with higher blue components. This behavior can be explained by the classical formula for dipole-dipole energy interaction, was presented before.

This demonstrates that by varying the thickness of the capping layer, we can effectively tune and manipulate the color response of the self-assembled plasmonic structure. Introducing a capping layer provides additional control over

[59] Schmidl, G. et al., "Formation and characterization of silver nanoparticle embedded in optical transparent materials for plasmonic sensor surfaces.," *Mater. Sci. Eng. B,* no. 193, pp. 207-216, 2015.

[60] Mayer, K. M. & Hafner, J. H., "Localized Surface Plasmon Resonance Sensor.," *Chem. Rev.,* no. 111, pp. 3828-3857, 2011

the color properties and opens up opportunities for various applications in color tuning and customization.

As the thickness of the capping layer increases, a more significant portion of the energy becomes confined within the higher dielectric media. This change in the energy distribution weakens the interaction between particles-particles weakens, leading to lower hybridization energies. Consequently, the resonant wavelengths shift towards higher wavelengths.

The effect of top layer in the self-assembled plasmonic structure is particularly important from an applications standpoint. While aluminum itself is chemically stable due to its native oxide layer, we found that the structures can be fragile when exposed to harsh contaminants or physical contact. To address this issue, we applied a commercial polyurethane clear coat (DuraClear Varnish, Americana) as a protective layer.

Interestingly, even with the addition of the clear coat, the samples maintained their vivid colors. This demonstrates that the self-assembled structure´s plasmonic resonance and color response is still preserved despite the protective layer; the result is shown in the next section. Additionally, the clear coat offers enhanced protection against physical contact and increased chemical resistance to spills.

Examining the Limits of the Tunability Through the Spacer and Capping Layer. In examining the tenability limits though the spacer and capping layer, a comparison of experimental and analytical results for all samples can be found in *Figure 33*. Additionally, the L*a*b* coordinates for the new colors produced with the additional capping layer are presented in *Figure 34*. As the capping layer's thickness increases beyond a few 10 nm, the near-field no longer encounters the upper dielectric/air interface, and the contribution from this interface saturates. At this point, the extension of the capping layer should be considered as an additional layer in the transfer matrix method (TMM) analytical model rather than as a change in the refractive index of the environment.

Moreover, it is noted that beyond approximately 20 nm of capping layer thickness, the spectral position of the plasmonic resonance remains unchanged, with only the reflection intensities being affected. This effect is demonstrated in *Figure 35* for samples with 5 nm and 10 nm thickness mass and a 10 nm oxide spacer. While the spectral position of the resonance is fixed after a specific thickness, further modifications primarily impact the reflection intensities rather than the overall color response.
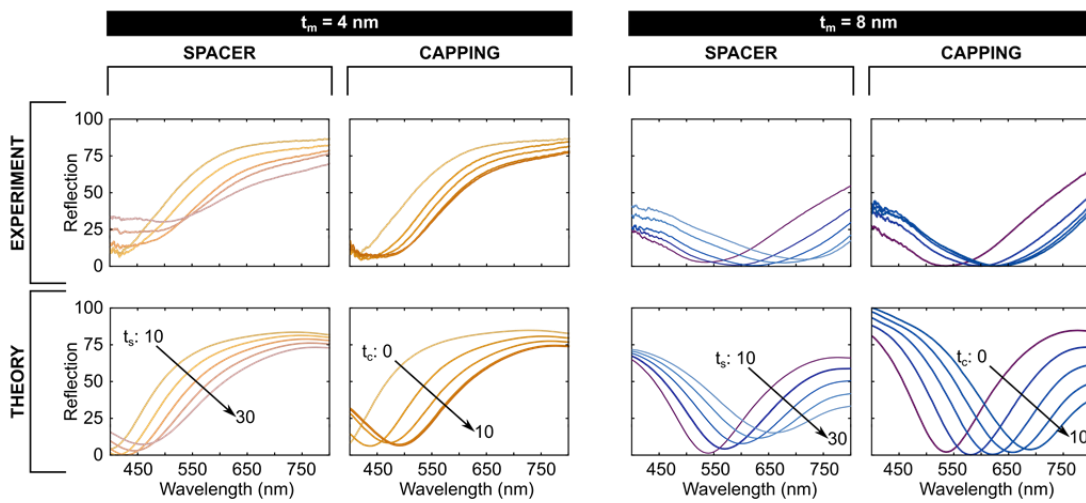
Figure 33 Spacer and capping effect. Comparison of the reflection curves from the measured samples and those predicted by analytical mode where t_m is the thickness deposit alumina (nanoparticles) for 4 nm and 8 nm, t_s thickness spacer, and t_c is thickness capping layer.
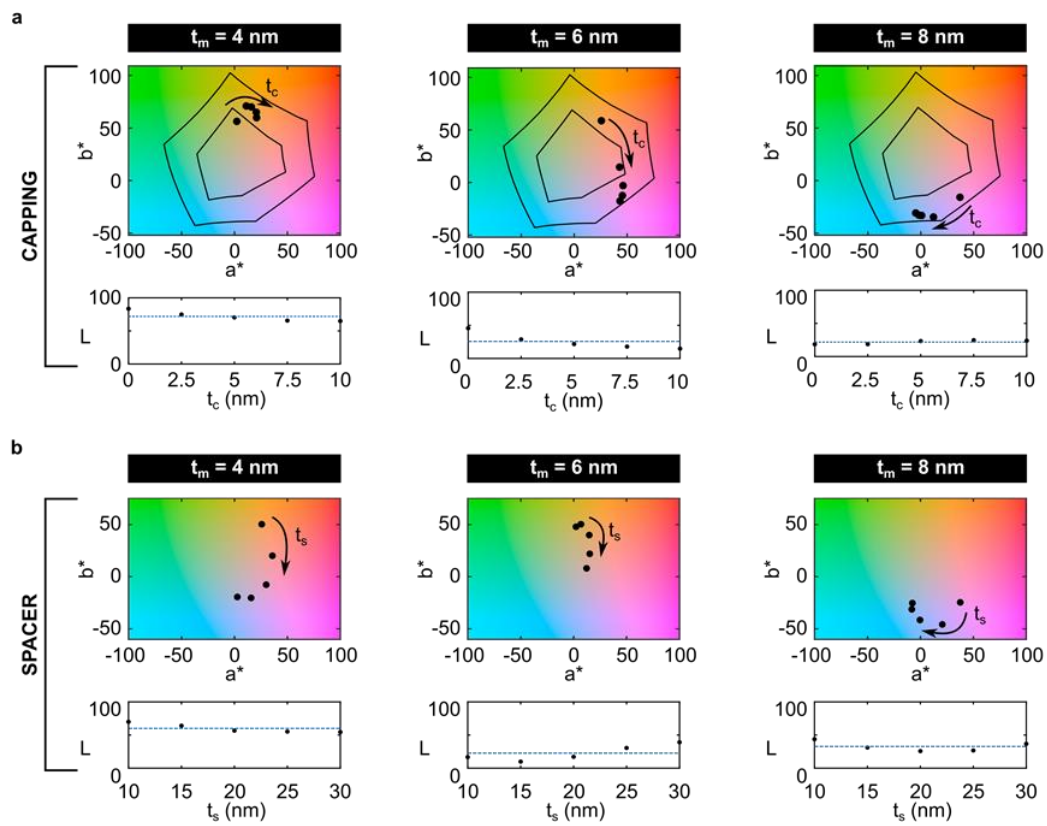
Figure 34 The Figure displays the CIELAB coordinates for analyzing the spacer and capping layers. By adjusting the geometrical parameters of the stack, it is possible to expand the available color gamut. a) shows the CIELAB coordinates for the capped configurations, while b) presents the coordinates for the spacer layers discussed in Figure 29. These coordinates provide a valuable representation of color space achieved by manipulating these layers.
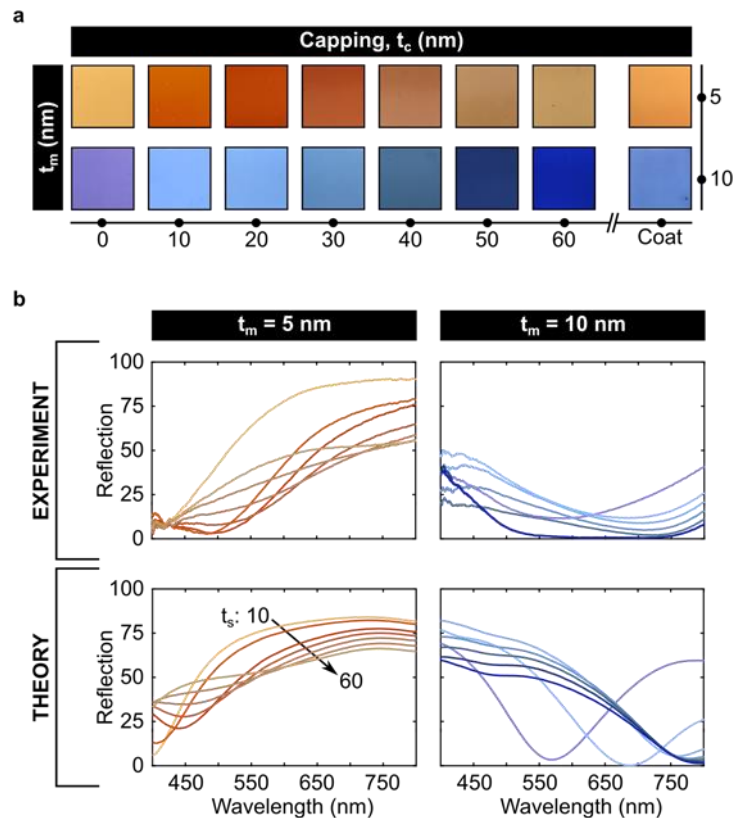
Figure 35a) Camara pictures of the samples with various capping layer Thicknesses and a clear coat are displayed for self-assemblies of 5nm and 10 nm. These visual representations provide insight into the impact of different capping layer thicknesses on the resulting colors. In b) both the samples' measured and analytical reflection curves are presented. This comparing allows for an assessment of the agreement between the experimental data and the analytical model in terms of the reflection properties

As the final element parsed from stack that governs the optical response of the self-assembled plasmonic structure is the transparent aluminum oxide spacer layer, which determines the thickness of the spacer. As illustrate in *Figure 29*d, for samples with mass thicknesses of 4 nm, 6 nm, and 8 nm, and varyting spacer thicknesses from 10 nm to 30 nm, changes in the spacer thickness lead to pronounced color variations in the structure. In particular, for the 6 nm nanoparticles layer, the reflection curves are shown in *Figure 29*e.

As the spacer thickness increases, the structure's resonance shifts towards longer wavelengths and the overall reflection levels are elevated, resulting in less saturated colors. This behavior can be explained by employing the interference theory of a non-symmetric subwavelength cavity. In this model, the bottom mirror and the top nanostructured self-assembly act as the two limiting

76

interfaces. At the same time, the ultra-thin dielectric (alumina) spacer, positioned between them, controls the vertical coupling between the two metallic layer. By manipulating the spacer thickness, the vertical coupling between the metallic layer is modified, leading to changes in the interference patterns within the structure. Consequently, this alters the resonant wavelength and the reflection properties, influencing the perceived color or the self-assembled plasmonic structure.

The describe configuration play a vital role in achieving nearly 100% levels of absorption in the nanostructured plasmonic self-assembled layer. This high absorption is only achieved when there is field enhancement at the nanoparticles layer for wavelengths that satisfy the phase matching condition[61]. In contrast to conventional Fabry-Perot resonators, where the phase accumulates solely through propagation in the dielectric and the resonant condition is limited to cavity lengths proportional to the wavelength of light, the gap-plasmon mode excited on the self-assembled Al nanoislands introduces an interface with non-trivial phase shifts and high losses. This unique dispersive nature allows absorption resonances even for thicknesses much smaller than the resonant wavelength, going deeply into the subwavelength scale. Therefore, carefully controlling the spacer thickness is crucial to achieving optical absorption and vibrant colors in the nanostructured plasmonic self-assembled layer.

Compared to a far-field Fabry-Perot mode, the distinct nature of the near-field coupled gap-plasmon mode becomes more evident with the larger spacer thicknesses. When the dielectric spacing layer reaches significant values (multiples of $\lambda/4n_s$, where n_s is the reflective index of the spacer layer), far-field effects become dominant, and the phase accumulated through propagation can satisfy the resonant condition, similar to conventional Fabry-Perot resonators. This results in a sharp dip in reflection, as shown in *Figure 36*. In *Figure 36* b), both the measured and analytical reflection curves for the samples are shown.

---

[61] Kats, M. A. & Capasso, F. Kats, "Optical absorbers based on strong interference in ultra-thin films," *Laser Photon. Rev.,* vol. 10, pp. 735-749, 2016.

Notably, one can observe the presence of a sharp Fabry-Perot resonance for spacer thicknesses that are large enough. This resonance appears as a distinct dip in the reflection curve, indicating the fulfillment of the resonant condition for the Fabry-Perot mode. Although this resonance offers colors with higher saturation, its purely geometrical nature makes it highly dependent on the angle of observation, thus significantly limiting its practical applications.

On the other hand, the near-field coupled gap-plasmon mode engineered inside the novel self-assembled ultra-thin structure maintains a fundamental advantage. It is not highly angle-dependent and offers a broader range of colors. This advantage makes the near-field coupled gap-plasmon mode versatile and attractive for practical applications than purely geometrical far-field Fabry-Perot resonances.
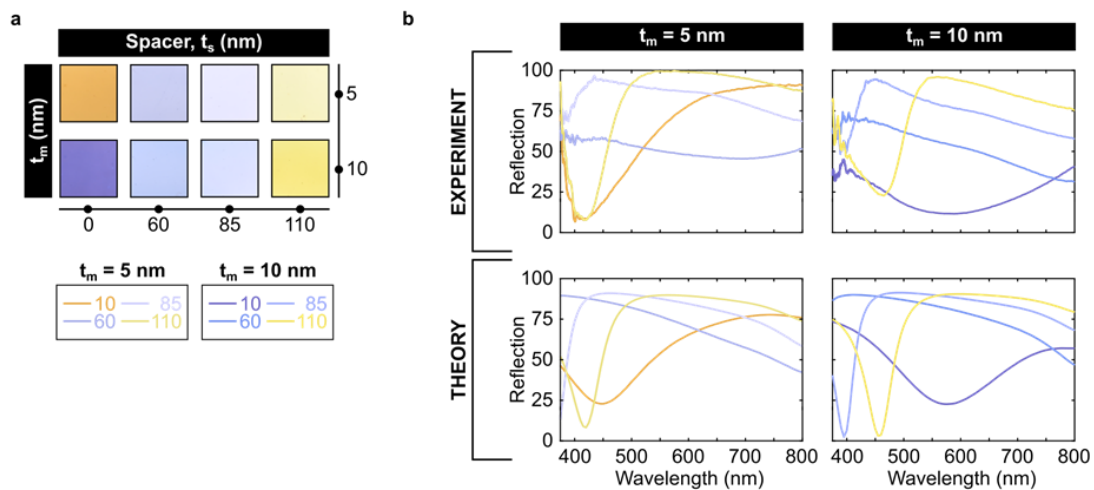
Figure 36 illustrates the limits of tunability through the spacer layer. In a) camera pictures of the samples with various spacing layer thicknesses are presented for 5 nm and 10 nm self-assemblies. The visual representation allows us to observe the impact of different spacing layer thicknesses on the resulting colors. In b), measured and analytical reflection curves for the samples are shown.

The proposed plasmonic self-assembled structure offers a versatile platform for structure coloration. Its growth using conventional evaporation techniques at low temperatures enables using a wide range of substrates. To demonstrate its versatility, we made multicolor butterflies by growing several stacks of different parameters on wing-shaped polyethylene terephthalate (PET) templates, as shown in *Figure 37*a. These color structures

exhibit polarization and angle insensitivity, showcasing their superiority over many other reports structural approaches. The polarization independence of the colors arises from the isotropic nature of the disordered self-assembled layer. The nanoislands in this layer exhibit no predominant direction or orientation of growth. As depicted in *Figure 37* b, no appreciable color difference is observed when the butterfly assembly polarization states. This characteristic highlights the structural strength of colors produced by this plasmonic self-assembled structure under different polarizations, making it a valuable advantage over other methods that may be sensitive to polarization changes.

The multilayer structure's polarization independence is important for integrating into devices that rely on polarized light, such as liquid crystal displays. Additionally, the subwavelength character of the cavity makes the structure highly insensitive to the angle of incidence. Photographic evidence of incidence.

When analyzing the colors produced by the self-assembled structure further, we investigate the angle insensitiveness of the plasmonic self-assembled structure; with the help of Dr. Cencillo we conduced reflection measurements of the three primary samples (*Figure 28* c) at various incident angles using an integrating sphere with a rotatable mount (*Figure 38*). We compared these experimental results with FDTD simulations of a single hemisphere with periodic boundary conditions, as estimated from the central values obtained though SEM analysis. The results demonstrate that the spectral position and reflection levels remain constant for incident angles as large as 60°. Beyond this point, with steeper angle, the amplitude of the resonance gradually decreases, and the spectral position slightly shifts towards the blue end of the spectrum. Notably, the polarization insensitiveness of the stack is result of the disorder morphology of the plasmonic self-assembled layer, where the nanoislands exhibit no predominant direction or growth orientation. On the other hand, the angle insensitiveness is an effect primary due to the subwavelength cavity, which is relatively independent of the specific morphology of the nanoislands. The combined effect of these two features makes the color of the plasmonic self-

assembly simultaneously insensitive to both the angle of incidence and polarization state of light, making it highly versatile and advantageous for various practical applications.

The adaptability of this unique large-are, self-assembling based fabrication method to different substrates allows for the integration of the stack into elastic platforms without compromising color quality. By growing three samples with 5 nm, 8 nm, and 12 nm nanopartucles' layers, along with a fixed 10 nm aluminum oxide spacer, on top of aluminum-coated polyethylene terephthalate (PET) strips, three configurations corresponding to the three primaries in the CYM color mode are achieved, as shown in *Figure 38* d. While vivid and brilliant, the specular coloration observed on flat substrates may not be ideal for all application, but we get that corrugate substrate can produce a diffuse coloration mode. In this mode, corrugate texturing of the substrate controls the degree of light dispersion upon reflection. By growing the nanostack on sandblasted PET strips, as depicted in *Figure 37* e, diffuse coloration is achieved. Unlike flat substrates, microtextured substrates result in surfaces that homogeneously diffuse light without inconvenient light streaks of specular reflection. This approach allows the structure to maintain angle and polarization insensitivity while offering a more aesthetically pleasing and practical coloration mode for various applications.
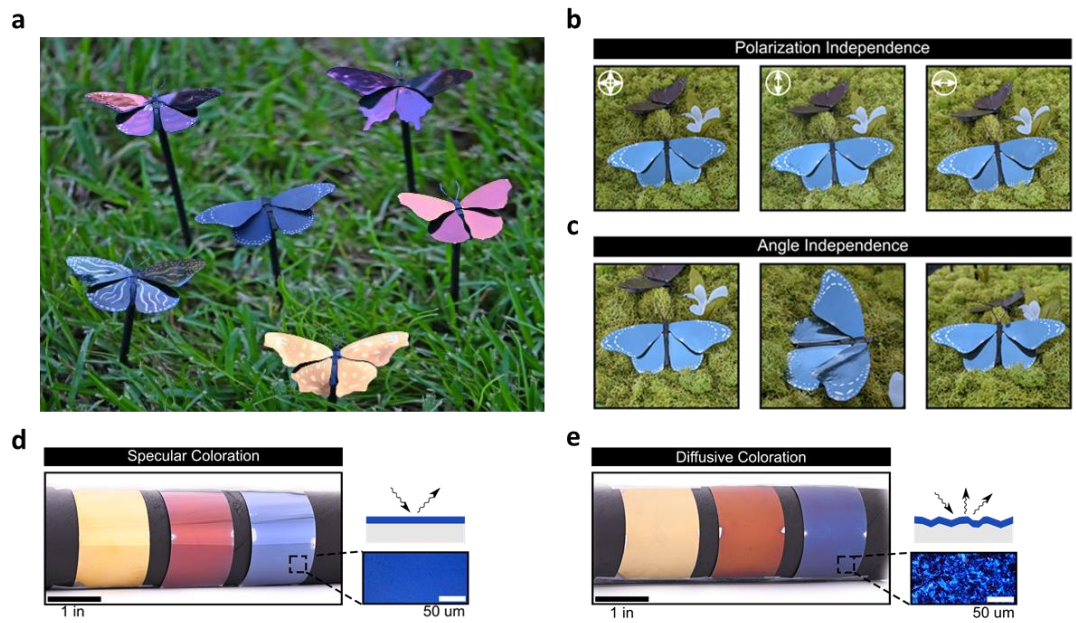
Figure 37 a Butterfly garden, which showcases various butterfly wings of various colors achieves structural coloration; b, Artistic butterfly model coated with structural blue demonstrates its polarization independence. When photographed with unpolarized light (left) and two orthogonal linearly polarized states (center and right), the color remains consistent, highlighting its polarization insensitiveness; c, It shows the butterfly´s color is also angle-insensitive, as evidenced by photographs taken at three different combinations of azimuth and zenith angles, where the color is retained regardless of the angle of incidence; d-e Flat polyethylene terephthalate (PET) strips are used as flexible substrates to form the three primary colors in the specular coloration mode and diffuse coloration mode.
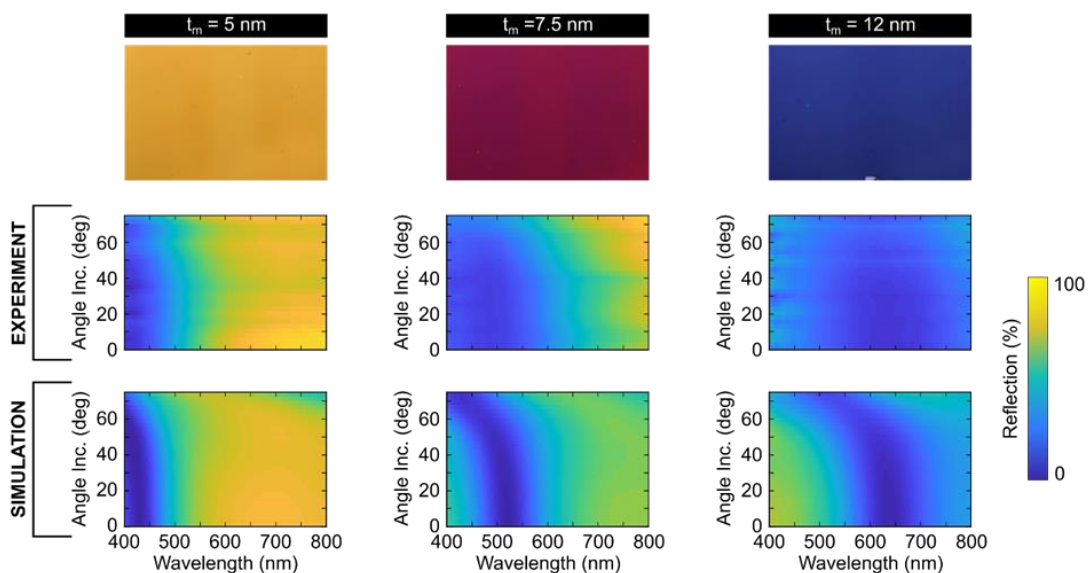
Figure 38 The angle insensitiveness of the subwavelength plasmonic cavity. The top pictures display camera photographs of the samples used for measuring the angle dependency of the structure. The top row represents the reflection levels measured on an integrating sphere. The bottom row of pictures shows FDTD

simulations for a single hemispherical particle. The simulations incorporate square periodic boundary conditions at various angles of incidence. By comparing the experimental reflection levels from the top row with the FDTD simulations from the bottom row, one can observe the consistency of the spectral position and reflection levels across different angles of incidence. This demonstration provides further evidence of the angle insensitiveness of the subwavelength plasmonic cavity, validating its practical applicability in various scenarios

Color Mixing to Expand the Color Gamut. The colors that until now we get by the structural coloration of one nanoislands layer are not permitted to generate colors outside of its boundaries. Generating green shades would therefore require a green basis. Unfortunately, due to its subtractive nature, green production is impossible with plasmonic self-assembly alone. Nonetheless, this limitation can be overcome by growing multilayers of plasmonic nanoparticles, as depicted in *Figure 39*. In this multilayer configuration, two additional geometrical parameters come into play to control the color appearance: the thickness mass of the extra layer and the interspace between the nanoisland films. By introducing these new parameters, it becomes feasible to create green shades and extend the color range beyond what a single-layer plasmonic self-assembled structure is achievable. This enhanced control over color generation opens up exciting possibilities for a broader spectrum of application and manipulation are essential.

We utilized an in-plane mixing scheme to produce a wide variety of green shades. The base structure consists of an aluminum mirror, a 10 nm oxide layer, and 10 nm equivalent of nanoislands (*Figure 39*a), On top of this base structure, we grew three additional top layers with thicknesses of 4 nm, 5 nm, and 6 nm, respectively, with oxide interspaces ranging from 10.5 nm to 22,5 nm, as shown in *Figure 39*b. The reflection curves for the 5 nm equivalent top layer are illustrated in *Figure 39*c. This representation reveals how the out-of-plane mixing scheme effectively expands the color palette, enabling the production of colors that would otherwise be inaccessible with a single plasmonic layer. While the bilayer structures exhibit low levels of reflection due to the double absorption of the two-fold plasmonic layer, carefully studying all geometrical parameters can partially help mitigate this effect. By optimizing the geometrical parameters, it is

possible to achieve improved color reproduction and higher reflection levels, offering a broader range of green shades and enhancing the versatility of the plasmonic self-assembled structure for various applications.
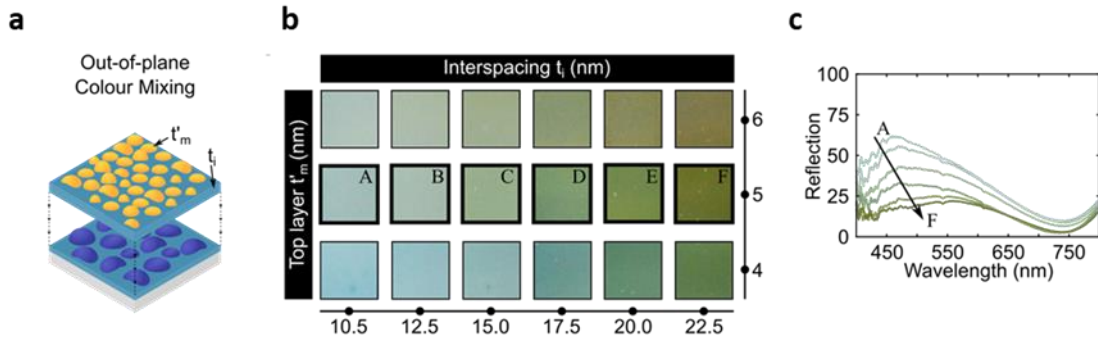
Figure 39a Scheme of Multilayer Structure that generates a new color. b Green shades inaccessible with a single layer can be generated by stacking two self-assemblies with different interspacing thicknesses. c Experimental Reflection of tuning the interspace layer between self-assemblies controls the optical response of the cavity.

Introducing interspace and top-layer geometrical parameter and the bottom self-assembly and spacer layer thickness provide extra degrees of freedom to expand the available color gamut. As elaborated in *Figure 40*, this allows for new colors with different saturation and luminance. From an industrial perspective, incorporating these new layers does not excessively increase the complexity of the manufacturing process. These layers can be grown in the same chamber as a single process step, with minimal additional time and cost. This makes producing multilayer plasmonic structures a viable and practical option for various applications. To incorporate the extra plasmonic film into the analytical model, one can add two additional layers on top of the single stack: the dielectric interspace and an extra effective medium to represent the upper plasmonic layer, where the experimental and theoretical optical answer is shown by reflection curves, which can see in *Figure 40*c. This extension of the model allows for accurate predictions and analysis of the optical properties of the multilayer structure, facilitating the design and optimization of the system for desired color effects.
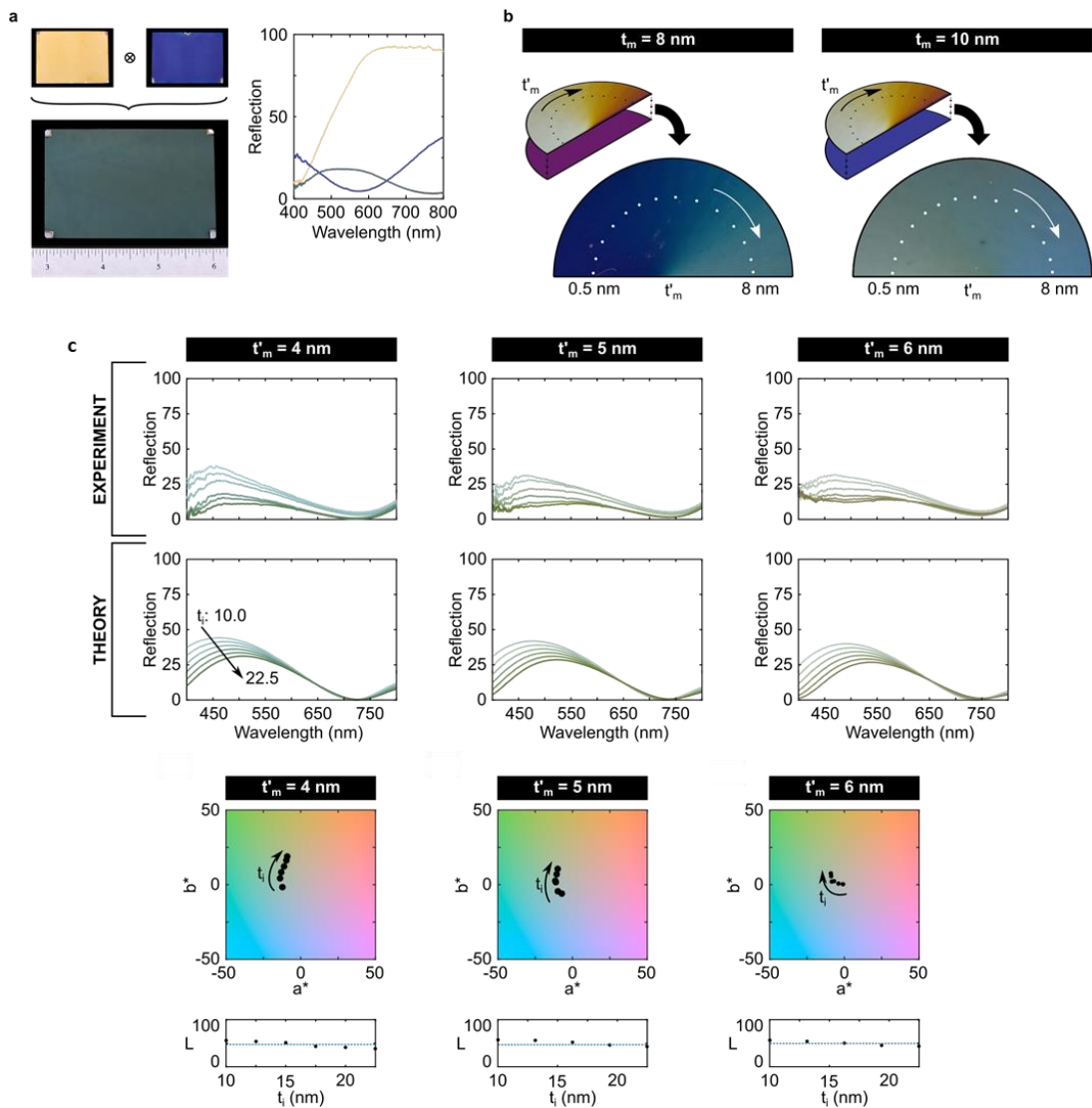
Figure 40a) Sample green can be generated by mixing two self-assembly layers. In this multilayer structure, the bottom self-assembly corresponds to the 12 nm blue, while the top corresponds to the 5 nm self-assembly resulting in yellow. b) Color gamut showing is by different combinations of thickness mass, interspacing, and bottom and top self-assembled layers offer extra freedom to produce green shades with higher brilliance and saturation. c) Reflection curves for green shades of Figure 12b. Reflection curves at the top correspond to the measured curves whereas the bottom ones correspond to the predicted values from the analytical model. The CELAB coordinates for all interspaces and top nanoparticles layers corresponding to 4, 5, and 6 nm self-assembly for green shades of Figure 12b.

Structural Color Paint. In industry, it is possible to use the fabrication process for growing the self-assembled structure, utilizing compatible systems. However, there is a fundamental limitation due to the requirement for structure growth on the substrate. This restriction critically affects the applicability of the platform in contexts where non-vacuum-compatible substrates are needed or

when large areas need to be covered. In such cases, the particular specifications of the evaporation equipment would always be a limiting factor. One alternative to commercial chemical colorants is the multilayer structure on a stand-alone platform that can be transferred, after fabrication, to any substrate. One potential solution to achieve this is to use a sacrificial layer as temporary support; the sacrificial layer used was S1813(MicroChem corp) and baked on a hotplate of 115°C for 5 min and after a double-sided mirror-symmetric stack was evaporated, where each side comprises an alumina-protecting capping layer, plasmonic self-assembly, and an alumina spacer. The mirror is shared between the two sides. The stack was liftoff of the substrate with acetone for the color subtraction finish. By employing this approach, a stand-alone multilayer structure can be produced, which can then be transferred to different substrates as needed. This method offers a more versatile and practical way to apply the plasmonic multilayer structure to a wide range of applications, including those requiring non-vacuum-compatible substrates or significant area coverage.

Removing the sacrificial layer at the end of the fabrication process yields tunable, self-standing, doubly-colored flakes, as shown in *Figure 41*a. By choosing to grow the structures symmetrically, a homogeneous colorization is ensured. However, growing flakes in asymmetric configurations are possible, where each face displays a different color. After separating the structures from the substrate, flakes are formed where the resulting flakes can be stored in a dry powder form, as depicted in *Figure 41*b, or kept in an organic solvent, such as acetone, as shown in *Figure 41*c. The flakes exhibit irregular shapes and sizes, with lateral dimensions ranging from 20 to 150 μm. To increase homogeneity coating efficiency, we made smaller and more regular flakes because including improved coating efficiency, enhanced adhesion strength to the substrate, and better color finish quality[62]. They also benefit the paint formulation chemistry by reducing the agglomeration of pigments.

---

[62] R. Woodbridge, Principles of Paint Formulation, NY: Springer New York, 1991.

While controlling size and shape thought pre-seeded substrates or patterned sacrificial layers is possible, it increases the complexity of the fabrication process, potentially diminishing the advantage of the structural paint. For this reason, it is employed a final step involving ultrasonication (Qsonica LLC) and filtering (Gilson Company Inc.) is employed to achieve homogeneity and efficiency in coatings. In the ultrasonication step, the flakes are broken into smaller portions with lateral sizes in the range of 10s of μm. Subsequently, filtering using a sieve with a 20 sq. μm mesh is performed to separate bigger particulates and contaminants from the controlled-size flakes. This process effectively improves homogeneity, as *Figure 42a* demonstrates.

The ultrathin nature of the structural paint, with a thickness of only 150 nm, provides a significant advantage compared to traditional chemical coloration, which often requires several microns of thickness for full coloration. As a result, structural paint is the coating layer is only 0.25 mg/sq. in (0.388 g/m^2), as shown in *Figure 42*b. A comparison is made to demonstrate the fundamental advantage of ultralight paint with current paint technologies used on Boeing airliners. The weight of the paint alone accounts for approximately 500 kg of a Boeing aircraft[63], with paint thicknesses between 90 and 140 μm. However, with the self-assembled structural paint's density being almost 4 to 8 times lighter than the current paint, a Boeing coated with the structural paint would only add 1.3 kg of extra weight. This significant weight reduction saves weight equivalent to 4-8 adult passengers, making it an outstanding choice for achieving ultralight paint.

---

[63] T. B. Company, "Boeing: 747-8," [Online]. Available:
https://www.boeing.com/commercial/747/. [Accessed 2022]
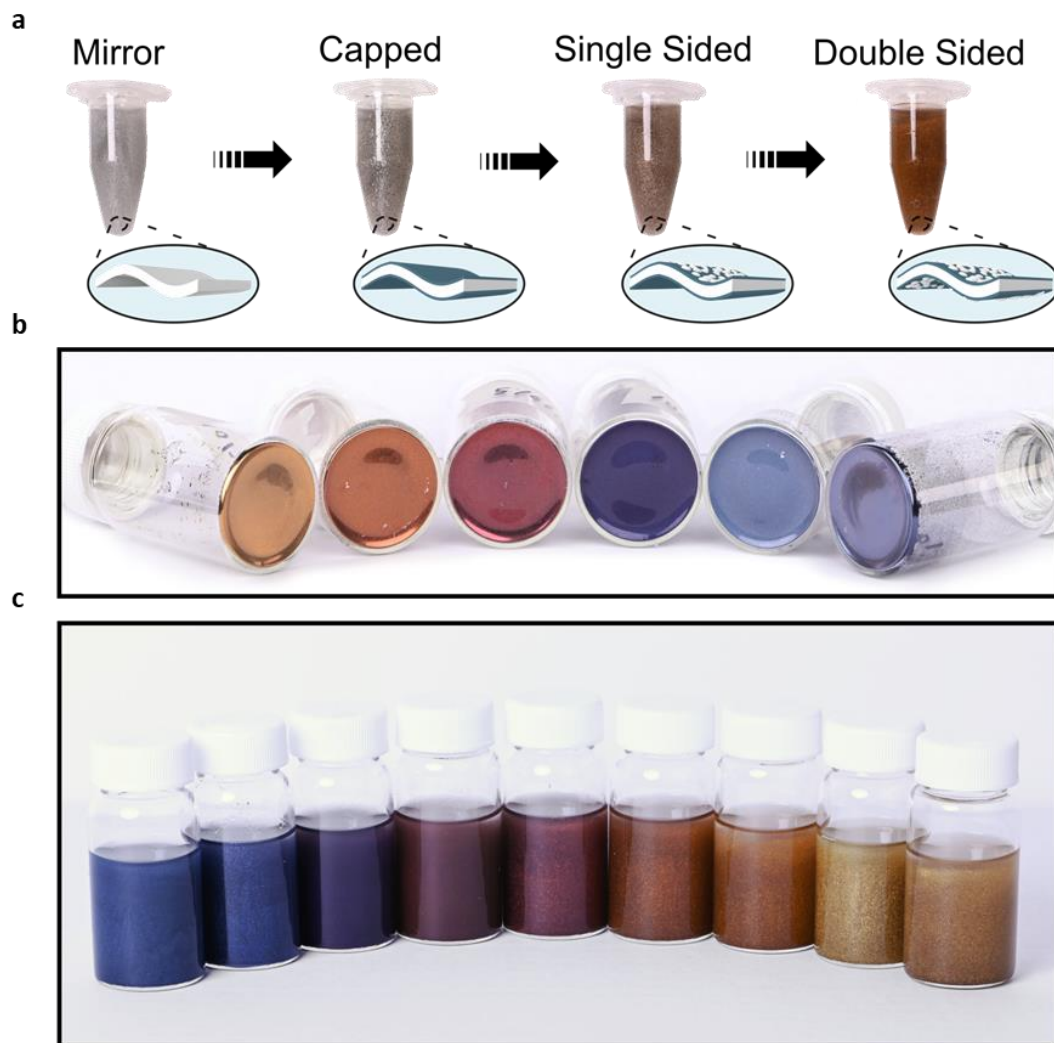
Figure 41 Showcases the Structural Color Paint and its commercial potential: a) The sequential growth of the bi-directional stack results in the formation of color flakes. b) color flakes can be stored dry, maintaining their structural color properties. c) Alternatively, color flakes can be dispersed in solution to create the structural color paint.

a

b
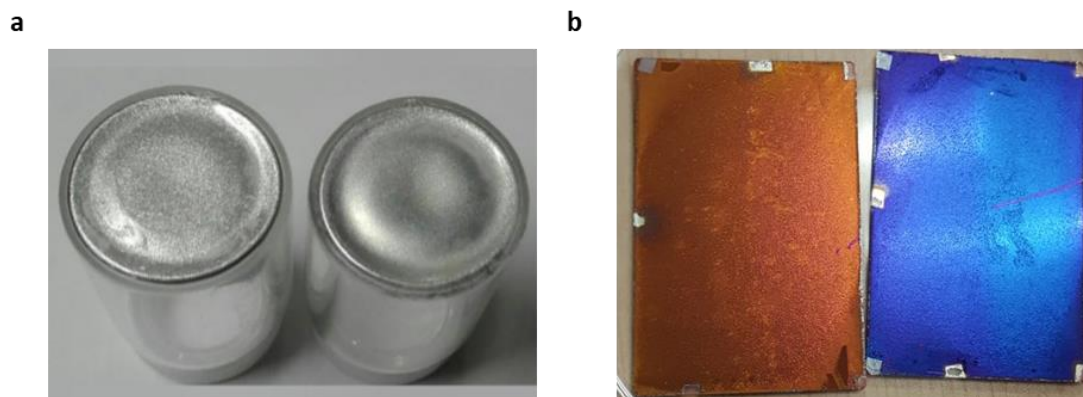
Figure 42 a) Flakes as liftoff (left) and after sonication and sintering (right): The image shows flakes before and after undergoing sonication and sintering processes. These treatments are carried out to ensure that the flakes achieve smaller dimensions, typically in the range of 10s of μm, resulting in a higher level of homogeneity in the coatings. b) The image displays two glass substrates coated with the self-assembly structural paint, and the combined weight of the paint on both substrates is only 5 mg, spread over a substantial 20 sq. in area. In contrast, traditional commercial paints require several microns to archive similar coloration. This paint provides full coloration with just a minute footprint of 150 nm.

The commercial potential of this platform for inorganic metallic pigmentation is demonstrated by formulating a paint that involves mixing the structural color flakes with a drying oil. Such as linseed oil from Gamblin (*Figure 43*a). This mixture of the flakes acting as the pigment and the oil serving as the binder represents the simplest form of paint, allowing the transfer of color to the target substrate. The resulting paint can be used to coat surfaces in applications that are otherwise incompatible with vacuum system. As shown in *Figure 43*b, the structural color paint is successfully used to paint an artistic multicolor butterfly on a black canvas. While different target surfaces may be used, these require a more careful binder selection and possibly include other chemical additives in the paint formulation. The structural color paint that is presented in this work is easily adaptable. As long as non-corrosive chemical are used, the self-assembled structure of the flakes provides a universal platform independent of the specific paint composition.
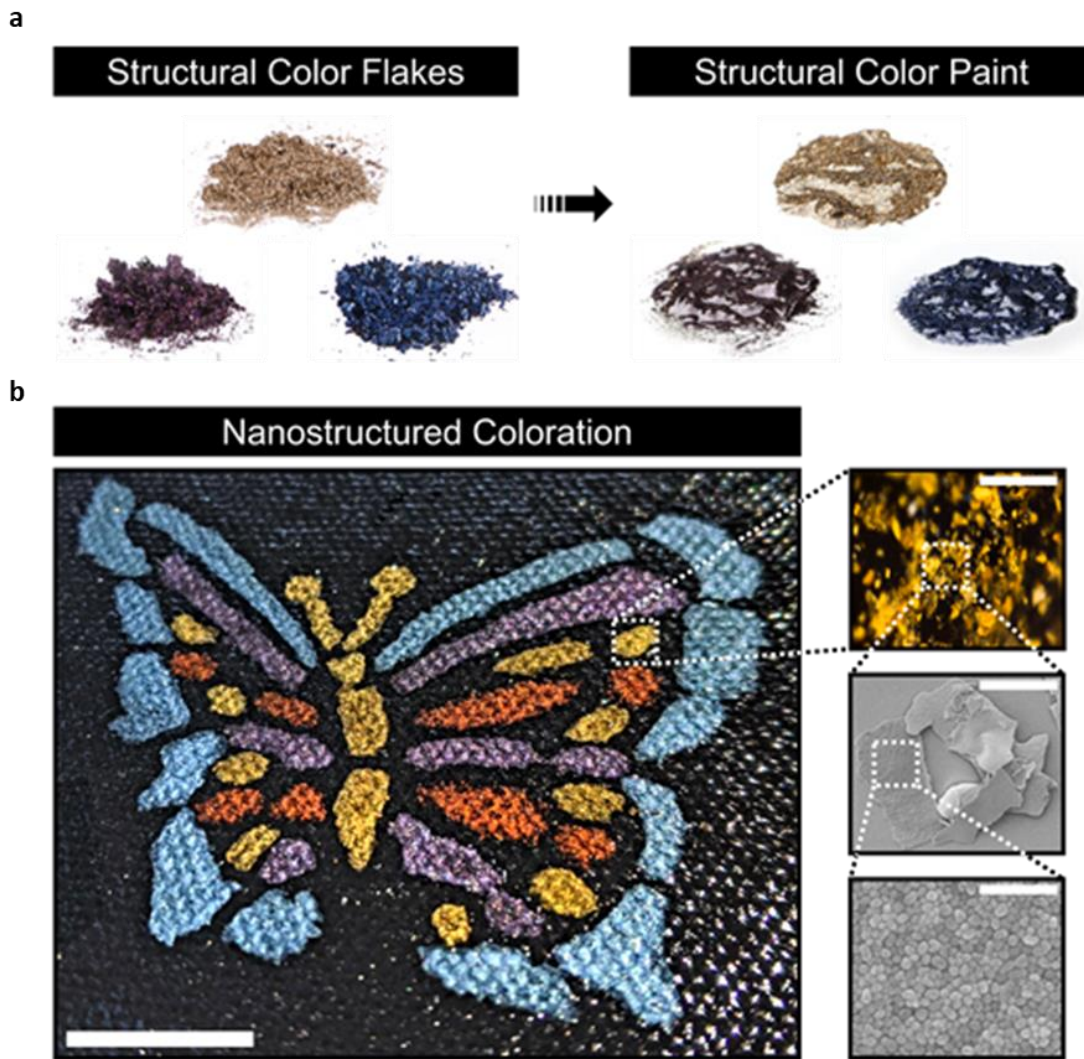
Figure 43a) The structural color paint is produced by mixing the flakes with a drying oil, where the flakes act as pigments and the oil serves as the binder. b) A multicolor artistic butterfly is painted on a black canvas using a set of linseed oil-based plasmonic paints, demonstrating the commercial feasibility of the platform. The insets show a microscope image (right-top) and SEM micrographs (right-bottom) of the structural color flakes. The scale bar for the butterfly is 1 inch, and for the insets, it corresponds to 1 mm, 100 um, and 150 nm, respectively

The structural color paint exhibits two additional features that make it a highly promising candidate for industrial production. Firstly, unlike traditional chemical coloration schemes often involving toxic and contaminant components, structural color paint employs only nontoxic materials, such as aluminum and its oxide, along with a biodegradable, water-soluble polymer as a sacrificial layer. This eco-friendly approach avoids detrimental environmental impacts, making the paint a more sustainable and responsible choice for various applications.

Secondly, the structural color paint offers exceptional optical properties. With just a single ultra-thin layer of pigment, measuring between 100 and 150 nm in thickness pigment of extremely low surface density, it is possible to have 100% reflection. This is an extraordinary characteristic of a paint that provides full coloration with minimal material usage. The low surface density of the pigment further contributes to its advantages in weight-saving applications, as mentioned earlier.

4.1.6. Discussion and Conclusions

Structural coloration offers a promising opportunity to replace chemical colorants with purer and non-toxic alternatives. However, the commercial production of structural color presents challenges due to anisotropic optical responses that lead to undesired effects like dichroism or iridescence, coupled with complex and time-consuming fabrication processes. In this work, we have successfully addressed these challenges by introducing a color nanostructure that opens up industrial production opportunities. By combining the plasmonic response metallic self-assembly with an ultrathin optical cavity, we demonstrated that we could obtain an extensive CYM color palette, which can be easily achieved by adjusting the geometrical parameters of the structure. Furthermore, we have explored mechanisms for expanding the available color space through multilayers, allowing cost-effective color mixing to enhance the color gamut further. The isotropic nature of the nanoislands' layer ensures polarization independence, the structure's angle insensitiveness is achieved by exploiting non-trivial phase discontinuities in the ultrathin cavity, and for the steep angles close to 70° avoids the path length effects, enabling efficient self-assembly that is a characteristic unimaginable to achieve in conventional Fabry-Perot resonators.

Building a subwavelength plasmonic cavity involving a low-temperature fabrication process within an E-beam evaporator was possible. This approach offers remarkable versatility, allowing for its implementation on various substrates whit flexible platforms necessary for wearable electronics manufacturing. Moreover, the structure adapts to the scattering properties of the

target surface, enabling the generation of both diffuse and specular modes of coloration. An additional advantage lies in its self-assembly nature, which ensures consistent color across large areas. Characterizing the structure, we observed that the purity of color produced by our structure is closely tied to the size and shape distribution of the nanoislands. It is possible to improve the control over the assembly´s morphology of the structure using pre-seeding techniques, elevated temperatures, or alternate materials. However, it introduces scalability and cost challenges to the manufacturing process.

We have engineered self-dependent bi-directional color flakes to showcase the commercial viability of our platform in producing inorganic metallic pigments. This is accomplished by depositing a double-sided stack onto a water-soluble sacrificial layer. These remarkably lightweight pigments exhibit full coloration with just a single layer of flakes. Combined with a binder matrix, they can be fashioned into a structural color paint that applies to coat various surfaces post-manufacturing. This pioneering method offers an ultra-light, multi-color, large-scale, cost-effective and eco-friendly means of introducing nanostructured coloration to diverse surfaces. With an unmatched surface density of 0.4 g/m^2, significantly lighter than commercially available paints.

4.2.   Tunability color as a detection tool

The production of structural colors using plasmonic resonances has garnered significant attention in recent years[64] [65] [66] [67]. In plasmonic coloration,

---

[64] N.Dushkina, A.Lakhtakia, In Engineered Biomimicry, Elsevier, 2013, pp. 267-303.

[65] Z. Xuan, J. Li, Q. Liu, F. Yi, S. Wang, W. Lu, "Artificial Structural Colors and Applications," The Innovation, vol. 2, no. 100081, 2021.

[66] Yulan Fu, Cary A. Tippets, Eugenii U. Donev and Rene Lopez, "Structural colors: from natural to artificial systems," *WIREs Nanomed Nanobiotechnol,* vol. 8, no. 758, 2016.

[67] S. Daqiqeh Rezaei, Z. Dong, J. You En Chan, J. Trisno, R. J. H. Ng, Q. Ruan, C. W. Qiu, N. A. Mortensen, J. K. W. Yang, "Nanophotonic Structural Colors," *ACS Photonics,* vol. 8, no. 18, 2020.

the color emerges due to specific bands of incident light absorbed by the constituent metallic nanoparticles. Notably, these absorption bands can be easily adjusted by modifying the structural geometrical parameters or the material characteristics, thereby allowing for precise color tuning (see Self-assembled Plasmonic paint). Consequently, any external alterations that influence material properties, structure geometry, or environmental conditions will inevitably lead to alterations in their optical response, perceived as changing color. This property positions them as a versatile platform for sensing applications.[68] [69] [70]

Notably, metallic nanostructures have unlocked the potential to craft color-based structures from initially colorless materials. These structures, known as plasmonic structural colors, possess environmental sensitivity. Taking advantage of this characteristic, we use the same concept of the plasmonic structure previously studied and characterized by this working group to make it a promising platform for moisture detection. We present a unique configuration involving the self-assembly of aluminum nanoparticles in close proximity to a mirror, separated by an ultrathin layer of poly(N-isopropylacrylamide) (PNIPAM). By integrating the plasmonic system with this active polymer layer, we establish a thermoresponsive gap-plasmon architecture. This architecture translates temperature and relative humidity alterations of the environment into observable shifts in color. The intriguing feature of this setup is the exploitation of PNIPAM's environmentally-triggered structural modifications, which result in a 7 nm resonance shift for every 1 nm change in the polymer's thickness, ultimately leading to changes in color. This system's transformation is fully reversible, making it suitable for sensing for colorimetric, self-powered by humidity and temperature, and reusable. Notably,

---

[68] J. Mejía-Salazar, O. N. Oliveira, "Plasmonic Biosensing," *Chemical reviews,* vol. 118, no. 20, pp. 10617-10625, 2018.

[69] King, Nicholas S. and Liu, Lifei and Yang, Xiao and Cerjan, Benjamin and Everitt, Henry O. and Nordlander, Peter and Halas, Naomi J., "Fano Resonant Aluminum Nanoclusters for Plasmonic Colorimetric Sensing," *ACS Nano,* vol. 9, no. 11, pp. 10628-10636, 2015.

[70] Fan, Jiao-Rong and Zhu, Jia and Wu, Wen-Gang and Huang, Yun, "Plasmonic Metasurfaces Based on Nanopin-Cavity Resonator for Quantitative Colorimetric Ricin Sensing," *Small,* vol. 13, no. 1, p. 1601710, 2017.

if condensation occurs on the structure, the polymer layer undergoes a non-recoverable deformation, eliminating, the polymer layer undergoes a non-recoverable deformation, eliminating the colors.

4.2.1. Poly N-isotropylamide (PNIPAM)

Numerous polymers can be structurally and materially adjusted through external stimuli like electric fields, mechanical stress, temperature, humidity, or changes in environmental pH[71][72][73]. Incorporating these responsive polymers into a structural coloration framework provides an innate and straightforward avenue for colorimetric sensing, holding promise for diverse chemical and biomedical applications.[74]

---

[71] J. H. Meng H, "A Brief Review of Stimulus-active Polymers Responsive to Thermal, Light, Magnetic, Electric, and Water/Solvent Stimuli," *Journal of Intelligent Material Systems and Structures.,* vol. 21, no. 9, pp. 859-885, 2010.

[72] Siyang Wang, Qianhui Liu, Lei Li, Marek W. Urban, "Recent Advances in Stimuli-Responsive Commodity Polymers," Macro Molecular Rapid Communications, vol. 42, no. 18, p. 2100054, 21.

[73] Ibekwe, Jinlian Hu and Harper Meng and Guoqiang Li and Samuel I, "A review of stimuli-responsive polymers for smart textile applications," Smart Materials and Structures, vol. 21, no. 5, p. 053001, 2012.

[74] Serpe, Molla R. Islam and Zhenzhen Lu and Xue Li and Avijeet K. Sarker and Liang Hu and Paul Choi and Xi Li and Narek Hakobyan and Michael J., "Responsive polymers for analytical applications: A review," Analytica Chimica Acta, vol. 789, no. 0003-2670, pp. 17-32, 2013.

In this work, we use one particular dynamic polymer that has drawn considerable attention recently, poly(N-isopropylacrylamide)(PNIPAM)[75] [76] [77] [78] [79] . PNIPAM is recognized as a thermoresponsive polymer that displays a distinctive lower critical solution temperature (LCST) transition. Around 32°C, this phase transition is characterized by a shift from a hydrophobic to a hydrophilic phase (*Figure 44*a). The transition's reversibility stems from alterations in hydrogen bonding within the polymer chains[80] [81]. At temperatures below the LCST, the polymer absorbs water and swell; however, when the temperature surpasses the LCST, the polymer shifts to a hydrophobic state, expelling absorbed water and consequently reducing its volume (*Figure 44*b). It has been reposted that is possible to deposit a layer of PNIPAM onto an existing plasmonic structure for temperature-sensing applications. When a temperature variation occurs, the polymer undergoes a phase transition, resulting in a conformal change in the polymer layer. This transformation subsequently impacts the environment around

[75] Y. S. &. D. W. Muhammad Abdul Haq, "Mechanical properties of PNIPAM based hydrogels: A review," Materials Science and Engineering: C, vol. 70, no. 0928-4931, pp. 842-855, 2017.

[76] Lin Tang, Ling Wang, Xiao Yang, Yiyu Feng, Yu Li & Wei Feng, "Poly(N-isopropylacrylamide)-based smart hydrogels: Design, properties and applications," Progress in Materials Science, vol. 115, no. 0079-6425, p. 100702, 2021.

[77] Deng Z, Guo Y, Zhao X, Du T, Zhu J, Xie Y, Wu F, Wang Y, Guan M, "Poly(N-Isopropylacrylamide) Based Electrically Conductive Hydrogels and Their Applications," *Gels,* vol. 8, no. 5, pp. 2310-2861, 2022.

[78] Xu X, Liu Y, Fu W, Yao M, Ding Z, Xuan J, Li D, Wang S, Xia Y, Cao M, "Poly(N-isopropylacrylamide)-Based Thermoresponsive Composite Hydrogels for Biomedical Applications," *Polymers,* vol. 12, no. 3, pp. 2073-4360, 2020.

[79] M. E. Shahin Homaeigohar, "Switchable Plasmonic Nanocomposites," *Advanced Optical Materials,* vol. 7, no. 1, p. 1801101, 2018.

[80] Otake, Katsuto and Inomata, Hiroshi and Konno, Mikio and Saito, Shozaburo,"Thermal Analysis of the Volume Phase Transition with N-Isopropylacrylamide Gels.," *Macromolecules,* vol. 23, no. 1, pp. 283-289, 1990.

[81] Malham, I. B., & Bureau, L, "Density effects on collapse, compression, and adhesion of thermoresponsive polymer brushes.," *Langmuir : the ACS journal of surfaces and colloids,* vol. 26, no. 7, p. 4762–4768., 2010.

the metallic resonators, leading to noticeable alterations in the sensor's optical response[82]. Essentially, this hybrid mechanism functions as a refractive index sensor.
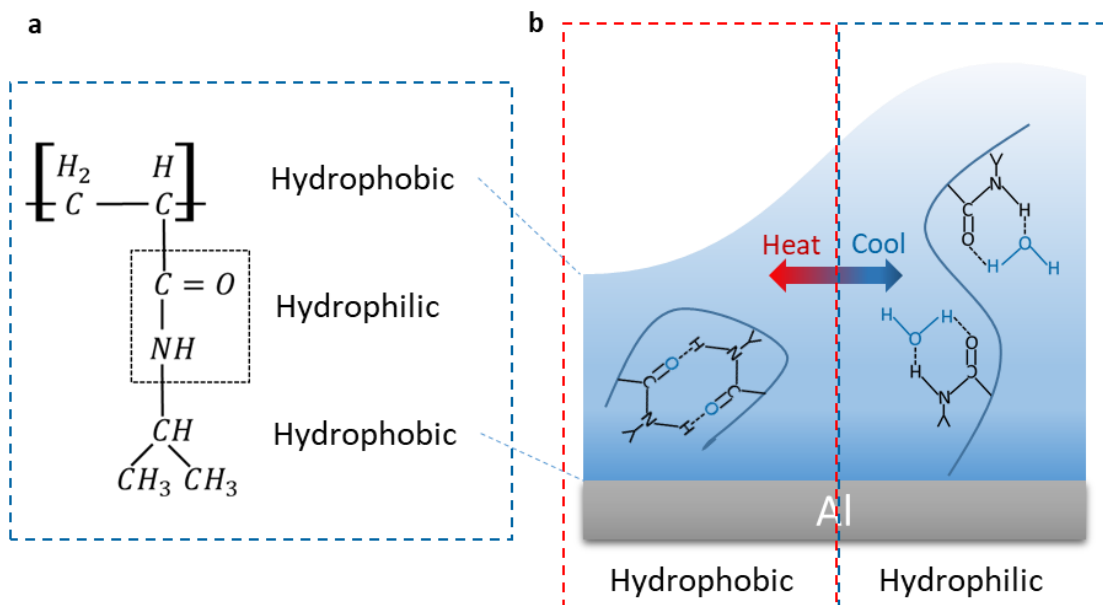
Figure 44 a) Chemical structure of PNIPAM indicating hydrophobic and hydrophilic regions . b) Schematic diagram of the phase transition when the temperature is < LCST, the polymer absorbs water and swells; when the temperature is > LCST, the polymer expels absorbed water, consequently reducing its volume.

It should be pointed out that the growth of PNIPAM shells on the metal core requires the grafting of PNIPAM brushes onto the plasmonic substrate[83] [84]

[82] Jiang, Nina and Zhuo, Xiaolu and Wang, Jianfang, "Active Plasmonics: Principles, Structures, and Applications," *Chemical Reviews,* vol. 118, no. 6, pp. 3054-3099, 2018.

[83] Carregal-Romero, S. Buurma, N.J. Pérez-Juste, J. Liz-Marzán, L.M. Hervés, P., "Catalysis by Au@pNIPAM nanocomposites: Effect of the cross-linking density," *Chemistry of Materials,* vol. 22, no. 10, pp. 3051-3059, 2010.

[84] Contreras-Cáceres, R., Pacifico, J., Pastoriza-Santos, I., Pérez-Juste, J., Fernández-Barbero, A., & liz-Marzán, L. M."Au@pNIPAM Thermosensitive Nanostructures: Control over Shell Cross-linking, Overall Dimensions, and Core Growth.," *Advanced Functional Materials,* vol. 19, no. 19, pp. 3070-3076, 2009.

[85] [86] [87]. Although this approach offers immediate practical utility, it poses challenges in terms of scalability due to the intricate and time-consuming nature of the process, the stringent environmental conditions required during growth, limitations in brush density, and substrate compatibility[88] [89]. The growing interest in exploring the PNIPAM in ultrathin films and adding components to modify or control some of its characteristics shows us significant differences from their

[85] [57] Nguyen M., Kherbouche I., Braik M., Belkhir A., Boubekeur-Lecaque L., Aubard J., Felidj N., "Dynamic Plasmonic Platform To Investigate the Correlation between Far-Field Optical Response and SERS Signal of Analytes," *ACS Omega,* vol. 4, no. 1, pp. 1144-1150, 2019.

[86] Mana Toma, Ulrich Jonas, Anca Mateescu, Wolfgang Knoll, and Jakub Dostalek, "Active Control of SPR by Thermoresponsive Hydrogels for Biosensor Applications," J. Phys. Chem. C, vol. 117, no. 22, pp. 11705-11712, 2013.

[87] Hélène Gehan, Claire Mangeney, Jean Aubard, Georges Lévi, Andreas Hohenau, Joachim R. Krenn, Emmanuelle Lacaze, and Nordin Félidj, "Design and Optical Properties of Active Polymer-Coated Plasmonic Nanostructures," *J. Phys. Chem. Lett.,* vol. 2, no. 8, pp. 926-931, 2011.

[88] Yang, Lei and Fan, Xiaoguang and Zhang, Jing and Ju, Jia, "Preparation and Characterization of Thermoresponsive Poly(N-Isopropylacrylamide) for Cell Culture Applications," Polymers, vol. 12, no. 389, 2020.

[89] O. Guselnikova, P. Postnikov, Y. Kalachyova, Z. Kolska, M. Libansky, J. Zima, V. Svorcik, O. Lyutakov, "Large-Scale, Ultrasensitive, Highly Reproducible and Reusable Smart SERS Platform Based on PNIPAm-Grafted Gold Grating," *ChemNanoMat,* vol. 3, no. 2, pp. 135-144, 2016.

brush counterparts[90] [91] [92] [93]. Specifically, the heightened surface-to-volume ration becomes crucial for these ultrathin films, emphasizing the significance of interface contributions and enabling water absorption from the surrounding air[94]. In essence, the transition of transition of ultrathin PNIPAM films is contingent not only on temperature but also on the moisture content of the environment[95]. Consequently, sensors incorporating ultrathin PNIPAM can serve dual purposes by facilitating temperature and humidity detection when integrated with plasmonic structures. In this work, we combined PNIPAM with plasmonic nanostructures to create a system that exhibits color changes in response to variations in temperature or humidity. In the subsequent chapter, we demonstrated the technique of self-assembling a layer of PNIPAM with aluminum nanoparticles over a substrate (aluminum mirror).

[90] Weinan Wang, Ezzeldin Metwalli, Jan Perlich, Kordelia Troll, Christine M. Papadakis, Robert Cubitt, Peter Müller-Buschbaum, "Water Storage in Thin Films Maintaining the Total Film Thickness as Probed with in situ Neutron Reflectivity," Macro Molecular Rapid Communications, vol. 30, no. 2, pp. 114-119, 2009.

[91] Harms S, Rätzke K, Faupel F, et al., "Free Volume and Swelling in Thin Films of Poly(N-isopropylacrylamide) End-Capped with n-Butyltrithiocarbonate," Macromol Rapid Commun, vol. 31, no. 15, pp. 1364-1367, 2010.

[92] G. K. J. P. C. M. P. A. M. B. K. A. L. K. S. R. R. S. V. R. R. C. a. P. M.-B. W. Wang, "Recently, there has been a growing interest in exploring spun-coated ultrathin PNIPAM films as an alternative approach [36–39]. Intriguingly, these ultrathin films exhibit significant differences compared to their brush counterparts.," Macromolecules, vol. 43, no. 5, pp. 2444-2452, 2010.

[93] E. M. J. P. C. M. P. R. C. a. P. M.-B. W. Wang, "Cyclic Switching of Water Storage in Thin Block Copolymer Films Containing Poly(N-isopropylacrylamide)," Macromolecules, vol. 42, no. 22, pp. 9041-9051, 2009.

[94] Y. L. a. K. Sakurai, "Thermoresponsive Behavior of Poly(N-isopropylacrylamide) Solid Ultrathin Film under Ordinary Atmospheric Conditions," CSJ Journals, vol. 46, no. 4, pp. 495-498, 2017.

[95] Y. L. a. K. Sakurai, "Thickness Changes in Temperature-Responsive Poly(N-isopropylacrylamide) Ultrathin Films under Ambient Conditions," ACS Omega, vol. 4, no. 7, pp. 12194-12203, 2019.

4.2.2. Experimental Methodgy

PNIPAM Ultrathin Film. We provided a detailed method for preparing PNIPAM ultrathin films.

- **Substrate Preparation:** Use a clean microscope slide of 1x1 sq. in. with an optically thick aluminum layer (100 nm) as the substrate for the polymer layer. Ebeam deposited the aluminum mirror; this technique is explained in the third chapter of this thesis.

- **Polymer Solution Preparation:** Dissolve 200mg of Poly(N-isopropylacrylamide) (Molecular weight $\sim 40,000$, from Sigma-Aldrich) in a solution consisting of 19g ethanol (200 proof, Sigma-Aldrich) and 1 g of pure water (18.2 MΩ, Thermo Scientific). Adding water enhances wettability, ensuring a smooth layer on the mirror substrate. This was observed under the microscope when analyzing the samples prepared with water and without, showing the film-microfractures observed in the anhydrous mixture and without anhydrous.

- **Stirring and Solution Maturity:** Stir the solution overnight at room temperature.

- **Spin Coating:** Apply 1mL of the prepared solution on the substrate. Spin coat at 3000 rpm for 30 seconds to achieve ultrathin films of approximately 35.5 nm thickness.

- **Annealing:** Annealing the samples at 70°C for 3 hours; we used a Fisherbrand Isotemp.

- **Desiccator Storage:** Store the samples overnight in a desiccator.

The samples are ready to proceed with the self-assembly growth after the prepared PNIPAM ultrathin films. To characterize the samples, the contact angle measurements were performed to assess the hydrophilic and hydrophobic of the surface by dropping 10μL water on a thermostage that controls substrate temperature. The result is shown in the next section of this chapter.

Self-Assembled Structural Color Fabrication. Below, we describe the information about the fabrication process.

After depositing an optically thick back-mirror onto a clean substrate using an e-beam evaporator and applying the PNIPAM ultrathin film by spin-coating, we start the Self-Assembly Growth.

1. **The Self-Assembly Growth PNIPAM/ Nanoparticles aluminum:** We use aluminum again to deposit of nanoparticles in the self-assembly, which was already characterized by this same laboratory team and explained above. We chose to keep the temperature of the substrates at 70°C for high color saturation while being below PNIPAM polymer. We used e-beam evaporating; this technique is described in Chapter 3, and we used pressures below 5×10^{-8} Torr for the growth of nanoparticles, while growth rates were kept constant at about 0.1 A/s to ensure Volmer-Weber growth. The deposit of aluminum nanoparticles is 4.5 nm thickness, a parameter controlled during evaporation.

   Analyze of Films. To study their morphology, analyzed the PNIPAM and self-assembly films using AFM (Atomic Force Microscope) and SEM (Scanning Electron Microscope) systems. It is possible to see the surface roughness of 2nm for PNIPAM, which is half that of the nanoparticle layer (4.5 nm). These analyses can be seen in the *Figure 48*a and *Figure 49*. Where the variability in the radii of the nanoparticles and the thickness of PNIPAM are identified as the main factors responsible for the broad nature of the absorption resonance (inhomogeneous broadening) and the lower spectral purity of the colors. This fabrication process and characterization provide valuable insights into the properties and behavior of the self-assembled structural color system.

   The Finite Difference Time Domain (FDTD). To start the modeling process in FDTD, we analyzed the morphology of the aluminum nanoparticles layer using SEM. We extracted a histogram of equivalent radii from the SEM's micrographs, where for a particle i, r_i^{eq} is defined as the radius required to fill the area A_i, so $r_i^{eq} = \sqrt{A_i/\pi}$. The next step was to perform a Gaussian fit of the histogram to extract the equivalent mean radius how to show the *Figure 49*. Then we take into consideration the filling factor f as the sum of the areas of the particles $(\sum A_i)$ over the total available area A_T then $f = (\sum A_i)/A_T$. With the

help of Dr. Pablo Cencillo, the same procedure as the simulation of self-assembled nanoparticles was carried out (described before in this thesis). We conducted FDTD simulations using Lumerical Inc., where we simulated a hemispherical particle with the mean equivalent radius obtained from SEM analysis, filling factor f, and PNIPAM thickness ranging from 25 to 45 nm, We set square periodic boundary conditions and illuminated with a plane wave at normal incidence. We placed a monitor at the top the simulation box to extract the reflection curves. Once obtained, it used MATLAB code to track the spectral positions of the minima of the reflection curves as a function of PNIPAM thickness, where we observed a positive slope of 7 nm red-shift for every additional 1nm of the polymer layer, demonstrating the high sensitivity of the gap-plasmon resonance to geometrical parameters the Refractive Index Values utilized in this work for the reflective indices of aluminum[96] and PNIPAM[97] are obtained from literature.

Reflection Curve Measurements and Imaging.

1. **Measurement Setup:**
   - Reflection curves are acquired at normal incidence.
   - Unpolarized light is used.
   - A 4x objective with a 0.07 numerical aperture is employed.
   - A fiber-coupled spectrometer (HR 2000+, Ocean Optics) is used to capture spectral data.

2. **Reference Mirror:**
   - An aluminum mirror serves as a reference to normalize the measurements. This reference ensures accurate and reading.

3. **Consistent Illumination:**
   - To maintain illumination consistency:

---

[96] E. D. Palik, Handbook of Optical Constants of Solids, vol. 3.

[97] Hélène Gehan, Claire Mangeney, Jean Aubard, Georges Lévi, Andreas Hohenau, Joachim R. Krenn, Emmanuelle Lacaze, and Nordin Félidj, "Design and Optical Properties of Active Polymer-Coated Plasmonic Nanostructures," *J. Phys. Chem. Lett.,* vol. 2, no. 8, pp. 926-931, 2011.

- Samples are photographed with flash-light at a fixed intensity.
- This fixed intensity ensures that the lighting conditions for imaging remain constant across measurements.

This setup and imaging procedure contribute to reliable and consistent data collection, which is essential for accurate analysis and interpretation.

Scheme and setup for measuring Relative Humidity and Temperature.

To measure Relative Humidity (RH) and Temperature (T), a chamber was built where the level of humidity and temperature is controlled, which consists of introducing water vapor to have humidity in the chamber and hydrogen to control the amount of humidity introduced into the chamber and hydrogen to control the amount of humidity introduced into the chamber through two valves, as shown in *Figure 45*.
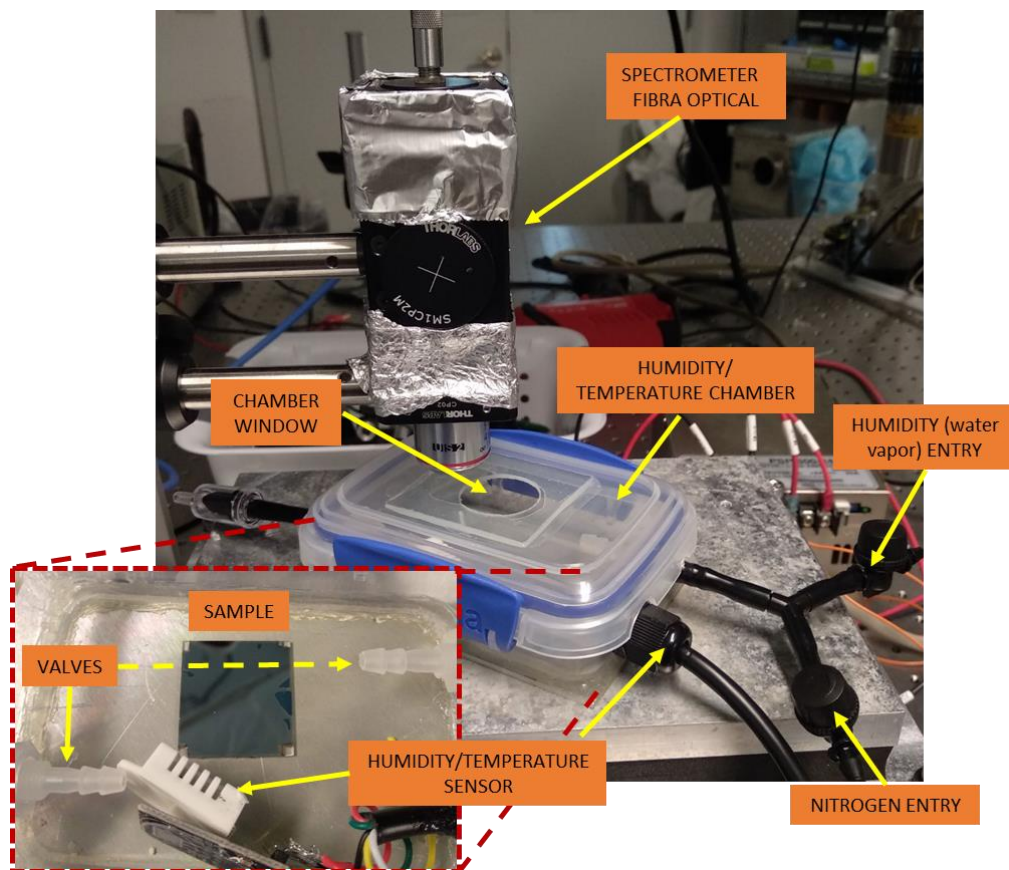
Figure 45 Relative Humidity and Temperature chamber setup. The Figure shows the sample is placed inside a closed chamber, and water vapor or nitrogen is introduced to control humidity around the sample. The chamber floor is metal and is always in contact with the thermoelectric to transfer or remove heat. The measure of reflection is possible thanks to the windows that has chamber.

The detection is made for a humidity and temperature sensor that is introduced inside the chamber. The temperature is controlled employing a Thermoelectric (Model TC-48-20 OEM Thermoelectric Cold-Plate Cooler), which comes into contact with the floor of the chamber. Through heat transfer, the chamber is heated or cooled inside. The thermoelectric can heat up to 199°C and cool to -20°C. The entire scheme can be seen in *Figure 46*. The sample is placed inside the chamber to control humidity and temperature; when the temperature and humidity change, the reflection is simultaneously measured using the spectrometer.
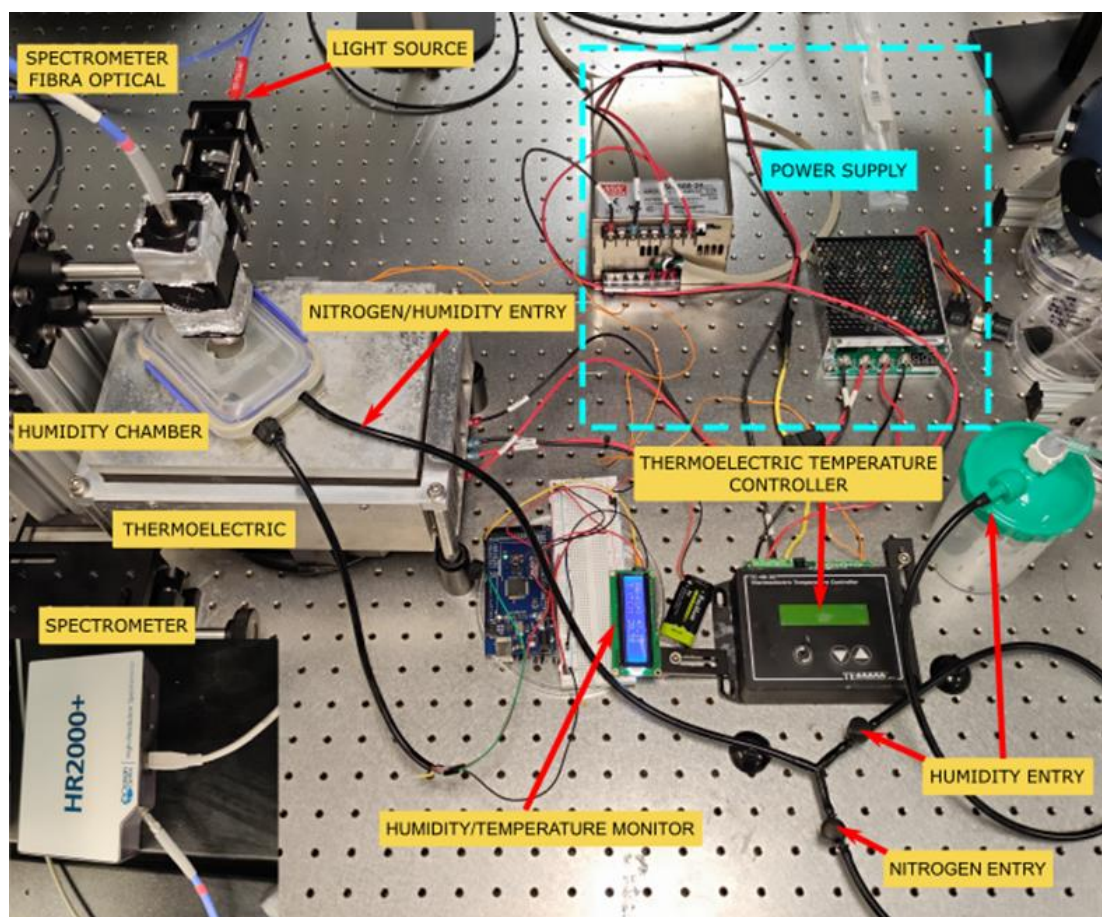
Figure 46. Scheme diagram for reflection, humidity, and temperature measure where it shows the spectrometer, the humidity/temperature chamber, and the thermoelectric.

Optical contact angle measuring and contour analysis system.

For the analysis of the physical properties of the surface of the sample PNIPAM/nanoparticles, we used the optical contact angle measuring and contour analysis systems (OCA 15EC, Dataphysics Instruments, see *Figure 47*) where the sample is analyzed when the temperature is below of the lower critical solution temperature (LCST) around 32°C for PNIPAM and to the temperature that exceeds 33°C. The sample was placed in the center of the sample table together with a ceramic thermoelectric to increase the temperature. Then, a drop of water of 10 µl on the sample is deposited using a single direct dosing system SD-DM. These liquids can be positioned and dosed with an electronic syringe ESr-N, as shown in *Figure 47*. The system can take a video of the sample when the drop is deposited. The camera can ensure pin-sharp drop images and facilitate effortless analysis with the software. The analysis obtained is showing more later.
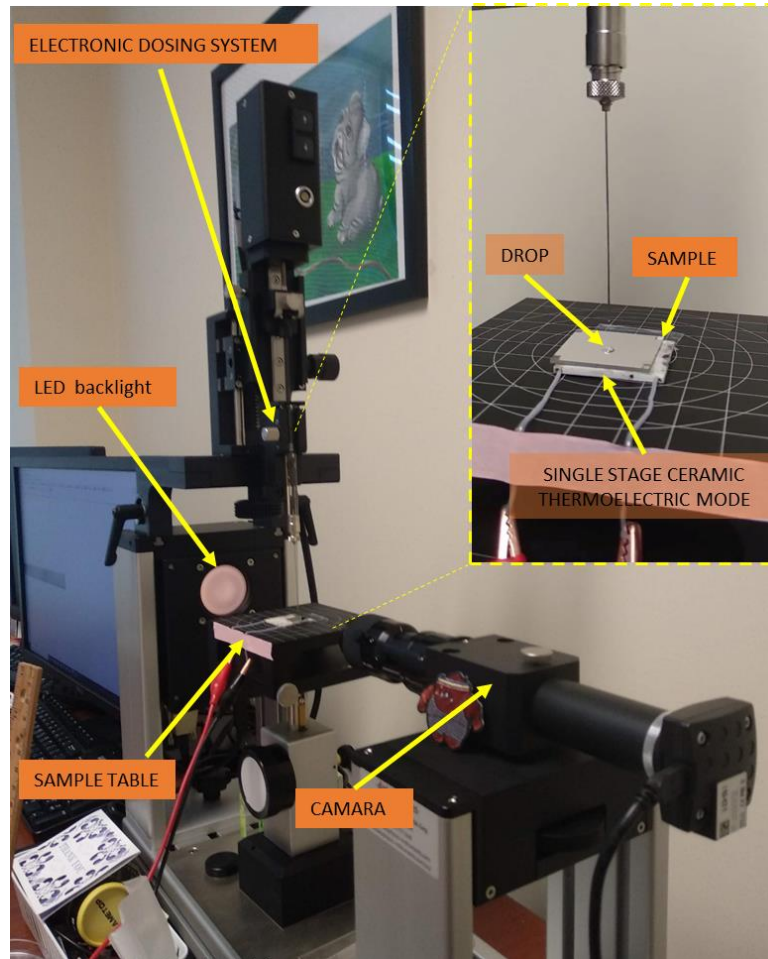
Figure 47 The optical contact angle measuring and contour analysis system OCA 15EC (Dataphycs Instruments).

4.2.3.   Results and Discussion

This section shows the experimental results of the hybrid PNIPAM/nanoparticles stack. The first part describes the PNIPAM ultrathinfilm, which analyzes the polymer's morphology and characteristics. The next part presents the aluminum nanoparticles deposited on the PNIPAM ultrathinfilm, where optical properties and geometrical change when the humidity and temperature are around; this change can be seen with the eyes and measured. Another result in this text is the stack simulation by mean software Lumerical and methode of the Finite Difference Time Domain (FDTD), where the compatibility of the simulation and the experimental result is observed. Finally, obtaining, as a final application, a humidity sensor.

Analyses of surface PNIPAM ultrathin film morphology and the self-assembly aluminum nanoparticles.

Like a first start at the stack analysis, the PNIPAM films and the nanoparticles are analyzed separately. For analysis of the layers of the stack, we used the AFM where it was possible to obtain the morphology of PNIPAM film and of nanoparticle self-assembly of 5 nm; this result shows the roughness of PNIPAM where we can see that the surface is more smooth than the nanoparticles layer, this is possible to see in the graphics 3D and in the comparison of their cross sections where the PNIPAM average surface roughness is found to be of 2 nm, half of that of the nanoparticles layer, that is 4,5 as shown in the *Figure 48*.
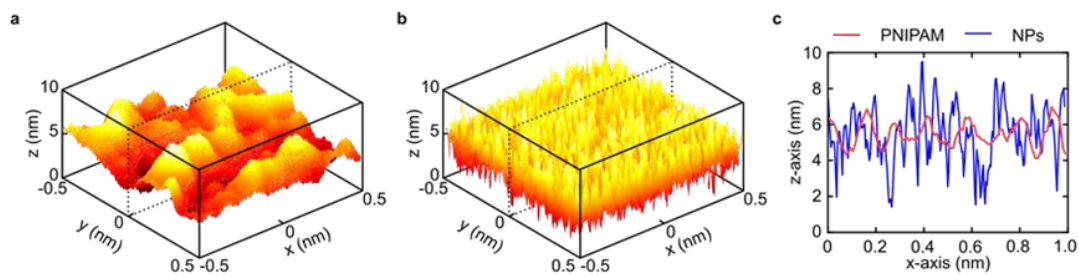
Figure 48a,b AFM morphology analysis for the PNIPAM film as spun coated and the nanoparticle self-assembly (5nm). c, The PNIPAM average surface roughness is 2 nm, half of that of the nanoparticles layer, which is 4.5 nm.

A sample with 5 nm of aluminum thickness deposit in shape nanoparticles was analyzed with the SEM, where it was possible to obtain the micrography of the aluminum nanoparticles we can see in *Figure 49*a. The Figure shows different sizes of nanoparticles; to know what size predominates in the sample, we extract the histogram of equivalent radii. This result is used in the simulation FDTD of the stack. *Figure 49*b, the graphic of bars shows all the radii possible that can be grown on the sample; this data is fitted to a Gaussian solid line corresponding where the mean value is 14.5 nm, for a thickness mass of 5 nm.
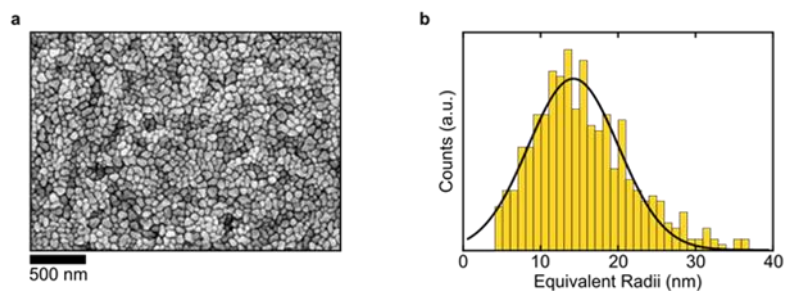
Figure 49 a, SEM micrograph of the aluminum nanoparticles layer. b, The SEM image analysis allows for the extraction of a histogram of equivalent radii for particles. The solid line corresponds to a Gaussian fit, with a mean value of 14.5 nm, for a thickness mass of 5 nm.

Hybrid PNIPAM/Plasmonic sensor.

Considering the characteristics of PNIPAM and nanoparticles analyzed, the self-assembled structural combining polymer and nanoparticles is now a hybrid PNIPAM/Plasmonic sensor. The sensor is composed of a layer of densely packed, self-assembled aluminum nanoparticles situated on top of an ultrathin PNIPAM polymer layer. This assembly is deposited over an aluminum backplane, as shown in *Figure 50*a. It is essential to point out that the sensor is constructed sequentially; that is to say, an optically thick layer of aluminum is evaporated onto a substrate, and PNIPAM is applied through of aluminum nanoparticles is deposited on top of the stack using an E-beam evaporator operated at a low rate. The details of the processes of deposit, evaporation, and growth are described in the section and chapter methods of this thesis.
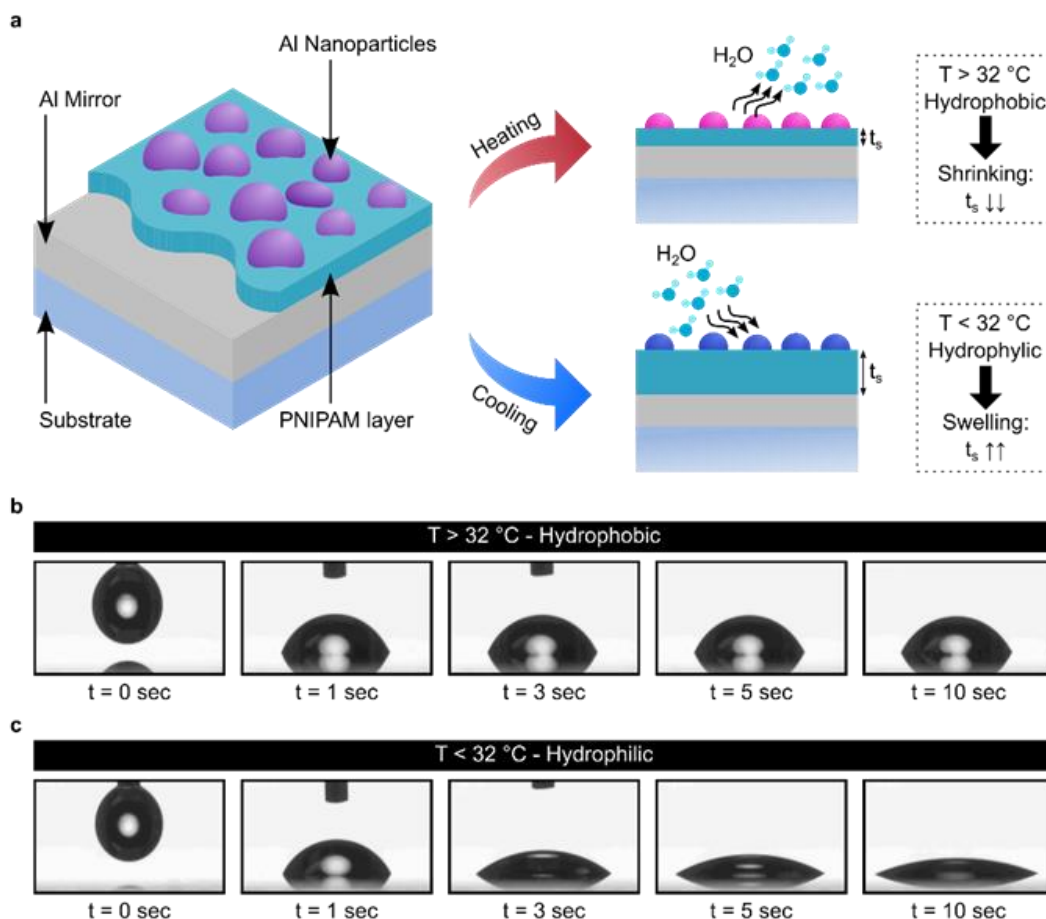
Figure 50 a The active color nanostructure comprises an aluminum self-assembled layer atop an ultrathin PNIPAM film positioned over a reflective back mirror. These metallic particles exhibit gap-plasmon resonances that can be adjusted by altering the thickness of the spacer. When the temperature falls below the LCST, the PNIPAM absorbs water, causing it to swell. Conversely, when the temperature surpasses the LCST, the PNIPAM expels the absorbed water, leading to a contraction in size. b, Above the LCST, PNIPAM exhibits hydrophobic properties, preventing water from bonding to the polymer layer. c, When the sensor's temperature is reduced below the LCST, the PNIPAM transitions to a hydrophilic phase, allowing it to absorb water again.

As discussed previously in this thesis, specifically in section 4.1 Self-assembled Plasmonic Paint and Chapter 2, by having ambient illumination, the free electrons within the metal nanoparticles can collectively oscillate, a phenomenon known as localized surface plasmon resonance. Light is strongly absorbed at wavelengths matching this resonance, while off-resonance components are back-reflected by the aluminum mirror, creating vibrant colors. Importantly, due to the close proximity of the plasmonic self-assembly to the back mirror, the electromagnetic mode is coupled to the ultrathin cavity. This coupling makes it highly sensitive to changes in the stack geometry while

maintaining relatively consistent behavior across different angles and polarizations, i.e., they are independent. This way, the structures achieve color by subtracting specific bands corresponding to the plasmon resonances from the incident white light. Therefore, any alteration in the structure, such as changes in nanoparticle sizes or spacer thickness, will result in a corresponding color change.

As mentioned earlier, PNIPAM is a thermoresponsive polymer with a sharp Lower Critical Solution Temperature (LCST) around 32°C. Above this temperature, the polymer transitions to a hydrophobic state, expelling water molecules bound to the polymer chains and reducing the layer's thickness. This reduction in the volume of the PNIPAM layer affects the overall cavity, causing the resolution wavelength for the gap-plasmon to shift towards shorter wavelengths. This results in an increase in the red components of the reflected light. Conversely, when the temperature of the stack is lowered below the LCST, the polymer transitions to a hydrophilic phase, absorbing water and causing an increase in layer thickness. This increase leads to a red-shift of the resonant wavelength, resulting in increased blue components in the reflected light (as illustrated in *Figure 50*a on the right).

The polymer's phase transition can be further characterized using contact angle measurements. A 10µL droplet of water is applied to the nanosensor at temperatures above and below the LCST, and its dynamic behavior is observed. As expected, at a temperature exceeding the LCST (50 °C), the droplet remains on the surface for an extended period without any discernible change in the contact angle, as illustrated in *Figure 50*b. This behavior corresponds to the hydrophobic phase of the PNIPAM polymer.

Thermal and Humidity Tunable Optical Response

It has been reposted that ultrathin films of PNIPAM exhibit change in response to alterations in the surrounding environment's temperature and humidity levels. Consequently, both stimuli are anticipated to induce alterations in the structure's color. To this motive, as previously described in the method section, a specially designed sealed gas chamber is employed to analyze both

108

factors' influence comprehensively. This chamber allows the controlled injection of nitrogen or water vapor to decrease or increase the relative humidity (RH). The chamber is situated on a thermoelectric that regulates the sensor's temperature. Additionally, the chamber is outfitted with an optically transparent window to facilitate real-time spectroscopic measurements. This setup enables the independent adjustment of temperature or relative humidity, allowing for the separate examination of their effects.

We initiate our investigation by examining the impact of temperature, holding the atmospheric water content constant. To achieve this, we seal a sensor composed of aluminum nanoparticles with a thickness equivalent to 5 nm mass and a 35.5 nm PNIPAM polymer layer at room temperature (20 °C) with a relative humidity of 50%. The environment is sealed, and subsequently, the sample is subjected to both heating and cooling, reaching temperatures of 10 °C and 40 °C, while observing the resulting color changes in the structure (refer to *Figure 51*a). where the photographic of the sample showing evident color shift. Upon cooling, the sensor absorbs moisture from the surrounding, causing it to swell. This leads to red-shift in the absorption of the plasmonic system, thereby diminishing certain red components in the reflected light. Conversely, when the sensor to contract. This reduction in cavity length intensifies the red components of the reflected wave. It´s important to note that a red-shifted absorption resonance in a subtractive coloration scheme leads to a greater contribution of shorter wavelengths in the reflected light.

Conversely, the reflection becomes red-shifted when the resonance undergoes a blue shift. In simpler terms. A red-shift in the absorption curve results in a blue-shift in the perceived color, and conversely, a blue-shift in absorption yields a red shifted hue. Spectral measurements of the sample at all three temperatures are presented in *Figure 51*c. Although there is minimal discernible change when transitioning from 20 to 10 °C, given that both temperatures fall below the LCST and consequently reside in the hydrophobic state, leading to the expulsion of water and subsequent contraction of the polymer layer. This remarkable shift results in a dramatic alteration of color.
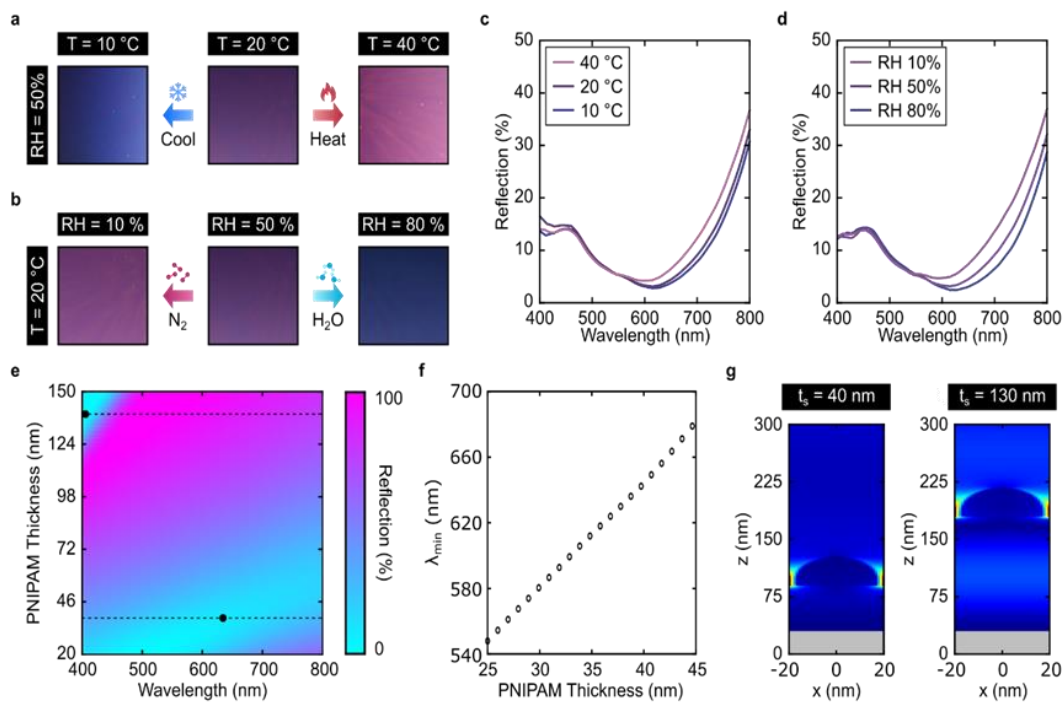
Figure 51 a) When the structure is heated above the LCST, the PNIPAM layer transitions to the hydrophobic phase, expelling water and causing a volume change, resulting in a color shift. Conversely, when cooled below the LCST, the PNIPAM layer transitions to the hydrophilic phase, absorbing water and changing volume and color. b) Changes in the PNIPAM volume can also be induced by altering the environment's water content. In dry atmospheres, water is released by the PNIPAM to maintain chemical equilibrium, while in saturated atmospheres, water is absorbed. c-d) Reflection curves for samples in a and b, respectively. e) FDTD simulation of the reflection curves for different PNIPAM thicknesses. The resonance shifts towards the red with increased thickness, resulting in bluer hues. f) The spectral position of the reflection minima plotted against thickness as obtained in, e.g.) Electric field enhancement of the nanoparticle for both thicknesses.

The influence of environmental humidity as a driving stimulus for polymer changer is evident when maintaining a constant temperature of 20 °C and dynamically introducing nitrogen/water into the atmosphere (as illustrated in *Figure 51*b). We observe that the alterations are more pronounced with variations in humidity compared to temperature, even though the polymer consistently remains below the LCST throughout this measurement, thus remaining in the hydrophilic phase with no phase change. By increasing the water content in the atmosphere to RH 80%, the polymer absorbs more water molecules due to the increased availability, resulting in a subsequent change in thickness and a

corresponding shift in color. Conversely, the polymer expels some of the previously absorbed water in a drier atmosphere, reducing volume. We attribute this behavior to a shift in the chemical potential equilibrium between the water within the polymer layer and the surrounding atmosphere. As the atmosphere dries, a new equilibrium is established between the polymer and the environment, causing water to transfer to the air to maintain equilibrium. Conversely, the chemical potential changes direction as the atmosphere becomes more saturated with water. This favors hydrogen bonding with the monomer chains[98], leading to the polymer absorbing additional water molecules. Reflection curves depicting changes in relative humidity while maintaining a constant temperature can be observed in *Figure 51*d.

In the next step, to gain further insight into the optical mechanism, we conducted Finite-Difference Time-Doman (FDTD) simulations on the stack with varying polymer thickness (see section 4.2.2. Experimental Methodology). We employed a single aluminum nanoparticles hemisphere with a radius equivalent to the mean radius of a 5 nm thickness mass-equivalent self-assembly. Keeping it fixed while adjusting the PNIPAM spacer thickness from 25 to 45 nm. The simulation was conducted for a plane wave propagating perpendicular to the stack, with periodic boundary conditions in orthogonal directions. Considering the experimental results, we can observe and interpret that the simulation results align well with these. As the polymer layer's thickness increases, the reflection minima shift towards longer wavelengths, with no significant qualitative change in the resonance shape (*Figure 51*e-g). For more precise tracking of the resonance position, we extracted the spectral position of the reflection minima for every 1 nm increment in polymer thickness (*Figure 51*f). The proportional relationship between the PNIPAM thickness and the position of the reflection minima (absorption maxima) unmistakably confirms the behavior we previously described. Both lower temperatures and higher humidity promote waver

---

[98] Y. a. S. K. Liu, "Thermoresponsive Behavior of Poly(N-isopropylacrylamide) Solid Ultrathin Film under Ordinary Atmospheric Conditions," *Chemistry Letters,* vol. 46, no. 4, pp. 495-498, 2017.

absorption by the polymer, leading to swelling. In comparison, higher temperature and drier environments reduce the water content in the polymer layer, resulting in thinner dimensions.

From the graph of *Figure 51*f, we estimate that the slope has a spectral shift of 7 nm for every 1 nm increase in PNIPAM thickness. Intriguingly, in contrast to applications involving grafted PNIPAM, where swelling thicknesses can be several times that of the dry polymer, the dynamics of ultrathin films do not exhibit such an extraordinary expansion. This ensures that the polymer thickness remains sufficiently thin to preserve the gap-plasmon hybridization and maintain vivid coloration. This would otherwise be lost interactions between the self-assembly and the cavity [99] [100].

Temperature-Response Coloration.

Expanding the color range generated by adjusting the structures in response to temperature and humidity alterations can be achieved by incorporating nanoparticle layers of varying sizes. Six distinct mass thicknesses of aluminum nanoparticles, ranging from 3 to 5.5 nm, are grown over a 35.5 nm PNIPAM layer. The samples are subjected to temperature changes in an open atmosphere, transitioning from 15 °C (below LCST) to 50 °C (above LCST), and photographs are taken at the same time, as we can see in *Figure 52*a. The larger particles exhibit a more pronounced color shift than the smaller ones. As discussed earlier, changes in the thickness of the polymer interference condition of the hybrid gap-plasmon system [101]. For smaller particles, the plasmonic

[99] Chanda, Daniel Franklin and Ziqian He and Pamela Mastranzo Ortega and Alireza Safaei and Pablo Cencillo-Abad and Shin-Tson Wu and Debashis, "Self-assembled plasmonics for angle-independent structural color displays with actively addressed black states," *Proceedings of the National Academy of Sciences,* vol. 117, no. 24, pp. 13350-13358, 2020.

[100] Chanda, Pablo Cencillo-Abad and Daniel Franklin and Pamela Mastranzo-Ortega and Javier Sanchez-Mondragon and Debashis, "Ultralight plasmonic structural color paint," *Science Advances,* vol. 9, no. 10, 2023.

[101] F. C. Mikhail A. Kats, "Optical absorbers based on strong interference in ultra-thin films," *Laser Photonics Rev.,* vol. 10, no. 5, p. 699, 2016.

resonance falls within the violet/near-UV bands, where minor tuning has a relativity modest impact on the overall visible color alteration [99] [100]. Conversely, for larger particles, the plasmon resonance is situated at the center of the visible spectrum, where the human eye is more sensitive, resulting in a more discernible distinction between colors.

We can notice that as particle size increases, the plasmon resonance shifts towards the far red/IR bands, leading to less conspicuous changes. By analyzing the spectra in both the heated and cooled states and extracting the CIELAB components, we can gain a better understanding of the relationship between color alteration and particle size (*Figure 52*b). As mentioned earlier, the most noticeable color change is observed within the central bands of the visible wavelengths, where human eyes are most responsive to variations. This corresponds to the orange, pink, and purple sensors (nanoparticle sizes ranging from 4 to 5 nm). In contrast, the yellow and blue samples (comprising the smallest and largest nanoparticles) exhibit a less pronounced color shift.
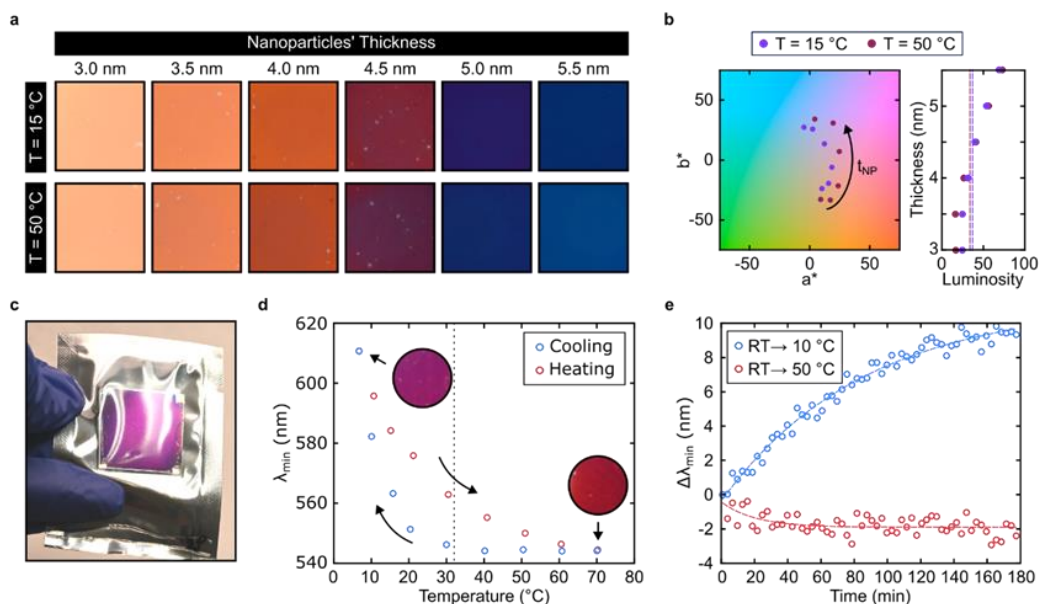
Figure 52 a) The size of the nanoparticle layer provides an additional parameter for customizing the structure's color during fabrication. Temperature variations lead to less noticeable color changes for smaller and larger nanoparticles. In contrast, the most significant changes occur for central values, where the plasmonic resonance is centered in the visible spectrum. b) CIELAB components of the samples from a. c) To eliminate the effect of atmospheric water content, the sensors are sealed in an envelope. d) The

heating and cooling dynamics show a clear asymmetry resulting from two different processes, above and below LCST. e) The asymmetry is particularly evident when tracking the spectral shift while heating and cooling a sample from room temperature (20 ºC) to 10 ºC and 50 ºC.

Isolating Temperature Effects from Humidity Effects.

To separate temperature –induced changes from those due to humidity alterations, we enclose the sensors in a sealed transparent bag at RH 50 %, thereby maintaining a fixed amount of available water. We monitor the spectral shift of the reflection curve minimum with temperature changes (*Figure 52*c). Starting at 70 °C, we gradually cool the sensor to 5 °C and subsequently reheat it to the initial 70 °C (*Figure 52*d). We implement small temperature and time increments (5-10 °C every 15 minutes) to ensure and reaching an equilibrium state and to prevent failure from thermal shock.

Upon completing the cycle from cold to hot, it is observed that there are two different regimes when passing from the hydrophobic to be hydrophilic phase. In the cooling cycle (blue circles), the shift follows an exponential trend as water molecules begin to be absorbed by the polymer matrix once the temperature falls below the LCST. A sharp transition can be observed above 30-32 °C (dashed line). However, in the heating cycle (red circles), two different mechanisms come into play in determining the spectral shift. Initially below the LCST, temperatures establish varying balances between water absorbed in the polymer and the environment. However, as the polymer shifts to the hydrophobic phase by elevating the temperature above the LCST, water is expelled, and temperature differences only govern the kinetics of this desorption process. The initial spectral position is recovered if given enough time, effectively resetting the sensor (overlapping blue-red circles). Hence, the observed color shift in response to heating and cooling cycles displays asymmetry, aligning with the asymmetric changes in thickness reported for ultrathin PNIPAM films in the literature[102].

---

[102] Y. L. a. K. Sakurai, "Thickness Changes in Temperature-Responsive Poly(N-isopropylacrylamide) Ultrathin Films under Ambient Conditions," *ACS Omega,* vol. 4, no. 7, pp. 12194-12203, 2019

It analyzed the time dynamics of a sample transitioning from room temperature (RT =20 °C) to 10 °C (blue circles) and from RT to 70 °C (red circles) (*Figure 52*e), corroborating the previous behavior result. The samples were placed on a previously cooled/heated stage, where we tracked the reflection minima for 180 minutes. Analyzing the results in the cooling stage, we can see that the spectral shift follows the exponential behavior; the PNIPAM absorbs the water of the capsule. Similarly, in the heating stage, the spectral shift saturates and remains constant once all the water in the PNIPAM is expelled. Given the larger temperature gradient in this experiment (20 °C to 50°C) compared to the one conducted in *Figure 52*d, we can account for the rapid nature of the shift saturation observed in this instance.

Environmental Humidity-Induced Colorimetric Sensing.

We take the sample to conditions with low humidity for a more detailed examination of the impact of humidity on the sample's color; we once again employ the custom-made gas chamber (detailed in the Methods section). In the case of a sensor at room temperature, nitrogen is introduced into the chamber into the chamber until the relative humidity drops to 10 %. As previously explained, the chemical equilibrium is disturbed when the atmosphere is desiccated, causing water trapped in the polymer to tend toward evaporation. This leads to the release of molecules, reducing the spacer´s volume and resulting in an augmentation of the red components in the reflected wave (*Figure 53*a). Conversely, if water vapor is introduced into the chamber, the chemical potential is altered, and water molecules bond with the polymer chains, causing the layer to swell. More blue components will be present in this scenario in the reflected light. In contrast, red ones will diminish, transitioning from a pink/magenta appearance to a purple hue and, ultimately, to blue hue.

By introducing water in a controlled manner, we observe the resulting color change for a 5 nm self-assembly and a 35.5 nm PNIPAM film. Across eight relative humidity levels ranging from 10 % to 80 %, we photograph the samples, documenting the subsequent color shifts (*Figure 53*b). it's crucial to note that the temperature remains constant and is below color change is a consequence of

alterations in the thickness of the polymer layer following the desorption of water molecules. As the PNIPAM remains in the hydrophilic phase, changes in the atmosphere can be utilized to adjust the thickness smoothly, avoiding the characteristic abrupt change observed in the case of temperature-driven phase transitions.

Moreover, we observe that color alterations resulting from shifts in the environment´s water content occurs rapidly within seconds due to the speed of its response; a video was taken, and some images were extracted from different time intervals until a complete color change was achieved. These images are shown in *Figure 54*. This rapid response is characteristic of the ultrathin nature of the polymer, where the absorption process is primarily governed by the polymer/air interface, rendering it a swift sensor. Notably, the process is reversible, and the original color is fully reinstated upon injecting nitrogen or water. Consequently, our hybrid PNIPAM/plasmonic structure functions as a reusable, real-time, and self-powered humidity sensor. Finally, in contrast to temperature-driven changes, no resetting is necessary to reset the sample to a specific state when humidity induces the color shift, as demonstrated in *Figure 53*a.
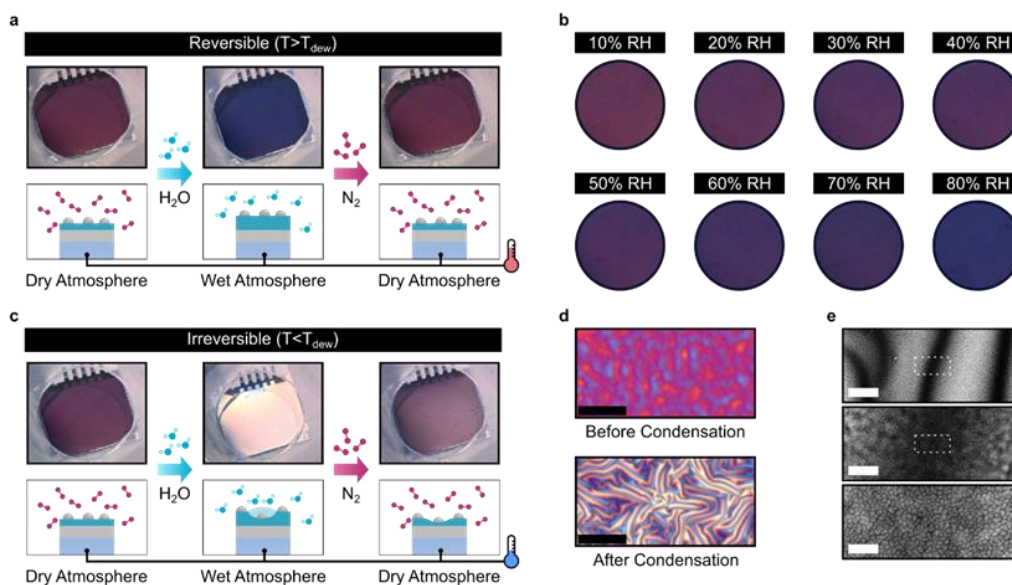
Figure 53 a) Below the LCST, the structures can be reversibly tuned by changing the humidity in the environment. As needed, this can be simulated in a gas chamber by injecting nitrogen (N2) or water

(H2O). b) Changing the humidity in the environment at room temperature (20 ºC) from a dry (10% RH) to a wet atmosphere (80% RH) allows for tuning of the color. c) If water condenses on the sensor, PNIPAM becomes oversaturated, resulting in an enormous enlargement of the spacer layer that disables the gap-plasmon modes. Even when dried, the color is not recovered. d) Microscope images of the sample before and after condensation (dry states below LCST). e) The peaks and valleys from drying the condensed irreversibly samples remove the color without affecting the nanoparticles. Scale bars for panel d are 100 μm. Scale bars for e, from top to bottom, correspond to 10 μm, 2 μm, and 100 nm.
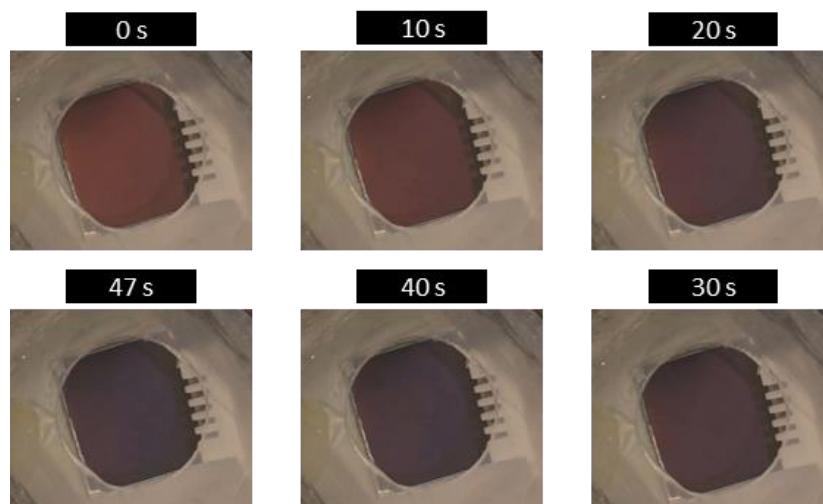
Figure 54 Images taken from different time intervals from 0 sec. to 47 sec. when the sample is completely changed to another color. Where the PNIPAM absorbs water but doesn't oversaturated, maintaining the relationship between the gap-plasmon modes.

Tamper-resistant condensation labels.

So far, the reposted results have been changes induced by both temperature and humidity entirely reversible, rendering the structures employed for sensing these stimuli reusable. However, as observed in the contact angle measurements for temperatures below the LCST (*Figure 50*c), a liquid phase on the sensor leads to color loss and irreversibility. This phenomenon presents an intriguing prospect for generating tamper-resistant condensation labels. Specifically, suppose the sensor is subjected to temperatures below both the LCST and the dew point. In that case, condensation will form, causing the color to vanish (*Figure 53*c). The dew point temperature is contingent on the environment's temperature and relative humidity. Thus, by maintaining a sensor at a low temperature in a dry atmosphere and gradually introducing room-temperature water vapor, the dew point condition can be attained, leading to

condensation. For a sensor at 5 °C and an environment at 20 °C, we observe dew formation at a relative humidity close to 40 %. Even if the atmosphere is subsequently dehumidified with nitrogen or the sensor is heated to a temperature above the LCST, the color does not recover. Importantly, this color loss is not attributable to particles begin washed away. Instead, when water condenses on the sensor, the PNIPAM absorbs water to saturation, resulting in extraordinary layer swelling and surpassing the spacer thickness required for near-field interaction that facilitates the gap-plasmon modes.

As a result of this excessive thickness, the plasmons are not excited, causing the sensor to exhibit a white appearance akin to that of the that of the back mirror (*Figure 55*c). when drying the polymer, it was observed that the polymer was deformed beyond restoration, losing the smoothness characteristic of the spin-coated samples. This desiccation process engendered peaks and valleys of various heights, generating a blended-color effect that can be attributed to the amalgamation of numerous distinct gap-plasmon modes, corresponding to each new layer thickness and resonating at different wavelengths. The hypothesis is validated by optical microscopy and scanning electron microscopy. Microscopic images depicting a sensor before and after condensation are available in *Figure 53*d. SEM micrographs of a desiccated sample (*Figure 53*e) following condensation reveal heightened roughness in the film. Although the nanoparticles persist across the entire polymer layer, the PNIPAM now exhibits a substantial thickness variability that nullifies the coloration. Importantly, even if the atmosphere is subsequently purged or the sensor is heated to a temperature above the LCST, the sensor will not regain its coloration, rendering it an inviolable dew label.
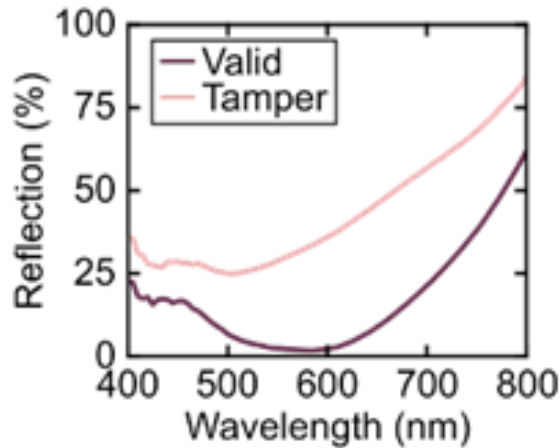
Figure 55 The loss of color saturation is appreciable under spectroscopic analysis, the reflection graph showing when the sample is completely saturated (light line) and when it is dry (dark red line).

4.2.4.   Conclusion

In this work, it was demonstrated that it is possible to incorporate plasmonic structural color as a resource for sensing through we have introduced a nanosensor integrating a highly sensitive ultrathin layer of PNIPAM responsive to both temperature and humidity, combined with a plasmonic nanoparticle assembly on top. This configuration gives rise to a gap-plasmon mode characterized by robust absorption resonances within the visible spectrum, notably influenced by the structure's geometry. Consequently, alterations in the polymer layer due to temperature or changes in humidity, either in the environment or within the sensor itself, lead to discernible shifts in color. This property can be harnessed for creating self-powered, reusable sensors for monitoring temperature and humidity. It is possible to create a wide range of colors that can be achieved by adjusting the parameters of the nanoparticle layer or the thickness of the spin-coated polymer. Still, the pink/purple sensors exhibit the most significant color variability, highlighting their potential in sensing applications. Notably, the effects induced by temperature or environmental humidity are reversible, provided no condensation occurs. After resetting, the sensors are prepared for reuse once again.

We proposed that our hybrid PNIPAM/plasmonic color structure can serve as a convenient, self-powered, and tamper-resistant dew label, considering that the condensation, in many scenarios, is undesirable. For example, metals lead to corrosion and premature wear, while organic materials create a conducive environment for mold and bacteria growth. Unwanted condensation also poses significant challenges in storage and shipping, necessitating controlled climate conditions. Specifically, in cardboard packaging, condensation can compromise the integrity of shipments, which is especially critical for valuable items like artwork [103].

Finally, Importantly, thanks to the fabrication techniques employed—spin coating and conventional evaporation—the hybrid PNIPAM/plasmonic sensors can be manufactured on a large scale, offering a practical pathway for real-world applications beyond laboratory settings.

---

[103] P. H. J. L. J. R. a. K. S. Patricia Ford, "IPI's Guide to Sustainable Preservation Practices for Managing Storage Environments, Image Permanence Institute," Rochester Institute Of Technology, 2012.

CHAPTER 5

PROJECT IN EXPERIMENTAL PHASE

Below, I will briefly explain this project, which is still in the experimental phase. The experiment consists of depositing a thin layer of VO_2 (vanadium oxide) on an aluminum substrate. Before depositing the VO_2, a thin layer of Titanium Dioxide (TiO_2) is deposited. This layer helps the injection and transport of electrons since its nature is a semiconductor. VO_2 is a material that can be used as a thermochromic material, given that its optical properties change significantly and reversibly with temperature. The deposit is made employing Sputtering, described in the methods chapter. When depositing VO_2 on the aluminum foil, it was observed that we had color. The new stack ($Al/TiO_2/VO_2$) was placed on a hotplate at approximately 100°C, the color changed, as seen in Figure 56b. and connecting the stack with a voltage of 8 volts was obtained again a color change (you can see this in the Grekos that are covered with foil in Figure 56c).

It should be noted that they are completely reversible changes. When analyzing the substrate with the SEM, it was observed that there were

nanostructures (See Figure 56a), concluding that these nanostructures are causing us to have structured color. The sample still needs to be analyzed; for this reason, only a brief explanation of its behavior and fabricating is given, but it falls within what we call structured color.
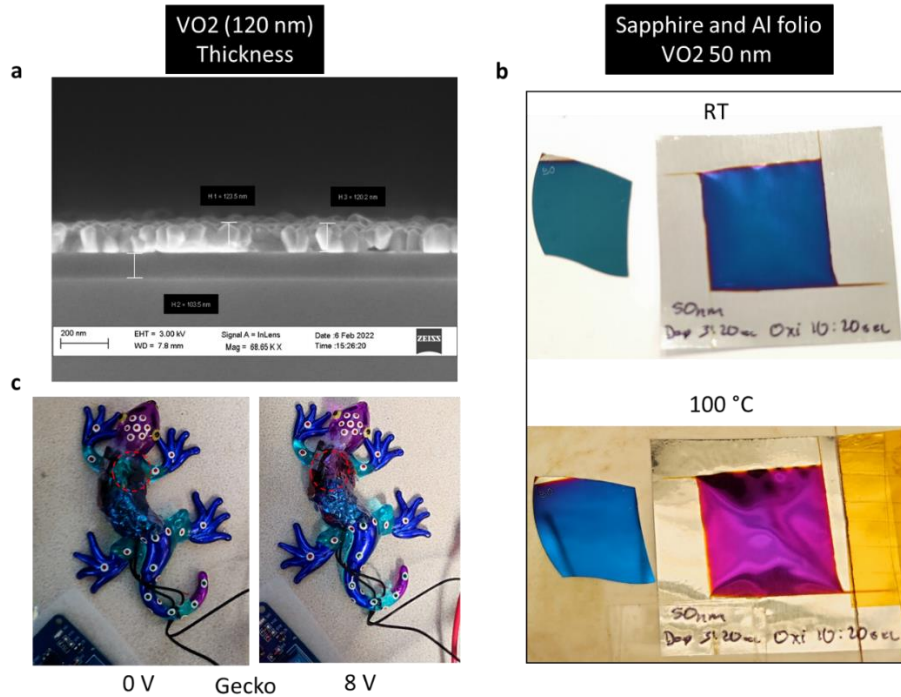
Figure 56 Figure a, SEM micrograph of the VO2 nanostructures layer where the Thickness is 120 nm. b, Aluminum was deposited on a sapphire substrate, V02 was deposited on this stack, and V02 was deposited on aluminum foil. The image shows the two samples where they are subjected to two temperatures. In the image above, the two samples are at room temperature; in the image below, they are at a temperature of 100 °C. The color change is appreciated due to the temperature difference. Finally, in Figure C, there is a gecko partially covered by an aluminum Foil, which has VO2; when a voltage of 8 v is placed, it changes color.

CHAPTER 6

GENERAL CONCLUSIONS

The work focuses on researching and manufacturing plasmonic nanostructures, which generate nanostructured colors. The plasmonic structure proposed in this work has potential for applications since the simplicity of its fabrication makes it feasible for its exploitation in industry. Concluding that by modifying some of its parameters, it is possible to obtain a wide range of plasmonic colors.

The material and process for manufacturing these plasmonic nanostructures are cheaper than those found in the literature since Aluminum is cheaper than other metals, and its resonance is found in the visible.

It was possible to fabricate a tunable plasmonic color is possible, which also functions as a temperature and humidity sensor. This was due to the sensitivity of the plasmonic structure and the polymer (PNIPAM) with a relatively Low Critical Solution Temperature.

Chapter 4 gives more specific and detailed conclusions for each of the two projects reported in this thesis, titled Self-assembled Plasmonic Paint (Dielectric thin-film and nanoparticles Al) and Tunability Color as a detection tool.

An extra project was described as still in the experimental phase but demonstrates that it has high research potential.

I conclude this chapter by reporting the publication works that were obtained from this thesis as well as presentations and conferences in which it was presented.

Participation in the LXIV National Congress of Physics held online from October 3 to 8, 2021, in a wall session, with the work titled "Angle independent structural color through ultrathin films."

Two publications in high-impact magazines were obtained from these projects:

Publication of the article "Ultralight plasmonic structural color paint" in the journal Science Advances, published in 2023, volume 9, and number 10.

Publication of the article "Reusable Structural Colored Nanostructure for Powerless Temperature and Humidity Sensing" in the journal Advanced Optical Materials, published in volume 11, number 16, 2023.

Finally, the cover of the journal Advanced Optical Materials is reported, which refers to the work published with the title "Reusable Structural Colored Nanostructure for Powerless Temperature and Humidity Sensing" in the journal Advanced Optical Materials" in volume 11, number 16 of 2023.

LIST OF FIGURES

135

List of acronyms

RGB   red, green, and blue

CMYK cyan, magenta, yellow, and Key

SPP   Surface plasmon polaritons

LSPR Localized Surface Plasmon Resonance

ML   Monolayer

FM   Frank-van der Merve

VW   Vollmer-weber

SK   Stranski-Krastanov

SEM   Scanning Electron Microscope

Ebeam Electron Beam Evaporation System

ALD   Atomic Layer Deposition

Al   Aluminum

Al_2O_3 Aluminum Oxide

FDTD   Finite Difference Time Domain

TMM   Transfer Matrix Method

NP   Nanoparticles

PNIPAM poly(N-isopropylacrylamide)

LCST Lower Critical Solution Temperature

RT   Room temperature

RH   Relative humidity

VO_2 Vanadium oxide

TiO_2 Titanium Dioxide

N2   Nitrogen

H2O   Water